The Deposition and Characteristion of Metallic Thin Films and Magnetic Multilayers Prepared by Pulsed Laser Ablation Deposition.

Anna Marie Widdowson

Submitted in fulfilment for the degree of Doctor of Philosophy

University of Warwick

March 1999

TABLE OF CONTENTS

ACKNOWLEDGEMENTS

I wish to thank Dr. Ric Allott, Dr. Edmond Turcu and co workers in the Laser Plasma X-ray Laboratory at the Rutherford Appleton Laboratory (RAL) for their assistance during my experimental time at RAL. The results obtained during this time form the wavelength, laser pulse temporal profile and tape target studies presented in chapter 5. I also wish to thank Exitech for their co-operation in the uniform profile investigation also presented in chapter 5. In particular I should mention Dr. Malcolm Gower and Dr. Phil Rumsby who agreed to let me use their equipment over a three week period and allowed Jason Haynes to take time from his usual work to assist me.

My thanks to Andrei Zenkevich and co workers in the Department of Solid State Physics at the Moscow Engineering Physics Institute for their co-operation in preparing samples which formed part of the comparison of deposition techniques in chapter 6. The sputtered samples, also discussed in chapter 6, were provided by Dr. Mark Watson and Dr. Pedro Gago-Sandoval formerly of the Centre for Data Storage Materials at the University of Coventry. I also wish to thank present members of this group, Prof. Roy Carey, Dr. Dave Newman and Jason Wiggins for allowing me to use equipment and for providing useful discussion regarding magnetic multilayer measurements.

Thanks also to Dr. Martin Lees for assisting with the vibrating sample magnetometer measurements and to Dr. Pam Thomas, Dr. Zhengwei Hu and Mick Cooper for assisting me with the x-ray reflectivity measurements.

Finally I wish to thanks members, past and present, of the Pulsed Laser Ablation Deposition group, Prof. Stuart Palmer, Dr. Tim Jackson, Dr. Roger Welch, Dr. Sushil Singh, Eduardo Palenque and Noor Baa'yah Ibrahim.

This work was possible as the result of a PhD Studentship funded by EPSRC.

DECLARATION

The work contained in this thesis is my own except where specifically stated otherwise, and was based in the Department of Physics, University of Warwick from October 1994 to March 1999. No part of this work has been previously submitted to this or any other academic institution for admission to a higher degree.

SUMMARY

This thesis investigates the use of pulsed laser deposition (PLAD) for the preparation of metallic films and magnetic multilayers. Initial work focuses on the effects of the laser wavelength and the laser pulse temporal profile on the deposition rates of nickel and silver and the droplet numbers deposited on to films. The results show that the deposition of silver films is affected by the sputtering of material from the substrate by energetic ions in the plasma and that this leads to saturation of the deposition rate at high fluences. The saturation features are not as pronounced in nickel deposition rates. We see that droplet numbers are only weakly dependent upon the laser wavelength, with fewer being present at shorter wavelengths. The effect that the number of pulses has on droplet numbers is also investigated. In the case of the pulse profile study more droplets were observed on films deposited using the picosecond (ps) pulse profiles. As for the nanosecond (ns) pulse profile the saturation in the deposition rates was observed in silver but not in nickel. The results of the ps laser pulse profiles showed that the ns background was dominant in the ablation process.

Two further investigations into reducing droplet numbers were performed. These showed that a uniform beam profile was not sufficient for eliminating droplets from the PLAD process and that the use of a tape target in conjunction with a ps pulse profile did not reduce droplet numbers either.

The aims of the second section of this thesis were to assess the suitability of PLAD for depositing multilayers and obtain Py/Pt multilayers showing a sensitive giant magnetoresistance (GMR) effect at low applied magnetic field. Samples prepared by two PLAD systems and by RF sputtering were compared. An anisotropic magnetoresistance effect was measured, however GMR was not. The multilayer structures were characterised using x-ray reflectivity and cross sectional transmission electron micrographs. The results showed greater uniformity in the layers deposited by sputtering than PLAD.

LIST OF FIGURES

LIST OF TABLES

Table 5.5 Growth conditions and droplet analysis for films grown at different wavelengths. * Values multiplied by 2 to take account of difference in thickness.

Table 5.6 Summary of droplet number/pulse for nickel and silver films shown in figures 5.9, 5.10, 5.11 and 5.12.

Table 5.7 shows the change in surface temperature of nickel and silver targets for isolated ns and ps features of the pulse profile as predicted by equation 2.3. The values take into account the ±10% error associated with the fluences of the ns and ps parts of the pulse profile.

Table 5.8 The nickel and silver deposition measurements shown in figure 5.17. λ=248nm.

Table 5.9 shows the measured and calculated threshold fluences for ps pulses and ns background. The ps pulse data is determined from figure 5.18.

Table 5.10 Evaporation rates for nickel and silver for the ps profile. The values are calculated using equation 2.12, after Kelly and Rothenberg (1985a).

Table 5.11 Characteristic surface damage wavelength, λ_D, for Ni and Ag and minimum droplet diameters, D and $2r_{min}$, (Bennett *et al.*, 1995; Kelly and Rothenberg, 1985a) for isolated 5ps pulses.

Chapter 6

Table 6.1 Shows the intended structures of Py/Pt multilayer specimens compared in this chapter. The preparation of all the samples is summarised in section 4.5. The subscripts 'war' and 'mos' denote the different PLAD systems described in sections 4.5.1 and 4.5.2 respectively. * The thicknesses of these layers are unknown.

Table 6.2 A summary of the total and bilayer repeat thicknesses obtained for a series of samples using x-ray reflectivity and TEM micrographs.

Table 6.3 Shows the saturation magnetisation values for PyPt2, PyPt3 and PyPt4 determined from figure 6.21 and the value determined from the moment/atom of $Ni_{0.8}Fe_{0.2}$ given by Crangle and Hallam (1963).

Appendix A

Table A.1 The nickel and silver deposition measurements at λ=193nm shown in figures 5.1 and 5.4.

Table A.2 The nickel deposition measurements at λ=248nm shown in figure 5.4.

Table A.3 The nickel and silver deposition measurements at λ=351nm shown in figure 5.1 and 5.4.

Table A.4 The nickel deposition measurements of *series 1, 2, and 3* shown in figure 5.3. λ=248nm.

Chapter 1

1 Introduction

1.1 Pulsed Laser Ablation Deposition

Pulsed laser ablation deposition (PLAD) is a potentially simple technique for depositing thin films. It involves the removal of material from a target using a focused laser beam to produce high energy fluences at the target surface. Ablated material from the target forms a plasma (or plume) perpendicular to the target surface. Material from this plume is deposited on to a substrate, usually placed parallel to the target, forming a film. Details of the ablation chamber and deposition conditions are given in section 4.1.

PLAD is a highly flexible technique and is easily adapted to new materials, including compounds, by changing the target. It has become a popular technique for preparing high-T_c superconductors such as $YBa_2Cu_3O_{7-\delta}$, (YBCO), and a range of other oxides. In comparison, molecular beam epitaxy (MBE) requires a new gun for each element and thus is not able to deposit compounds easily, making it less flexible than PLAD. Sputtering on the other hand can be used to deposit compounds and thus competes with PLAD in this area.

Although PLAD has become a widely used technique for the deposition of YBCO its progression to the deposition of metallic films has been much slower. This is because sputtering is already commercially available as a successful method for depositing metallic films. One advantage of PLAD over that of sputtering is that material consumption can be kept to a minimum. Targets with an area of $1cm^2$ are required for PLAD compared to target areas in the order of $5cm^2$ for sputtering. In the case of noble metal deposition, as in the work presented in chapter 6, the target size is an important financial consideration and thus PLAD could be a favoured deposition technique in such cases.

One of the disadvantages, however, of PLAD is the production of molten droplets in metal deposition, which deposit on to the film surface making it difficult to

obtain high quality films. For multilayer deposition where individual layers are of the order of 3nm thick, droplets 0.1-10μm in size are detrimental to the desired sample properties. This thesis addresses the problem of droplet production in the PLAD process. It investigates whether optimising laser parameters can prevent the production of droplets. The advantage of this approach for reducing droplets, rather than filtering for example, is that further understanding of the laser-target interaction can be obtained. This may lead to the eradication of droplets from the process. Other methods, however, do not tackle the source of the problem and can result in some of the advantages of the PLAD technique, for example a high deposition rate, being compromised, as discussed in section 1.6.

One of the main problems encountered in the work presented here is the lack of control of the PLAD process. This is borne out in the comparison of multilayer samples deposited by sputtering and by two different PLAD systems in chapter 6.

1.2 Outline of thesis

This thesis discusses the application and problems of PLAD for the deposition of metallic films and metallic multilayers. The remainder of this chapter discusses the literature relevant to the work presented in chapters 5 and 6. A brief overview of the development of PLAD is followed by a discussion of previous work relating to the effects of laser parameters on droplet numbers. An extensive amount of work has not been published in this area; thus the results presented in chapter 5 provide additional, valuable information relating to the production of droplets during the deposition of metallic films by PLAD.

The second half of this chapter reviews a range of multilayer samples deposited by PLAD. It also discusses a comparison of single metallic films deposited by PLAD, sputtering and thermal evaporation and sputter deposited multilayers containing noble metal spacer layers. This discussion along with the samples characterised in chapter 6 allow a comparison of multilayer deposition by sputtering and PLAD. The literature shows that there is still plenty of scope for the

development of PLAD for the deposition of metal films and multilayer devices if a competitive alternative to sputtering is to be achieved.

Chapters 2 and 3 discuss the theory relevant to chapters 5 and 6 respectively. Chapter 2 presents the theory of PLAD and droplet production. The theory of magnetoresistance is presented in chapter 3.

Chapter 4 describes the experimental procedures carried out in this thesis for the deposition of films and the characterisation techniques employed.

Chapter 5 investigates the effects of laser parameters on the deposition of metallic films, including nickel, silver, gold and copper. Initial work focuses on the effect that the laser wavelength has on the deposition rate of nickel and silver and the number of droplets produced. A similar investigation of the effect of the laser temporal profile is also presented. By changing the laser wavelength and laser temporal profile the absorption of energy into the target was altered, as described in section 2.2. The motivation for this was to minimise melting and thus prevent molten droplets from forming. However the results in chapter 5 show that droplets were still formed during the PLAD process under the different conditions. We also see that the deposition rates are affected by the sputtering of material from the substrate by energetic species in the plasma.

The final section of chapter 6 investigates the effect on the production of droplets of using a uniform beam profile and the use of a Cu tape as a target. Again the complete eradication of droplets by these methods was not achieved.

A comparison of multilayer samples deposited by two different PLAD systems and by sputtering is presented in chapter 6. The three deposition techniques are described in sections 4.5.1, 4.5.2 and 4.5.3 respectively. The multilayers were deposited to investigate a sensitive giant magnetoresistance response at room temperature, with low applied magnetic field, however the results show only an anisotropic magnetoresistance effect. In addition the magnetisation curves for some of the samples are shown to confirm that they are ferromagnetic. The structure of the samples is analysed using high resolution x-ray reflectivity curves and cross sectional

transmission electron micrographs. The results show that the sputtered samples have the highest quality multilayer structure.

To summarise this thesis addresses one of the major problems faced by PLAD, i.e., the production of droplets. The results show that droplets cannot be eliminated from the deposition process by altering the laser parameters alone. However they do suggest that the number of droplets can be reduced, and as a consequence greater control over the PLAD process can be achieved. In addition we see that the deposition rates of nickel and silver are dependent upon the energy of depositing species which can give rise to sputtering of the depositing films. This also has implications for the control of film growth via PLAD. The comparison of the multilayer samples in chapter 6 shows that least uniformity is observed in samples deposited via PLAD. This further illustrates the importance of obtaining a controlled deposition process. Such control is required if PLAD is to become a viable alternative to sputtering.

1.3 The Development of Pulsed Laser Ablation Deposition

Following the development of the ruby laser (Ready, 1963; White, 1963; Askar'yan *et al.*, 1963) an interest developed in the laser-target interaction of both solids and liquids. This was quickly extended to the deposition of ablated material from the target thus forming a range of films by pulsed laser ablation. Early films included semiconductors and dielectrics (Smith and Turner, 1965). As higher power lasers were developed their application in material deposition was continually investigated. Renewed interest in PLAD was generated in 1987 when high T_c superconducting films were successfully deposited by this technique (Dijkkamp *et al.*, 1987). Thus much of the early work focused on the deposition of oxides and the technique enjoyed continued success in the deposition of the high T_c superconductor YBCO.

The important features in PLAD history which led to its substantial usage for the deposition of high T_c superconductors by this method are given in a review by Cheung (1994). The review covers the period 1965-1994 and also discusses the use

of PLAD for the deposition of ferroelectric thin films and other perovskite oxides. Other comprehensive reviews of PLAD include Cheung and Sankur (1988), which gives a summary of materials deposited, and Jackson and Palmer (1994). An account of the deposition of a whole range of materials is given by Boyakovet *et al.* (1978).

More recently PLAD has been successful in depositing rare earth manganites, which show colossal magnetoresistance properties, see for example Zhang *et al.* (1997), Koo *et al.* (1997) and Singh *et al.* (1996). Work also continues on YBCO, for an overview see Muenchausen and Wu (1994) and Li (1994). The use of PLAD to deposit $Si_{1-x}Ge_x$ with the eventual aim of fabricating heterostructures has also been investigated (Antoni *et al.*, 1995) although films are often found to be non-epitaxial, germanium rich in comparison to the target, and contaminated by droplets as a result of the ablation process. Greater success is enjoyed by the deposition of diamond like carbon films, which are usually deposited by sputtering. Such films are useful as protective layers, infrared windows and electrodes on electronic components. See for example Sato *et al.* (1987), Martin *et al.* (1990) and Levoska and Leppavuori (1995).

This thesis is concerned with the deposition of metallic films. Intuitively one might think that the deposition of single element and alloy films would be far simpler than that of complicated oxides yet the success of metals deposition has not equalled that of the well established perovskite deposition. The move to PLAD for the deposition of metals has been less popular for three main reasons. Firstly sputtering and evaporation are already very successful techniques for the deposition of metals. Secondly to produce high quality films stringent deposition conditions are required. To prevent contamination of metal films high vacuum is needed. This can reduce the simplicity of deposition and increase the cost of a PLAD system. Finally the deposition of metals is accompanied by the production of molten droplets which deposit onto the films, reducing the film quality. A compromise between the deposition rate and the droplet production often has to be established. Whilst an increase in the deposition rate, by increasing the laser fluence at the target, reduces

contamination problems it is counterproductive in that higher fluences usually lead to increased droplet numbers.

1.4 General Features of PLAD

Kools (1994) discusses many of the general features associated with the deposition of metals by PLAD. We see that the deposition rates of ~0.003nm/pulse or ~1nm/s (Kools, 1994 and Hubler, 1994 respectively) are comparable with the deposition rates of ~0.1nm/s determined in this thesis. These compare with sputtering, MBE and (chemical vapour deposition) CVD which have deposition rates of 1nm/s, 0.3nm/s and 2nm/s respectively (Hubler, 1994). This paper compares other aspects of PLAD with those of different deposition techniques. One aspect is the comparison of the energy of the species depositing onto the substrate. A region of 10-100eV is cited as being most desirable for good film production and PLAD fits this specification. However even at these energies some problems can arise with species in the plume being energetic enough to sputter deposited material from the substrate, especially if the target substrate distance is small, see section 5.2 for a more detailed discussion. It has been shown that this phenomenon can lead to non-stoichiometric deposition of films, as compared to the target, if preferential etching of one of the elements occurs. For example Van de Reit (1993a) *et al.* report a reduction in gallium content in FeSiGaRu films as the fluence is increased. Sputtering of copper films is also observed by Jordan *et al.* (1995). Stone *et al.* (1997) find that Tb-Fe films deposited by PLAD are terbium deficient. In this thesis we see the effects of sputtering on the deposition of material onto the substrate. At higher fluences the deposition rates tend to saturate.

So far only the measurement of deposition rate has been discussed, i.e., the rate at which material is deposited onto the substrate. The measurement of ablation rate is also well documented in the literature. This, in contrast, is the rate at which material is removed front the target. By the nature of these two processes it follows that the ablation rate can be affected by processes at the target, usually as a result of the shielding of the laser pulse from the target. This is shown for example by Stauter

et al. (1996) and Kononenko *et al* (1997). Both show that ablation rates are reduced as a result of shielding of the laser energy from the target. Kononenko *et al.* (1997) shows saturation in the ablation rate at a range of wavelengths, 1078, 539 and 270nm. The effect is more prominent in steel and aluminium than in ceramics and is also enhanced when moving to picosecond pulse lengths from nanosecond pulse lengths and is attributed to the absorption of the laser energy by the plasma. Stauter *et al.* (1996) suggest that the saturation of ablation rates in ceramics ablated using a laser wavelength of 1060nm, occurs as a result of the target being shielded as the plasma density increases, however shielding is not observed at 248nm. This suggests that at 248nm the plasma density is not high enough for absorption to occur. This is in agreement with the discussion in section 2.3.1.

In contrast to the ablation rate, the deposition rate can be affected by either a change in the ablation rate or processes of deposition at the substrate, i.e., by sputtering as discussed earlier in this section, or both. Thus when saturation of deposition rates is reported it is not always simple to ascertain which of these mechanisms is responsible.

1.5 Mechanisms for Droplet Emission/Production

One of the problems associated with PLAD is the production of droplets. The particulates seen on the metallic films are generally molten in origin as opposed to fragments broken from the target surface as seen for oxide targets. Thus a distinction is made between 'droplets' seen on metallic films and 'particulates' seen on oxide films (and other films deposited using higher melting temperature targets).
A comprehensive review of droplet mechanisms is given by Kelly and Miotello (1994), who illustrate the differences in particulate production arising from oxide materials and metals. For example in high melting point materials such as oxides, and also tungsten, repeated thermal shocks to the target from the laser pulses results in thermal stresses. Such thermal stresses cause cracking of features on the target, which are subsequently dislodged as particulates. Fracture features are evident in SEM micrographs of appropriate targets thus supporting the exfoliation mechanism

(Kelly *et al.*, 1985b; Muller *et al*, 1993; van de Riet *et al.*, 1993b). For metals, however, the melting point is generally lower. This means that melting occurs at the target surface. The molten pool is disturbed as a result of the pressure exerted by the developing plasma. This leads to molten droplets leaving the target surface and depositing onto the films. This is the hydrodynamic mechanism presented by Kelly *et al.* (1985b) and is discussed in more detail in section 2.4.1.1.

The formation of molten droplets is evident on a range of molten targets (Kelly *et al.*, 1985b; Thomas *et al.* 1992; Bennett *et al.* 1995, Brailovsky *et al.*, 1995). This is also illustrated in this thesis for ns pulse ablation in section 5.6.3 where wave formations evident on the targets support the hydrodynamic mechanism of droplet expulsion from molten material at the target surface, discussed in section 2.4.1.1.

Recent work on the factors affecting droplet emission includes that of Weaver and Lewis (1996). This work correlates the droplet distribution on aluminium with a Boltzmann probability distribution, i.e., the probability of a droplet of a certain size being emitted is related by Boltzmann statistics to the increase in the energy of the system resulting from the formation of the droplet. The theory supports the idea of volume vaporisation which gives rise to vapour bubbles disrupting the melt at the target surface thus emitting droplets. In Weaver (1998) the evolution of these vapour bubbles is homogeneous nucleation which enables droplet emission to be correlated with atomic number via the determination of the rate of formation of homogeneous bubbles per unit volume within the molten region of the target. Therefore in order to investigate this model different energy densities are required on the targets to ensure the same molten volume from target to target. Much of the work in the literature makes a comparison between materials at the same incident fluence. The constraint of having equal molten volumes on the target makes it difficult to ascertain the validity of this model with droplet numbers reported here and elsewhere. It is difficult to deconvolve the importance of the laser fluence and molten volume between different target materials. Certainly it is known that a decrease in fluence leads to fewer

droplets being present on the deposited films, however this is accompanied by a decrease in molten volume at the target and thus a decrease in homogeneous bubble nucleation. The crux of this matter is whether or not homogeneous bubble nucleation can be considered as the soul source of droplet emission from the target as opposed to say the hydrodynamic model of Kelly and Rothenberg (1985a), the development of capillary waves arising from the pressure exerted by the plume at the molten surface (Brailovsky *et al.*, 1995) or the effects of inertial forces acting on the melt as a result of phase changes and thermal expansion at the target (Bennett *et al.*, 1995).

1.6 The Reduction of Droplets

The previous section shows that the main source of droplets on metal films arises from molten material at the target being expelled by the recoil pressure associated with the developing plume. This suggests that the reduction of such melting might result in the elimination of droplets from metal films deposited by PLAD. This is one of the areas under investigation in this thesis. In addition to this approach there are a range of other methods for reducing droplet numbers which are well documented by Cheung (1994), Chen (1994), Jackson and Palmer (1994) and Cheung and Sankur (1988). Methods subsequent to these papers are discussed below.

Jordan *et al.* (1997) discuss the use of a curved magnetic filter previously employed to reduce droplets in vacuum arc deposition. This involves constraining the plasma to follow a curved solenoidal path dictated by a magnetic field. The droplets are not affected by the field and thus only material from the plasma is deposited at the end of the filter. A reduction in droplet numbers is observed on copper films deposited by PLAD using this filter.

Gorbunov *et al.* (1996) re-examine the reduction of droplets using a crossed beam method first suggested by Gaponov *et al.* (1982). The system was developed to allow the deposition of a wider range of materials than initially developed for high T_c superconductors. The crossing of the beams also acts as an energy band-pass filter where medium energy particles form the dense part of the plasma whilst the fastest

and slowest, i.e., most and least energetic, particles pass through unaffected. Gorbunov *et al.* discuss the use of this method for deposition of artificially mixed thin films and multilayer structures.

One of the disadvantages of filter methods is the reduced deposition rate at the substrate. The problems associated with this are two fold. Firstly by reducing the deposition rate the need for high vacuum conditions to avoid contamination problems is increased. Secondly the reduction in deposition rate below that used by sputtering reduces the appeal of the PLAD technique. Other methods have been suggested for aiding the reduction in droplets that do not involve reducing deposition rates. For example the correlation between target roughness and particulate numbers is well established, see for example van de Reit *et al.* (1993b). Thus translating the target reduces the amount of roughness that develops on the target and consequently minimises droplet numbers. Another suggestion for reducing droplet numbers is the use of uniform beam profiles. This thesis investigates the use of a uniform beam profile in section 5.9 where the limited literature on this subject and the results are presented and discussed.

This section has discussed recent topics associated with droplet formation and the pursuit of reducing droplet numbers. Some of these methods result in the decrease of deposition rates and make PLAD technologically more difficult. These detract from the fast and simple characteristics attributed to PLAD. Thus the next section discusses other parameters that might be exploited to reduce droplet numbers and thus improve the quality of deposited films.

1.6.1 The effect of laser wavelength on PLAD

In this thesis the effect of laser wavelength on the ablation process is discussed with the possibility of this parameter bringing about a reduction in droplets produced by the ablation of metals. Very little is published relating to the effect of wavelength on droplet formation. Misra and Palmer (1991), Kautek *et al.* (1990) and Koren *et al.* (1989) discuss the influences of wavelength on droplet production in YBCO, all of which report a reduction in particulates on films deposited at shorter wavelengths.

One of the few papers discussing the relationship of the production of particles with wavelength in metals is Dupendant *et al.* (1989). The authors claim that there is no clear wavelength dependence of particulate production. However the results could indicate a weak dependence of droplet numbers on laser wavelength in metals. The results for aluminium, for example, seem to indicate fewer droplets at shorter wavelengths. A comparison of the velocity distribution of droplets with a fluence of $15J/cm^2$ show higher droplet numbers at a wavelength of 1064nm than 532nm. The same is seen at a lower fluence of $4J/cm^2$ with the droplet numbers being greater at a laser wavelength of 1064nm than 335nm. A similar trend is seen in yttrium, although even at low fluences, i.e., $1.5J/cm^2$, a substantial number of droplets still remain. Hence it may be argued that there is a weak dependence of the droplet numbers with laser wavelength which could correspond with the findings in section 5.6.1.

Many of the other references pertaining to wavelength are associated with more general features such as ablation and deposition rates. Fabbro *et al.* (1982) is one of the earliest works relating ablation to wavelength. It shows an increase in the ablation rate with shorter wavelength resulting from increased absorption by the target. The results suggest that the mass ablation rate depends on the laser power density and the laser wavelength.

Svendsen *et al.* (1996) discuss the deposition rates of silver with fluence at wavelengths of 355nm and 532nm. At 532nm a linear increase in deposition rate with increasing fluence is observed, however above $10J/cm^2$ there is a greater spread in the data and the initial trend becomes less clear. For 355nm the initial deposition rate is equivalent to that of 532nm, however at slightly higher fluences the deposition rate begins to saturate and therefore appears lower than for 532nm. For example at $15J/cm^2$ the deposition rates are measured as 3.0×10^{13} Ag/cm^2 and 4.5×10^{13} Ag/cm^2 for 355nm and 523nm respectively. This corresponds with the results in this thesis where deposition rates are initially higher at shorter laser wavelengths but saturate more quickly. Similar features are seen in the ablation rate data presented by Stauter *et al.* (1996). This shows an initially high ablation rate of Si_3N_4 at a laser wavelength

of 532nm which falls off compared to the ablation rate at 1060nm. However it should be noted that even though the behaviour in the deposition and ablation rates appears similar the origin of the saturation characteristics of the deposition rates in Svendsen *et al.* (1996) and the ablation rates in Stauter *et al.* (1996) are not necessarily the same as discussed earlier in section 1.4.

The work of Kononenko *et al.*(1997), which shows ablation at 1078nm and 270nm, gives no clear indication of a relationship between the ablation rates and laser wavelength for aluminium nitride, aluminium and steel. This highlights the discrepancies still arising in the literature concerning the effect of laser wavelength on the ablation process.

1.6.2 The effect of laser pulse length on PLAD

Much of the work relating to the laser-target interaction using a variety of pulse lengths has occurred in the area of micro-machining where it is of particular importance to achieve precision machining with little thermal damage to the sample. Much of this work draws conclusions relevant to PLAD. In this area it is found that there is less damage caused to the target at shorter pulse lengths, usually sub-picosecond. This occurs because there is insufficient time within the duration of the pulse for heat to diffuse into the target. For example a reduction of a factor of 100 in the heat affected zone of a gold target is observed when moving from ns pulses to fs pulses (Rosenfeld and Campbell, 1996), which suggest that melting does not occur within the length of the pulse. These aspects are discussed in detail in section 2.4.2. Momma *et al.* (1997) discuss the variation in the laser-target interaction arising from the variation in pulse length. This work vividly highlights the reduction in melting of a metallic target as a result of moving to shorter pulse lengths. The micrographs are reproduced in figure 1.1. It shows two steel targets, the first ablated using a pulse length of 3.3ns and laser fluence of 4.2J/cm^2 and the second using a pulse length of 200fs with a laser fluence of 0.5J/cm^2, both at a laser wavelength of 780nm. The fluences used are the minimum fluences required for material damage at the target, i.e., threshold fluences. The figure clearly shows that melting occurs on the steel

sample ablated using the ns pulses and not on the target ablated using the fs pulses. One might expect that the low fluence at the target in the fs regime can be attributed to the reduction in melting, however others show that melting can still occur in metals at low fluences for ns pulses, for example see Dupendant *et al.* (1989). Hence this paper illustrates another feature of ultra short pulses which is generally observed. That is, the fluence required for ablation using shorter pulses is an order of magnitude lower than for ns pulses, also see for example Sandy-Lee *et al.* (1992). This implies that the ablation efficiency of picosecond and shorter pulses is higher than for ns pulses.

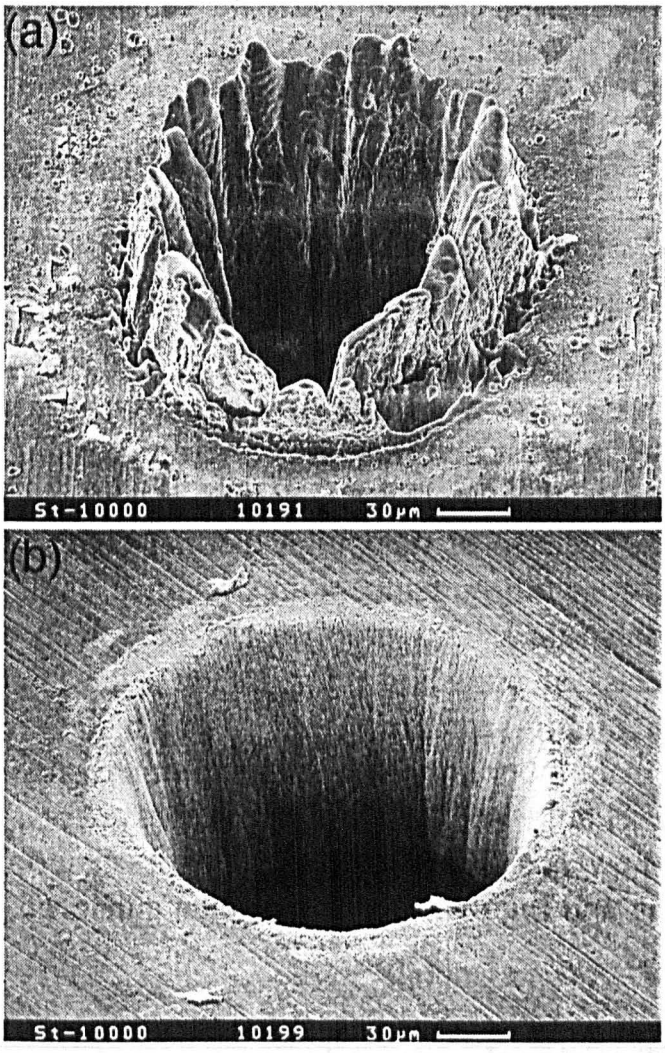

Figure 1.1 SEM micrographs of holes drilled through a 100µm steel foil. (a) τ_p=3.3ns, F=4.2J/cm^2, λ=780nm. (b) τ_p=0.2psns, F=0.5J/cm^2, λ=780nm. Momma *et al.* (1997).

One of the first papers examining the differences in laser-target interaction using ps and ns pulses was by Corkum *et al.* (1990). It concluded that for copper and molybdenum the threshold fluence for damage of the target for pulses less than 1ns was independent of pulse duration. This is not borne out by Rosenfeld and Campbell (1996) who show different thresholds at 130ps and 8ps for both gold and nickel

targets in the form of films. They show that the thresholds at 130ps and 8ps for nickel film targets greater than 1μm in thickness are ~0.5cm^2 and ~0.2J/cm^2 respectively and for gold they are ~0.75J/cm^2 and 0.05J/cm^2 respectively. In addition they also show that the fluences required for ablation at ns pulse lengths are far higher than for shorter pulse lengths, with the threshold fluences for nickel being 1.5J/cm^2 for 15ns pulse length and for gold being 2.0J/cm^2 for 20ns. These compare favourably with measured values in Table 5.3.

Limited work has been carried out on the effects of pulse length on film quality. Muller *et al.*(1993) investigate the effect of using 500fs and 30ns pulse lengths on the film qualities of diamond like carbon (DLC) films, copper films and silicon films. For both DLC and silicon films there is an improvement in film quality with 500fs pulse length. For silicon this is borne out by the decrease in the number of droplets on the films deposited using fs pulse lengths. This correlates well with the damage observed on the targets, with larger cone structures being present from the ns ablation and smaller structures with fs pulses, in accordance with the droplet sizes observed. For the DLC film improved structural qualities are obtained with the fs pulse lengths. The copper ablation characteristics are not necessarily in agreement with other observed characteristics at short pulse lengths. Muller *et al.* (1993) report a higher deposition rate using fs pulses than ns pulses due to a more peaked angular distribution on the ablation plume with fs pulses. In addition the deposition rate saturates. In the fs regime this is likely to be due to the increase in kinetic energy of the plume species which cause sputtering at the substrate surface. In contrast the deposition rate does not saturate with ns pulses. The higher power density is found to give a lower threshold fluence as demonstrated by many authors. Although droplets are still present on the copper films deposited using ns pulses the fs films are found to have a sub-micron granular texture which leads to highly porous films. This may arise because, in the absence of melting at fs pulse lengths, fragments are removed from the copper target by an exfoliation method, Kelly *et al.* (1985b). The outcome of this work appears to be that 500fs pulses work well to improve the film quality of silicon

and DLC but are less effective for copper films, which appear to be free of droplets arising from the target melt at this short pulse length but still do not have good film quality.

Kononenko *et al.* (1997) show ablation rates of AlN ceramic at different pulse lengths and they do not appear to be affected in the same way as metals. At 1078nm the ablation of AlN is greater for ps than ns pulses whilst at 539nm the deposition is less for ps than ns pulses. For steel however it is generally found that ns pulse ablation rates are greater than ps pulse ablation rates. The comparison of these results with those presented in this thesis is difficult since the fluences are so different. Maximum fluences used in this thesis are $20J/cm^2$ in the ns regime and $10\times10^{-3}J/cm^2$ in the ps regime. The work presented by Kononenko *et al.* (1997) covers fluences up to $10^4J/cm^2$ and gives very little data at the low end of the scale corresponding with fluences used in this thesis.

When moving to shorter pulse lengths it is generally understood that heat diffusion into the targets followed by melting is no longer valid. The processes involved in the ablation of materials using short pulses are less clearly understood. Multiphoton ionisation, Joule heating and collisional ionisation are processes that have been suggested for ablation at short pulse lengths, see for example Stuart *et al.* (1995) and Du *et al.* (1994).

1.7 A Review of Metallic Films and Multilayer Samples Fabricated by PLAD and Other Deposition Techniques.

Metallic multilayer samples are deposited with two main objectives, either for use as a device showing giant magnetoresistance (GMR) or as x-ray mirrors. The deposition of multilayers has largely been carried out using sputtering and molecular beam epitaxy (MBE), with sputtering being most commonly used. In the second half of this chapter the deposition of a range of multilayer devices by PLAD and other deposition techniques are discussed. Particular emphasis is placed samples prepared by PLAD and also on multilayers incorporating the noble metals specifically but prepared mainly by sputtering. Both of these aspects allow comparisons to be made

with the $Ni_{0.8}Fe_{0.2}$/Pt multilayers presented in chapter 6. However before discussing multilayer samples a comparison of metallic films deposited by PLAD, sputtering and thermal evaporation is presented.

1.7.1 A comparison of metallic films deposited by PLAD, sputtering and thermal evaporation

Hubler (1994) compares different deposition techniques and shows that PLAD provides ions in the desired energy range for deposition compared to the commonly used sputtering. Consequently we see that sputtered, thermally evaporated and PLAD films have largely the same characteristics Krebs *et al.* (1995a, 1995b, 1997). Some differences between films deposited via sputtering and PLAD are however reported. For example, smaller grain sizes were observed in iron, niobium, silver, titanium and tungsten films deposited by PLAD (Krebs *et al.*, 1995a). Larger lattice spacings were also observed in the growth direction of Fe and Ag films deposited by PLAD compared to the bulk.

Texturing was another feature of films deposited via PLAD. For example, texturing of Fe and Ag films gave rocking curve widths of 0.5° compared to 1° in sputtered films (Krebs *et al.*, 1995b). Unusual compositions of alloys were obtained in films deposited by PLAD. Similar features were observed for alloys as well (Krebs, 1995a). Larger lattice spacings were reported in Fe-Nb, Fe-Ag, Ni-Ag, Cu-Co, Co-Cr and texturing was also a feature of alloy deposition (Krebs, 1997). In addition alloy films were subject to unusual compositions. For example, single phase Fe(Nb) was achieved with 13 atomic% (at%) Nb, whereas for sputtered films two phases existed, a Fe(Nb) phase with 11 at% Nb and as amorphous Fe-Nb phase. This latter phase was not present in the PLAD films. A supersaturated Ni(Ag) phase with 20 at% Ag was also achieved by PLAD.

Krebs *et al.* (1995a and b) ascribe the differences in PLAD films, compared with sputtered and evaporated films, to the high instantaneous deposition rates achieved by PLAD. These can be up to 10^5 times higher than for sputtered/thermal evaporation rates which are of the order of 0.1nm/s. In addition, the average kinetic

energy of the species in the ablation plume is generally considered to be higher than the species deposited by sputtering/evaporation. This is particularly true when the fluences used in PLAD are considerably higher than the ablation threshold, i.e.,~10J/cm^2. These factors all have implications for the growth mechanism and can give rise to some different features of films deposited via PLAD.

1.7.2 PLAD and the deposition of multilayers

The deposition of multilayer devices by PLAD has by no means been exhaustively researched. Indeed the use of PLAD for metal film deposition is still developing with the literature on this subject expanding (Lunney, 1995; Kools, 1994). Initial multilayers deposited by PLAD were for use as x-ray mirrors. Gapanov *et al.* (1979) carried out the earliest work depositing multilayers by PLAD. This work showed the possibility of heteroepitaxial deposition of a range of semiconductor films, such as InSb-CdTe, and demonstrated the use of PLAD for successful layer deposition. Gapanov and co workers continued to deposit a range of multilayer devices for use as x-ray mirrors with considerable success (Gapanov *et al.*, 1983; Akhsakhalyan *et al.*, 1984).

Uniformity is of utmost importance in such mirrors. In order to achieve high reflectivity in the 14-17nm wavelength range layer thicknesses of ~0.5nm and an interface roughness of the order of 1-2 atomic layers are required. The problem of achieving sharp interfaces between layers was discussed by Mai and Pompe (1992) where good interfaces were achieved in carbon/nickel and carbon/tungsten mirrors. Improved interface sharpness was achieved by ensuring that the deposition species fell within a certain energy range. Different energy ranges promote different growth regimes at the film surface. For example, for incident ions with energy ~0.1eV, 3D growth is promoted since ions have insufficient energy for surface diffusion once they are deposited at the surface. At higher energies, ~10eV, layer by layer growth occurs at the substrate. As long as the incident energy is less than the displacement energy (~30eV) the incoming species have sufficient energy to be mobile on the film surface after impact. Above 30eV atomic mixing of layers occurs which gives rise to a loss of

interface sharpness (Kools, 1994). The energy of the incoming species can be controlled by using different fluences. Although Mai and Pompe (1992) do not explicitly state the fluences at which their multilayers were deposited they do discuss how choosing appropriate ablation conditions can optimise the energy of the species in the ablation plume to obtain good interfaces in multilayer samples. This enabled Mai and Pompe to deposit layers with thicknesses ranging from 1-10nm with interface roughness <0.5nm. A similar amount of interface roughness, ~0.6nm, is observed by Enrech *et al.* (1994) in Co/Pd multilayers deposited by PLAD.

Krebs *et al.* (1997) compares multilayer samples deposited by PLAD and sputtering. In the case of Fe/Nb multilayers interface mixing is found to be more pronounced in the case of PLAD samples than sputtered samples. However Fe/Ag and Pd/Nb multilayers were successfully deposited by PLAD with interface roughness of around one to two monolayers. In the case of Fe/Nb the system has a negative heat of mixing, whilst for Fe/Ag and Pd/Nb systems the heat of mixing is positive. This plays a major role in the definition of the deposited multilayers. Thus it is the high instantaneous deposition rates and atomic mixing which affect the quality of multilayer samples. This intermixing at the interface is a feature observed by others. Geilman *et al.* (1997) show intermixing of Fe/Al multilayers and find that the mixing is dependent upon whether Al is deposited on to Fe or Fe deposited on to Al, as well as showing that intermixing is more prominent in PLAD than thermal evaporation. A similar asymmetry in interdiffusion at Ni/W interfaces is seen by Rothman *et al.* (1997) with the diffusion being 2nm for Ni on W and 1.3nm for W on Ni. Intermixing problems are also encountered in the fabrication of Mo/Si multilayer soft x-ray reflectors by PLAD (Kim *et al.*, 1998). In addition droplets were also present on the deposited multilayers. An attempt to eliminate these droplets was made by using a shorter wavelength and by using two synchronised laser pulses, as described in section 1.5. However the droplets were not completely eliminated. Analysis of these Mo/Si multilayers by x-ray reflectivity revealed asymmetric interdiffusion as for the Al/Fe

multilayers deposited by Geilman *et al.* (1997). This led to a lower reflectivity at normal incidence being measured.

Some work has been carried out on the deposition of multilayer samples for giant magnetoresistance devices. For example Kools *et al.* (1993) deposited Co/Cu multilayers. The deposition was carried out in UHV which, as discussed in section 1.3, is desirable for good metallic deposition at a relatively low fluence of $3J/cm^2$ and a chopper was also used to minimise the number of droplets deposited on to the films (see section 1.5). The samples were deposited onto Si(100) and an example of one structure was $Si(100)/20nmCu(1.0nmCu/1.6nmCo)_{25}$. XRD spectra of these samples revealed that the FWHM of the x-ray peaks were comparable to those seen in sputtered samples.

The nature of PLAD means that in theory the layer thickness can easily be controlled by the number of pulses provided the deposition per pulse is known. In practise, however, variations in the deposition per pulse arise, increasing the difficulty with which uniformity in layer thickness can be achieved. Kools (1992) observes that this variation in the deposition rate per pulse can be as much as 10%. Macquart *et al.* (1991) have had similar success in depositing W/C x-ray multilayer mirrors to Mai and Pompe (1992). They report an interface roughness of 0.4nm with good reflectivity. However variations in layer thickness arise which are detrimental to the quality of the mirrors. Thus we see that roughness arising at interface as a result of mixing and the variation in the deposition per pulse are major limiting factors when using PLAD for the deposition of metallic multilayers. These are problems experienced in this thesis and are discussed in chapter 5.

The extent of the published work on the PLAD of metallic multilayers is fairly limited, due mainly to the difficulties encountered in PLAD and also to the success of sputtering in this area.

1.7.3 Nobel metals used in giant magnetoresistance multilayer devices

This section reviews the use of multilayer devices deposited by methods other than PLAD to obtain giant magnetoresistance (GMR). Particular attention is paid to

multilayers which have noble metals as non-magnetic spacer layers and Ni, Fe or an alloy of Ni and Fe as the magnetic layer, since such devices follow the basic structure of the multilayers presented in chapter 6. A comprehensive review of metallic multilayer devices showing GMR is given by Parkin (1995). Parkin (1995) discusses a wide range of multilayer systems, for example Co/Cu, Fe/Cr and granular alloys of Co/Cu also exhibiting GMR. The oscillatory behaviour of interlayer coupling arising from changing the non-magnetic spacer layer thickness and other spin engineered devices are discussed. Of particular interest are the multilayers of permalloy/gold ($Ni_{0.8}Fe_{0.2}$/Au) for comparison with multilayers discussed in chapter 6. (The alloy $Ni_{0.8}Fe_{0.2}$ known as permalloy will be abbreviated to Py).

The original reports of GMR were in 1988 by Baibich *et al.* (1988) and Binasch *et al.* (1989). They reported GMR values of 5% in Fe/Cr multilayers and up to 3% in Fe/Cr/Fe sandwiches at 4.2K respectively. However the fields required for magnetic saturation were large and thus the devices were not suitable as low field sensors. Once GMR was discovered a whole range of multilayer systems were investigated. An important aspect in the multilayer system was found to be the choice of non-magnetic spacer layer. A popular choice for the layer was Cu followed by other transition metal (TM) spacers. Parkin (1991) began to show that a systematic variation of the interlayer coupling strength existed. He investigated eleven different 3d, 4d and 5d transition metals sandwiched between Fe, Co, Ni and Ni alloy layers. The coupling strength was seen to increase from the 5d to 4d to 3d metals and also increased exponentially as the d-band of the spacer layers filled across the 3d, 4d and 5d periods. Thus the variation in the coupling strength was dependent upon the position of the transition metal spacer layer element in the periodic table. The trends in interlayer coupling strength are summarised in Table 1.1.

Ti NC	V	Cr	Mn	Fe FM	Co FM	Ni FM	Cu
Zr NC	Nb	Mo	Tc	Ru	Rh	Pd NC	Ag NC
Hf NC	Ta	W	Re	Os	Ir	Pt NC	Au NC

Table 1.1 Part of the periodic table summarising the interlayer coupling strength of transition metals, as observed by Parkin (1991). FM=ferromagnetic, NC=no coupling, → increase in coupling strength. In some cases coupling was observed subsequent to this work, see for example Parkin (1994).

For example the coupling strength increases along the period from V or Cr or Cu and up a column from W to Mo to Cr in the case of Co/TM multilayers Similar behaviour was also reported for multilayers of Fe/TM, Ni/TM, Py/TM and $Ni_{0.8}Co_{0.2}$/TM. However at this time coupling was not observed for all the transition metals, for example in Co/TM multilayers containing Pd, Ag, Pt or Au. Structural defects were cited as a possible explanation for the lack of antiferromagnetic coupling. The coupling in Co/Au layers had however been observed by Dupas *et al.* (1990).

Further work on multilayer systems containing Au, i.e., Co/Au (Grolier *et al.*, 1993), Py/Au (Parkin *et al.*, 1994) and Fe/Au (Shintaku, 1993) showed the oscillation of the antiferromagnetic coupling between magnetic layers with inter layer thickness previously observed by Parkin *et al.* (1990). Despite showing this oscillatory behaviour no simple variation in the antiferromagnetic coupling with spacer layer thickness has been established (Parkin, 1995).

The results of Parkin (1991) enabled spacer layers showing weak coupling between magnetic layers to be identified. Thus weakly antiferromagnetically coupled magnetic multilayers could be deposited in which saturation occurs at low magnetic fields, leading in turn to increased sensitivity in the GMR of the device. Thus according to Parkin (1991), Au shows weaker coupling than Ag, which shows weaker

coupling than Cu. Therefore we might expect that multilayers containing Au would have a higher GMR sensitivity and saturate at lower applied magnetic fields than similar multilayers containing Cu or Ag. This is demonstrated by considering Hylton *et al.* (1993) and Parkin *et al.* (1994). Hylton *et al.* (1993) reported GMR values >2% at room temperature in sputtered Py/Ag multilayers, with a sensitivity of 5-12%/mT. In comparison Parkin *et al.* (1994) reported the lowest saturation field obtained in metallic multilayers at room temperature from sputtered Py/Au samples with sensitivities ~10-20%/mT. These sensitivities are generally higher than for the similar samples with Ag spacer layers. Other multilayers containing Ag, for example Ni/Ag (Yang *et al.*, 1994; Rodmacq *et al.*, 1992) and Py/Ag (Rodmacq *et al.*, 1993) show GMR up to 8%. However saturation fields in these cases are of the order of 1.6MA/m ($\mu_0 H$=2T), therefore the same sensitivity is not achieved. We see that the sensitivity of the Py/Ag multilayers produced by Hylton *et al.* (1993) is not achieved by Rodmacq *et al.* (1993), and indeed Parkin (1991) does not initially report coupling in Py/Au, implying that the deposition conditions of such multilayers are critical. Thus in this thesis multilayers of Py/Pt are investigated. According to Parkin (1991), Pt should show weaker coupling than Au and may therefore result in an increase in the GMR sensitivity and the reduction in the saturation field. However the critical deposition conditions do not make fabrication of Py/Pt devices showing GMR easy.

Chapter 2

2 Pulsed Laser Ablation Deposition Models

2.1 Introduction

There are two aspects of pulsed laser ablation deposition (PLAD) which need to be addressed: the laser-target interaction, which constitutes the laser ablation process, and the deposition of material onto the substrate. The ablation process encompasses the mechanisms by which material is removed from the target as a result of energy supplied by the laser. The removal of material from the target is principally through plasma formation but may also be achieved by the formation of molten droplets. The ablation process also extends to the effect that the forming plasma has upon the laser-target interaction. These processes may have consequences for the deposition of material onto the substrate. In addition the deposition of material onto the substrate may be affected by the interaction of the plasma and the film forming at the substrate. Aspects of both the laser ablation and deposition processes are discussed in this chapter.

2.2 Laser-Target Interaction: The Ablation Process

This section introduces the kinetic model for the heating and removal of material from the target. The kinetic model assumes that the energy supplied to the target by the laser is entirely involved in the heating, melting and evaporation of material from the target surface and ignores the process of plasma formation. It also assumes that the laser pulse length is sufficiently long that the time taken for energy transfer (from the electrons to the lattice of the solid) may be neglected. By making these assumptions we can introduce the thermal diffusion depth, L_{th}

$$L_{th}=(2\kappa\tau_p/c_{pm}\rho_m)^{1/2} \qquad (2.1)$$

where κ is the thermal conductivity, c_{pm} is the molar specific heat capacity, ρ_m the molar density, and τ_p the laser pulse length and is taken as 20ns throughout this chapter unless otherwise stated.

A second parameter of importance in PLAD is the optical absorption depth, α^{-1}, given by

$$\alpha^{-1}=\lambda/4\pi k \qquad (2.2)$$

where λ is the laser wavelength and k is the extinction coefficient. These two parameters determine the depth to which the laser energy is absorbed into the target (Preuss *et al.*, 1994). The dependence of L_{th} on τ_p and α^{-1} on λ suggests that the laser wavelength and the laser pulse length have a direct effect on the ablation process. This is illustrated in figure 2.1 where the effect of altering the pulse length on the magnitude of the thermal diffusion length in relationship to the optical absorption depth is seen in metals where $L_{th}>\alpha^{-1}$ with L_{th}~1μm for τ_p=20ns and α^{-1}~20nm and L_{th}~10nm for τ_p=5ps at ultraviolet (UV) wavelengths. We also see how these parameters vary in different materials. For example in YBCO $\alpha^{-1}>L_{th}$ with L_{th}~10nm for a 20ns pulse length compared with α^{-1}~50nm (Gavigan, 1990).

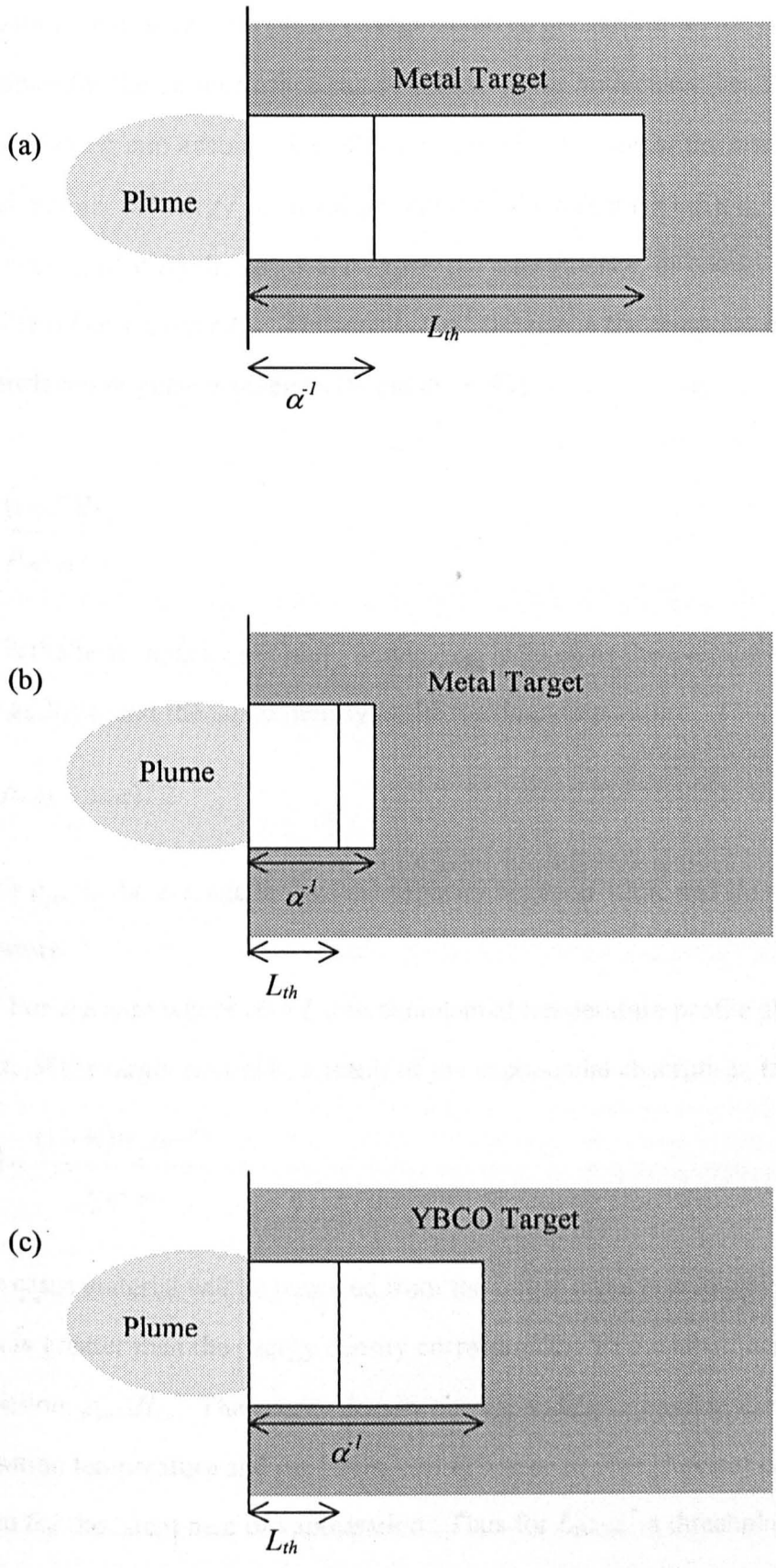

Figure 2.1 Schematic representation of L_{th} and α^{-1} for (a) metal target and ns pulse lengths (b) metal target and ps pulse length and (c) YBCO target and ns pulse length at UV wavelengths.

If we assume that there is no phase change in the target surface then a peak temperature for the target surface can be estimated for both cases, i.e., $L_{th}>\alpha^{-1}$ and $\alpha^{-1}>L_{th}$. Taking into account the reflectivity, R, of the target at the laser wavelength the total amount of energy absorbed per pulse by the target is $(1-R)I\tau_p$, where I is the laser power irradiating the target and $I\tau_p=F$ the laser fluence, or energy density on the target. This heats a layer L_{th}. Thus for $L_{th}>\alpha^{-1}$ the rise in the temperature of the target surface per pulse is given as (Saenger, 1993)

$$\Delta T_s \approx \frac{(1-R)I\tau_p}{\rho_m c_{pm} L_{th}} \tag{2.3}$$

$\rho_m c_{pm}$ is the heat capacity per unit volume. ρ_m is taken as the average of the solid density at 300K and the liquid density at the melting temperature. Thus

$$\rho_m = (\rho_{m,(s)} + \rho_{m,(l)})/2 \tag{2.4}$$

Similarly c_{pm} is the average molar heat capacity between 300K and the vaporisation temperature.

For the case where $\alpha^{-1}>L_{th}$ an exponential temperature profile along the depth, z, of the target occurs as a result of the exponential absorption, thus

$$\Delta T_s(z) \approx \frac{(1-R)I\tau_p \alpha e^{-\alpha z}}{\rho_m c_{pm}} \tag{2.5}$$

In both cases material will be removed from the target if the heat supplied per unit volume is greater than the energy density corresponding to the latent heat of vaporisation, $\rho_m \Delta H_{lv}$. The energy density corresponding to heating the target to the vaporisation temperature and the latent heat of fusion are insignificant compared to the term for the latent heat of vaporisation. Thus for $L_{th}>\alpha^{-1}$ a threshold fluence can be determined

$$F_{th} = \frac{\rho_m \Delta H_{lv} L_{th}}{(1-R)} \tag{2.6}$$

The threshold fluences for nickel and silver are calculated at 193nm, 248nm and 351nm using his model and the results are presented in Table 2.1 below where L_{th}=6.8μm for silver and 2.6μm for nickel.

Wavelength	Nickel J/cm^2	Silver J/cm^2	Reflectivity of nickel	Reflectivity of silver
193nm	5.9	8.0	0.37	0.24
248nm	6.5	8.1	0.43	0.25
351nm	6.9	33.7	0.46	0.82

Table 2.1 Shows the threshold fluences calculated using equation 2.6 at three laser wavelengths and the reflectivities used in the calculations (CRC, 1992). The values used in the caluclation are τ_p=20ns, L_{th}=6.8μm for silver and 2.6μm for nickel and ΔH_{lv}=378.8kJ/mol for nickel and 254.2kJ/mol for silver (CRC, 1992).

These values are higher than the threshold fluences measured for nickel and silver in section 5.3.1. This is because in this simple model the energy required to overcome the latent heat of vaporisation is significant. The high value for silver at 351nm is related to the high reflectivity at this wavelength. During the ablation process the roughening of the target may reduce the reflectivity thereby reducing the calculated threshold closer to the observed values.

By using a kinetic model an expression for the amount of material removed from a target can be calculated. Such a model is outlined by Kelly and Rothenberg, (1985a). It equates the flux of material removed from the target as a result of the increase in the energy supplied by the laser with the flux of molecules condensing at the surface. In keeping with the kinetic model we can assume that the laser pulse

length has a top hat temporal profile. For example an estimate of the time to reach the vaporisation temperature can be obtained by rearranging equation 2.3 which gives the heating rate as

$$\text{Rate} \approx \frac{I(1-R)}{L_{th}\rho_m c_{pm}} \tag{2.7}$$

Hence for 20ns pulses the rise time in metals is $3\text{x}10^{-9}$s, this is ~15% of the complete pulse length. Therefore within the length of the pulse there is time for the target surface to reach the vaporisation temperature for fluences of the order of 10J/cm^2.

From the kinetic theory of a perfect gas an expression for the fraction of molecules with mass m, travelling between velocities u and $u+\text{d}u$, normal to the target surface can be obtained, assuming the velocities follow a Boltzmann distribution as outlined in Tabor (1979). This fraction is given by

$$\frac{\text{d}n}{n} = \left(\frac{m}{2\pi\text{k}T}\right)^{1/2} \exp\left(-\frac{mu^2}{2\text{k}T}\right)\text{d}u \tag{2.8}$$

where T is the temperature of the gas and k the Boltzmann constant. Using a one-dimensional model the number of molecules hitting the surface of a liquid per unit area per unit time can be determined. Consider molecules with velocities u to $u+\text{d}u$ in a volume with unit cross sectional area and length u. The number of molecules in this volume, u, with velocity u is $u\,\text{d}n$, where $\text{d}n$ is the number per m^3 and these will all strike the surface in one second. The total number of molecules is the integral of $u\,\text{d}n$ with the limits of 0 to ∞, which takes into account only those molecules heading toward the surface. From equation 2.8 the integral is evaluated to give

$$\text{Condensing flux} = p_{vs}(2\pi m\text{k}T)^{-1/2}\ \text{atoms/m}^2\text{s} \tag{2.9}$$

where p_{vs} is the vapour pressure that would exist in equilibrium. In such a condition the condensing flux is equal to the vaporising flux. Therefore

$$\text{Vaporising flux} = \text{p}_0\{\exp(-\Delta H_{lv}/\text{k}T)\}\ (2\pi m\text{k}T)^{-1/2}\ \text{atoms/m}^2\text{s} \tag{2.10}$$

where p_0 is a constant and ΔH_{lv} is the latent heat of vaporisation. The exponential term gives the probability of atoms having sufficient energy to leave the surface. Thus an expression for the depth of material removed per pulse can be derived as

$$\text{depth}/\text{pulse} = \left(\frac{p_0}{N}\right)(2\pi m\text{k})^{-1/2}\int_0^{\infty}\exp\left(\frac{\Delta H_{lv}}{\text{k}T}\right)T^{-1/2}\,\text{d}t \qquad (2.11)$$

where N is the number density in the condensed phase. From equation 2.3 we see that for $0<t\leq\tau_p$ then $\Delta T\propto t^{1/2}$. At times greater than τ_p then $\Delta T=\Delta T(\tau_p)+(\partial\Delta T/\partial t)_{\tau p}(t-\tau_p)$. If equation 2.11 is integrated and the units converted from T to t the following expression for depth/pulse is obtained.

$$\text{depth/pulse} \approx \frac{p_{vs}T_s^{1/2}\tau_p}{M^{1/2}\Delta H_{lv}}\text{x}1.53\text{x}10^6\,\text{nm/pulse} \qquad (2.12)$$

M is the molecular mass in mass units u, ΔH_{lv} is in eV/atom, T_s is the surface temperature of the target and p_{vs} is in atmospheres. To calculate this quantity the boiling point temperature is used as this is the scope of the kinetic model presented. Values for nickel and silver are 0.057nm/pulse and 0.055nm/pulse respectively. These values are compared with ablation rates measured from nickel and silver targets in chapter 5.

2.3 Formation of the Plasma

The model presented above describes evaporation from the target surface, however the PLAD process is sufficiently energetic to form a plasma. Thus the formation of the plasma is briefly introduced in this section. The plasma is the primary method by which material is removed from the target. Phipps and Dreyfus (1993) discuss the different regions of the forming plasma in detail. Four regions are identified. Firstly a dense region close to the target where the plasma density is as high as 10^{21}-10^{23}cm^{-3}, i.e., very close to solid values. These densities are high enough for some absorption to occur through inverse Bremsstrahlung and other absorption processes, as discussed in the following section. This region extends for only a few hundred nanometers, of the order of the laser wavelength and one-dimensional

expansion takes place. Beyond this region the plasma density decreases to below $10^{21}cm^{-3}$ and expansion is three-dimensional. Due to the high number of collisions this expansion is beam like in behaviour. Such expansion forms a Knudsen layer (Phipps and Dreyfus, 1993). In the third region the number of electron collisions decreases significantly and the plasma density drops to between 10^{16}-$10^{12}cm^{-3}$. Some absorption may still be possible at longer wavelengths and longer pulse lengths. Finally in the outer region of the plasma energetic electrons escape from the plasma and a thermal distribution of ions continue to expand outwards to reach the substrate.

2.3.1 Absorption by Inverse Bremsstrahlung

The formation of a plasma of significant density can absorb incoming laser radiation primarily through inverse Bremsstrahlung. One of the consequences of such absorption is the reduction in the amount of laser energy reaching the target, which in turn reduces the amount of material removed. Inverse Bremsstrahlung is the opposite process to Bremsstrahlung radiation where the emission of photons occurs as a result of electrons being involved in inelastic collision with ions. In the case of inverse Bremsstrahlung absorption, free electrons oscillating in the electromagnetic field at the laser frequency collide with ions in the plasma. This distorts the oscillating motion thus heating the plasma. The energy dissipated to the plasma in the form of heat is obtained from the absorption of photons from the laser radiation.

In order for such absorption to occur the plasma frequency ω_p, must be greater than the frequency of the incoming photons. The plasma frequency is governed by the electron density n_o and is given as

$$\omega_p = \sqrt{\frac{n_o e^2}{m_e \varepsilon_0}} \qquad (2.13)$$

where e is the electronic charge and m_e the mass of the electron. For UV wavelengths ω for the laser is ~5-10x$10^{15}s^{-1}$. Thus for absorption to occur via inverse Bremsstrahlung the electron density must be ~$10^{22}cm^{-3}$. Whether such densities, and consequently significant absorption by inverse Bremsstrahlung can be achieved in

metal ablation using UV wavelengths is questionable. Phipps and Dreyfus (1993) suggest that very close to the target densities of up to $10^{23}cm^{-3}$ are possible. Increased ionisation at shorter UV wavelengths compared to IR wavelengths may occur and thus increase the chances of achieving high enough densities. Despite this they comment that although absorption via inverse Bremsstrahlung does occur it is not significant enough at UV wavelengths to shield incoming laser energy from the target. More recently Hermann *et al.* (1998) extrapolate electron densities $\geq 10^{19}cm^{-3}$ at $t=0$. This also suggests that absorption via inverse Bremsstrahlung will be negligible at UV wavelengths if indeed it occurs at all. In chapter 5 saturation in the deposition rates of nickel and silver is observed. However in the light of this discussion absorption via inverse Bremsstrahlung is not pursued as a likely explanation for this saturation.

2.4 The Deposition of Material onto the Substrate

There are distinct differences between the deposition of films by PLAD and other methods. For example the pulsed nature of PLAD involves a high instantaneous influx of material followed by a long period before the next pulse. For τ_p~20ns the deposition of the plasma onto the substrate occurs over ~1ms (Horwitz and Sprague, 1994). If the laser repetition rate is 20Hz then the time between pulses is 50ms. In contrast to other deposition techniques the flux of incoming material is constant.

Another difference with PLAD is the energy of the depositing species. For example the species impinging upon the substrate have an average energy of up to 1000eV (Horwitz and Sprague, 1994) compared with several hundred for sputtering and only a few eV for MBE. The range of energies and species within the plume are also diverse with ions of energy up to a few keV and neutrals with energies of several eV.

As a result of these differences the nucleation and growth of films by PLAD does not follow the standard mechanisms such as Volmer-Weber (three-dimensional island growth), Frank-van der Merwe (two-dimensional monolayer growth) or Stranski-Krastinov (two-dimensional growth of monolayers followed by three-

dimensional island nucleation). An alternative theory of film growth via PLAD has been developed by Metev and Meteva (1989) and Kashchiev (1977). This involves the simultaneous filling of monolayers governed by a time constant. The time constant of film growth plays an important role in governing the deposition conditions for film growth via PLAD (Metev, 1994).

2.4.1 Sputtering of the depositing film

In addition to the these possible nucleation and growth modes another process that can occur is the sputtering of depositing films by the incoming ions from the plasma. This can give rise to reduced deposition rates being observed in PLAD. A situation might arise where material already deposited on the substrate is removed by incoming ions thus preventing the deposition rate from increasing continuously with increasing laser fluence. Such a situation would arise where the incoming plasma species are highly energetic, i.e., 100-1000eV (Metev, 1986; Jordan *et al.*, 1995). The removal yield $Y(E)$, atoms/ion, for low energy incident ions E(keV) can be expressed as

$$Y(E) = \frac{1.9}{U_0}\sqrt{\frac{Z_f}{f}}\left(\sqrt{E} - 0.09\sqrt{U_0}\right) \qquad (2.14)$$

where U_0 is the sublimation energy of the film on the substrate and Z_f is the atomic number of the film. The value of f is given by

$$f = \frac{\left(\frac{Z_p}{Z_f}\right)^{2/3} + \left(\frac{Z_f}{Z_p}\right)^{2/3}}{2} \qquad (2.15)$$

where Z_p is the atomic number of the projectile, i.e., from the ablation target (Zalm, 1984).

The expression is valid for ion energies ≤ 1keV. This is suitable for use in PLAD since ion energies in the plasma range up to 1000eV. For PLAD ions in the region of 100eV are of interest for deposition (Hubler, 1994). Since f only varies slowly with (Z_p/Z_f), the yield expression suggests that sputtering yield is mostly

dependent on the projectile energy and not their species. With higher energy ions present in the plume at high fluences (Jordan, 1995) one would expect a greater degree of sputtering from the film. Sputtering yields for silver depositing onto silver and nickel and nickel depositing onto silver and nickel are shown in figure 2.2. Values for U_0 are for nickel= 4.46 eV/atom and for silver=2.96 eV/atom, (CRC, 1992). These yields are discussed with respect to the observed deposition rates of nickel and silver that are presented in section 5.2.

2.4.2 Models for droplet production

Models predicting the origin of droplets and consequently their size are found in Kelly and Rothenberg (1985a), Bennett *et al.* (1995) and Dreyfus *et al.* (1994). Considering the Kelly and Rothenberg (1985a) model first, the formation of droplets is expected if the amount of material removed from the target is greater than the removal rate measured at the target surface. Such a comparison between calculated removal rates due to vaporisation and measured ablation rates is carried out for nickel and silver in section 2.5.

An expression for the radius of droplets is obtained by considering the change in dimension ΔL that a forming asperity undergoes due to thermal expansion. The force F that the forming asperity has to over come in order to separate from the molten surface is given by

$$F = \frac{-\partial\left(4\pi r^2\gamma\right)}{\partial r} = 8\pi r\gamma \qquad (2.16)$$

It is assumed that the asperity is spherical and that γ is the surface energy of the molten surface. Provided that the momentum of the forming droplet exceeds the product of $F\Delta t$, where Δt is the difference in time of the pulse length and the time taken to melt the target surface, i.e.,

$$\frac{4\pi r^3 10^3 M_{mol}\rho_{m,(l)}}{3}\frac{\Delta L}{\Delta t} > 8\pi r\gamma\Delta t \qquad (2.17)$$

where M_{mol} is the molar mass in g/mol and

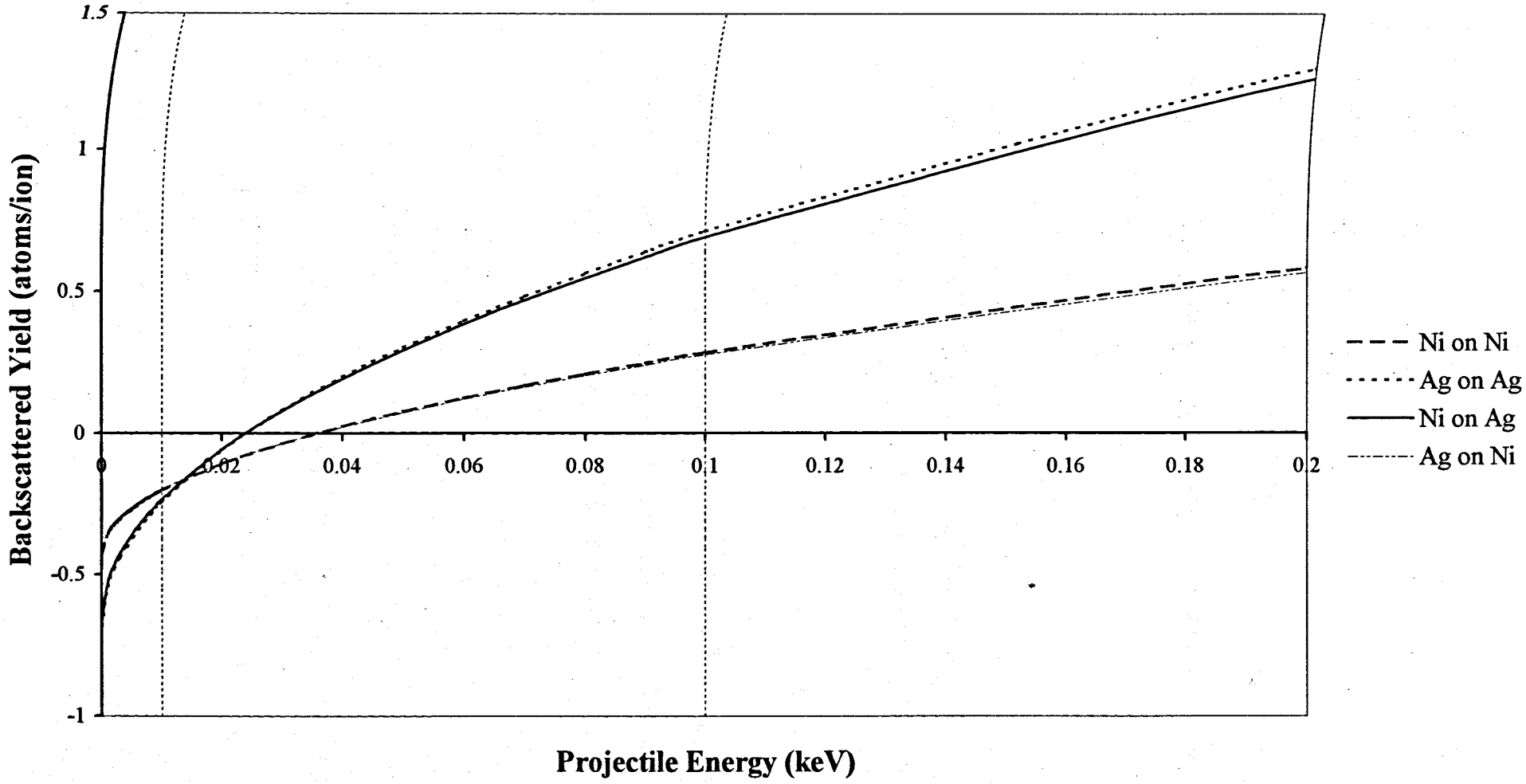

Figure 2.2 Yield of atoms from nickel and silver films, Zalm (1984). Values at 10eV and 100eV are indicated.

$$\Delta t = \tau_p \frac{T_s - T_m}{T_s} \tag{2.18}$$

with T_s and T_m being the surface temperature of the target and the melting point temperature respectively, then

$$\Delta L = 2r\xi(T_s - T_m) + 2r(\rho_{m,(s)} - \rho_{m,(l)})/3\rho_{m,(s)} \tag{2.19}$$

with ξ being the coefficient of linear thermal expansion. Thus a minimum droplet size, r_{min}, can be obtained

$$r_{\min} = \left\{ \frac{3\sigma 2r}{10^3 M_{mol} \rho_{m,(l)} \Delta L} (\Delta t)^2 \right\}^{1/3} \tag{2.20}$$

In Bennett *et al.* (1995), the emission of droplets is explained in terms of the acceleration of the surface melt and Rayleigh-Taylor type instability. Such instabilities occur when a heavier fluid lying on top of lighter fluid is displaced. This results in a tendency for the fluids to exchange positions making the system unstable. If the inertial forces associated with the acceleration of forming asperities exceeds the surface tension then molten material leaves the surface as droplets. This acceleration arises from the phase change at the liquid-solid interface. Wave-like features formed at the target surface, as a result of instabilities in the melt, are shown to have a 'most dangerous wavelength', λ_D, the characteristic wavelength at which droplet emission occurs. Hence

$$\lambda_D = 2\pi \sqrt{\frac{3\sigma}{10^3 M \rho_{m,(l)} a}} \tag{2.21}$$

and σ is the surface tension, giving a droplet diameter

$$D = \sqrt{\frac{12\sigma}{10^3 M \rho_{m,(l)} a}} \tag{2.22}$$

where a is the mean acceleration of the solid-liquid interface. Hence the acceleration of the melt forms waves which can lead to the expulsion of droplets. The magnitude of the acceleration of the melt due to the phase change is given by

$$|a| = |a_i| \left(\frac{\rho_{m,(s)}}{\rho_{m,(l)}} - 1 \right) \tag{2.23}$$

where a_i is the mean acceleration of the liquid-solid interface determined for $1 J/cm^2$ as $\sim 4.6 \times 10^6 m/s^2$. This gives an acceleration of $0.58 \times 10^9 m/s^2$ for both nickel and silver. Hence from equations 2.20 and 2.22 the minimum droplet sizes for nickel and silver are calculated along with the characteristic wavelengths and presented in Table 2.2. The calculated results give droplet sizes for ns pulses which are of the same order as the droplets found on the films discussed in chapter 5 and are consistent with values in Bennett *et al.* (1995).

Sample	λ_D (μm)	D (μm)	$2r_{min}$ (μm)
Ni	6.7	2.1	2.6
Ag	4.6	1.5	1.9

Table 2.2 Characteristic surface damage wavelength, λ_D and minimum droplet diameters, D and $2r_{min}$ for nickel and silver. (Bennett *et al.*, 1995; Kelly and Rothenberg, 1985a).

2.4.3 Limitations of the kinetic model at shorter pulse lengths

The model for laser-metal interactions shows that when moving to shorter pulse lengths, the time scale in which energy is transferred to the target lattice, i.e., the electron-phonon relaxation time ~1-2ps, is no longer negligible. This implies that within the duration of the pulse there is insufficient time for heating of the target to occur.

The transfer of energy to the target occurs in two stages. Firstly the energy is absorbed by free electrons which thermalise rapidly via electron-electron collision, with a characteristic relaxation time, τ_e. Energy from the electrons is then transferred to the lattice by electron-phonon interactions characterised by τ_l, the electron-phonon relaxation time, where $\tau_e << \tau_l$. By varying the pulse length three situations can arise.

(i) $\tau_e << \tau_p << \tau_l$, i.e., where femtosecond pulses are used for deposition the pulse length is shorter than the electron-phonon relaxation by three orders of magnitude. In this regime L_{th} is confined to the surface and heat conduction into the target can be neglected within the length of the pulse.

(ii) $\tau_e << \tau_l \approx \tau_p$, i.e., for ps pulses the pulse length is at least comparable with the electron-phonon relaxation time. In this regime $L_{th} \approx 10$ nm for metals and the time taken to heat the target may no longer be negligible.

(iii) $\tau_e << \tau_l << \tau_p$, i.e., for ns pulses the pulse length is sufficiently long for extensive heating of the target.

Thus in metals when using shorter pulse lengths for deposition the transfer of energy to the lattice which heats the target does not take place within the duration of the pulse and thus the kinetic model in section 2.2 is no longer valid.

In this thesis ns pulses and shorter ps pulses are used for PLAD, thus we are concerned with the second and third regimes described above. Ablation models within the literature extensively use the assumptions discussed in section 2.4.2 in relation to the kinetic model. This makes it difficult to present a good model for material removal using shorter pulse lengths. The problems associated with using the models described in this chapter at shorter pulse lengths will be discussed in detail in chapter 5.

Chapter 3

3 Magnetoresistance

In chapter 6 the magnetoresistance of multilayer samples is presented. In order to interpret the results three magnetoresistance effects need to be discussed. These are ordinary magnetoresistance (OMR), anisotropic magnetoresistance (AMR) and giant magnetoresistance (GMR).

3.1 Ordinary Magnetoresistance

This is a phenomenon observed in non-ferromagnetic metals where the resistance of the sample varies with applied magnetic field. There are two aspects of OMR, longitudinal and transverse magnetoresistance. In the former the magnetic field is applied such that it is parallel to the current in the sample. This causes the conduction electrons to move in helical paths as a result of Lorentz forces. The radius of curvature of the electrons' path is inversely proportional to the field strength. The increase in the conduction electrons' path results in an increase in collisions and thus an increase in resistance. In the transverse orientation, the magnetic field is applied perpendicular to the direction of the current. This causes conduction electrons to move in a direction perpendicular to both the magnetic and electric fields. Again this increases the conduction electrons' path and therefore increases the number of collisions. In general the magnetoresistance is proportional to the square of the applied field, H^2, at low fields and saturates at high fields (McGuire and Potter, 1975) and transverse MR is greater than the longitudinal MR. The magnetoresistance ratio is given by

$$\text{MR ratio} = \Delta\rho/\rho_0 \qquad (3.1)$$

where ρ_0 is the resistivity in zero field and $\Delta\rho$ is the change in resistivity due to the applied magnetic field. In this case $\Delta\rho$ is positive, i.e., the resistivity increases with increasing applied magnetic field.

The size and shape of the sample can also affect the resistivity, particularly if the mean free path for electron scattering is of the same order as one of the dimensions of the sample. The mean free path in metals at room temperature is 10^{-7}-10^{-8}m. Thus for films greater than 100nm in thickness it is considered that the resistivity is almost the same as for bulk samples, (McGuire and Potter, 1975). When measuring magnetoresistance of films the shape can effect the resistivity, although it is not usually significant (Meaden, 1966). For example in the parallel arrangement, if the radius of the helical path of electrons is larger than the film thickness then we might expect this to have an effect on the resistivity. However the radius of the helical path decreases with increasing field, thus making the constraints placed on the helical electron path by the film thickness less significant at higher fields.

For the perpendicular geometry used in this work the film thickness can have an effect on the resistivity. The geometry is such that with the current and magnetic field in the plane of the film the deflection of the conduction electrons is out of the plane of the film. Since the total film thickness of the samples are of the order of the mean free path, i.e., 50-90nm, the resistivity may be increased in this geometry. Typically the OMR effect is of the order of a few percent in metals at room temperature (Smit, 1951).

3.1.1 Anisotropic Magnetoresistance

In ferromagnetic materials the phenomenon of AMR is observed. In such materials a magnetisation already exists and thus the orientation of the direction of magnetisation with respect to the current and the applied magnetic field becomes important. The transverse and longitudinal geometries still apply to the geometry of the current and the applied magnetic field as for OMR. Resistivities in these geometries are $\rho_{\perp}$ and $\rho_{/\!/}$ respectively. In a polycrystalline sample the magnetic domains are aligned by a small internal field of <5mT, induced by a small applied

magnetic field. The values of $\rho_{\perp}$ and $\rho_{//}$ in this initial alignment are different with $\rho_{//} > \rho_{\perp}$. This initial difference is the anisotropic magnetoresistance, $\Delta\rho_{AMR}$, i.e.,

$$\Delta\rho_{AMR} = \rho_{//} - \rho_{\perp} \qquad (3.2)$$

It is usual to quote magnetoresistance measurements as ratios, thus the normalised AMR ratio is given as

$$\text{AMR ratio} = \Delta\rho_{AMR}/\rho_{ave} \qquad (3.3)$$

where $\rho_{ave} = 1/3\rho_{//ini} + 2/3\rho_{\perp ini}$, with the subscript 'ini' denoting the resistivities of the sample from the initial alignment of the magnetic domains by a low magnetic field. Some of the literature is unclear about this ratio and gives ρ_{ave} as $1/3\rho_{//} + 2/3\rho_{\perp}$, i.e., not the initial values. This suggests that ρ_{ave} varies with the magnetic field and thus does not give a strict normalisation.

At room temperature Smit (1951) shows that from zero field to the field for initial alignment, i.e., <5mT, $\rho_{//}$ increases and $\rho_{\perp}$ decreases, see figure 3.1. However, as the external field is increased to a few Tesla the resistivities $\rho_{//}$ and $\rho_{\perp}$ both decrease. The decrease in resistivity is the same in both orientations, thus $\Delta\rho_{AMR}$ remains constant at higher fields. In making measurements of AMR the resistivity at zero field, rather than initial alignment, is usually taken as these values are similar (McGuire and Potter, 1975). Thus practically the total anisotropic magnetoresistance ratio is taken as the ratio of the difference in $\rho_{//}$ and $\rho_{\perp}$ with the sample fully magnetised and the resistivity with the sample fully demagnetised.

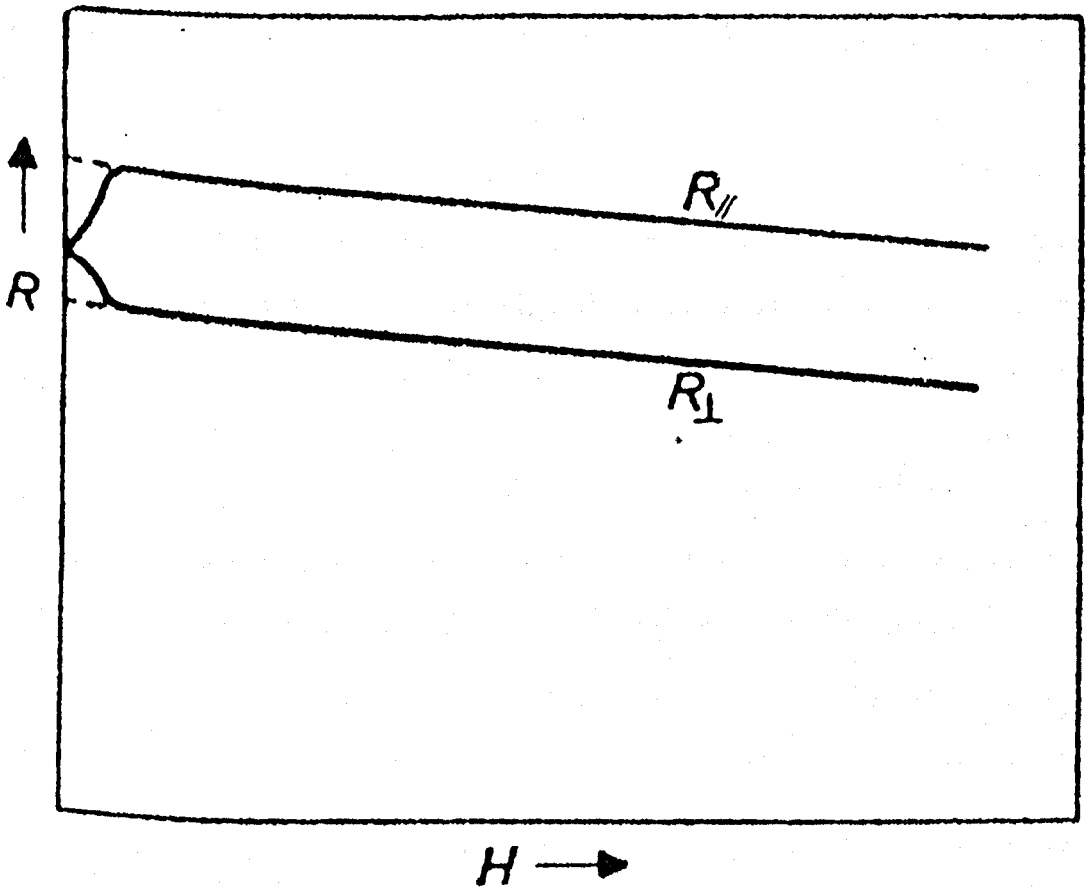

Figure 3.1 A schematic representation of the parallel and transverse resistances of ferromagnetic metals, (Smit, 1951).

In contrast to OMR the overall effect of a magnetic field on a ferromagnetic material is to reduce the resistivity. AMR depends on the direction of the spontaneous magnetisation, whereas OMR depends on the magnitude of the applied magnetic field. In general for AMR $\rho_{//} > \rho_{\perp}$. If the magnetisation of the ferromagnetic sample is considered as having the same effect as an applied magnetic field one would expect the resistance to increase with increasing magnetisation as for the OMR case. Since the reverse effect occurs the OMR model fails to explain AMR. In a simple classical model s-electrons are responsible for conduction and scattering of s-electrons

in to available d-states gives rise to resistance. However the direction of the spin must be preserved in the s-d transition. With this model the effect of an applied magnetic field is to decrease the density of parallel d-states at the Fermi surface with increasing magnetisation, this results in a decrease in the resistance since fewer parallel s-d transitions are possible. However this does not account for the anisotropic MR observed in ferromagnetic materials, i.e., that the resistivity is dependent upon the orientation of the current in the sample and the applied magnetic field. The anisotropy arises as a result of the interaction between the spin system and the lattice via spin-orbit coupling which allows mixing of parallel and antiparallel d-states. Therefore when the s-electrons are moving orthogonally to the orbit, i.e., the current is perpendicular to the applied magnetic field, the simple classical model works and the applied magnetic field reduces the density of available parallel d-states thus reducing the resistance of the sample. However when the s electrons are moving parallel to the orbit, i.e., the current and the magnetisation are parallel, the spin-orbit coupling mixes the parallel and antiparallel states. This increases the density of available parallel d-states thus giving and extra contribution to the resistivity of the sample. This explains why $\rho_{\parallel} > \rho_{\perp}$.

The AMR percentage for a 60nm $Ni_{0.82}Fe_{0.18}$ film was found to be 2.97% (McGuire and Potter, 1975). This is higher than measured for the multilayers discussed in chapter 6 where the thickness of $Ni_{0.8}Fe_{0.2}$ layers within the samples is much less than 60nm.

3.1.2 Giant Magnetoresistance

A spin dependent scattering model can be used to explain the GMR effect. A simple model of the GMR effect in multilayers with the current in the plane of the sample is shown in figure 3.2, with a resistor model for each of the parallel and anti-parallel alignments. In this schematic representation the resistance of the layers to the two possible conduction bands, i.e., parallel and anti-parallel, is shown. The resistance occurs as a result of spin dependent scattering at the interfaces of the alternating ferromagnetic and non-magnetic layers of the multilayer. As electrons

reach the interface of a ferromagnetic layer those with spins anti-parallel to the magnetisation in the layer are predominantly scattered whilst electrons with parallel spin to the magnetisation pass through the interface. In the non-magnetic layer the scattering of the two conduction channels are the same. Ideally in zero field the nonmagnetic layer thickness is such that the magnetisations in successive ferromagnetic layers are anti-parallel, i.e., antiferromagnetically coupled. Thus the two conduction bands are alternately scattered at the interfaces of alternate layers resulting overall in a high resistance state. However, when the multilayer is placed in a magnetic field the magnetisations align, consequently, only one of the spin channels is predominantly scattered at the ferromagnetic/non-magnetic interfaces resulting in a reduction in resistance. The difference in resistance of these two states is illustrated using the resistor model in figure 3.2. The model shows that the overall resistance is higher when the magnetic layers are antiferromagnetically coupled and lower when ferromagnetically coupled. The spin dependent scattering gives rise to a change in resistance far greater that OMR and AMR with values up to 70% in Co/Cu multilayers at room temperature being reported (Parkin, 1995).

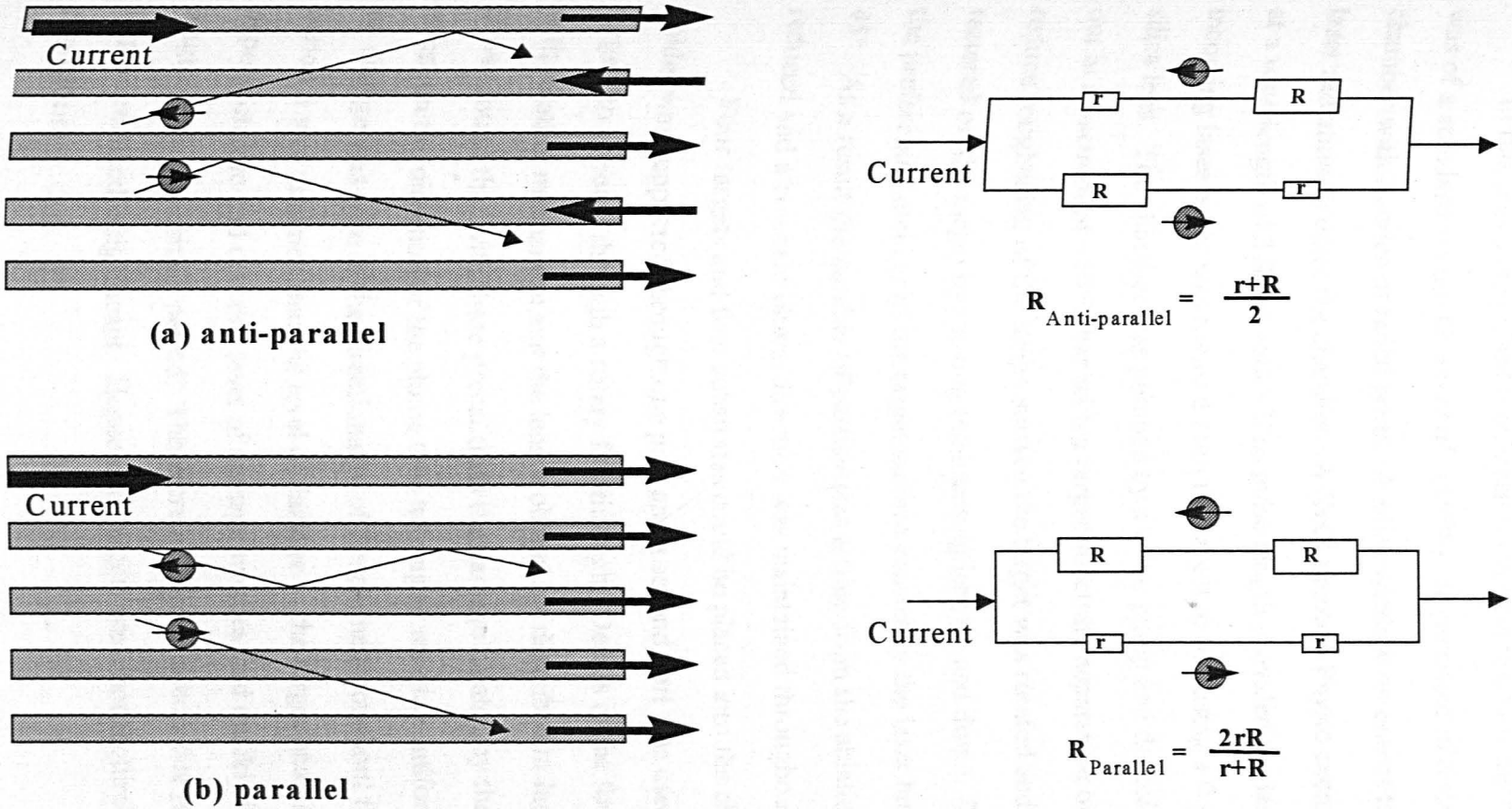

Figure 3.2 A schematic representation of spin dependent scattering at the magnetic/non-magnetic interfaces of a multilayer film. (a) shows both parallel and anti-parallel spin species being scattered for the anti-parallel magnetic alignment. (b) shows the parallel alignment where the electrons with spin anti-parallel to the magnetisation undergoing more scattering than electrons with spin parallel to the magnetisation. Based on a figure provided by E.W. Hill (Private communication).

Chapter 4

4 Experimental Procedures

4.1 The Standard Pulsed Laser Ablation Deposition Chamber

In this thesis the pulsed laser ablation system used for the deposition of films was of a standard set up, Green *et al.*, (1994). It consisted of a stainless steel chamber with a series of radial ports. A silica window on one of the ports allowed laser radiation to enter the chamber. A XeCl Lambda Physic excimer laser operating at a wavelength of 308nm with ~20ns pulse length provided the laser radiation. The incoming laser beam was focused onto the target at 45° using a 0.4m focal length silica lens. The chamber was pumped by a turbo pump and depositions were carried out in a vacuum of $\sim 10^{-6}$mbar with a target-substrate separation of 4cm. In order to reduce roughening of the target surface the target was rotated and the laser spot rastered on the target by moving the focusing lens up and down. This also prevented the preferential etching of the target surface caused by the laser hitting the target at 45°. As a result the number of particulates arising from the ablation process was reduced and a constant plume direction was maintained throughout the deposition.

Four targets and four substrates could be placed into the chamber. The target holder was supported through one port and a second port was used to couple the targets to a motor through a rotary feedthrough. Details of the four way target holder with rotation mechanism and the lens 'wobbler' are described in Jackson *et al.* (1995). It was found that with these precautions the damage created by the laser had little effect on the direction of the plume thus helping to maintain uniform ablation. Since no change was seen in the directionality of the plume throughout the deposition period it was assumed that the level of damage to the target had little effect on the deposition rate and that this level of damage was reached quickly in comparison to the length of the deposition period. Therefore any initial effects due to changes at the target remained insignificant. Hence new targets were not required for each deposition.

The four way substrate holder consisted of four faces of a cube which could be rotated into the ablation plume, one of which was adapted to hold a 5MHz crystal quartz oscillator to determine the deposition rates. The 5MHz driver is detailed in Callegaro *et al.* (1994).

Targets were prepared from pieces of the required metal ~1cm^2 in area. These were polished using p1000 SiC paper. Both the targets and the substrates were cleaned in acetone followed by ethanol. Glass microscope slides were used as substrates for the droplet study discussed in chapter 5 and silicon for the multilayers discussed in chapter 6. This system was used to deposit multilayer samples PyPt2, PyPt3 and PyPt4 in chapter 6 and is based at the University of Warwick.

4.2 Determining Laser Fluences

Fluences, i.e., energy densities on the target, were determined by measuring the pulse energies and the spot sizes produced by the laser beam. For the system described above the laser pulse energy was measured using an energy meter internal to the excimer laser, which had been previously calibrated using a Gentec energy meter. In the case of the Questec laser in the wavelength investigation (section 4.4.1) and the laser used at Exitech (section 4.4.3) the pulse energies were measured directly using a Gentec energy meter. In the case of the ps pulse train and single ps pulse regimes (section 4.4.2) the average power was measured. Provided the repetition rate of the pulses was known the energy associated with each envelope and thus each ps pulse could be determined. However some problems in doing this were experienced. Figures 4.1 and 4.2 show schematic pulse profiles of the ps pulse train the single ps pulse envelopes respectively. They are representative of the pulse envelopes observed on an oscilloscope. In both of these cases there is background radiation associated with the ps pulse envelope. Thus in each case an estimate of the energy associated with each part of the pulse envelope was required in order to determine the fluence of each part. The determination of the different fluences for the ps pulses and the background associated with the envelopes is discussed in section 5.7.1.

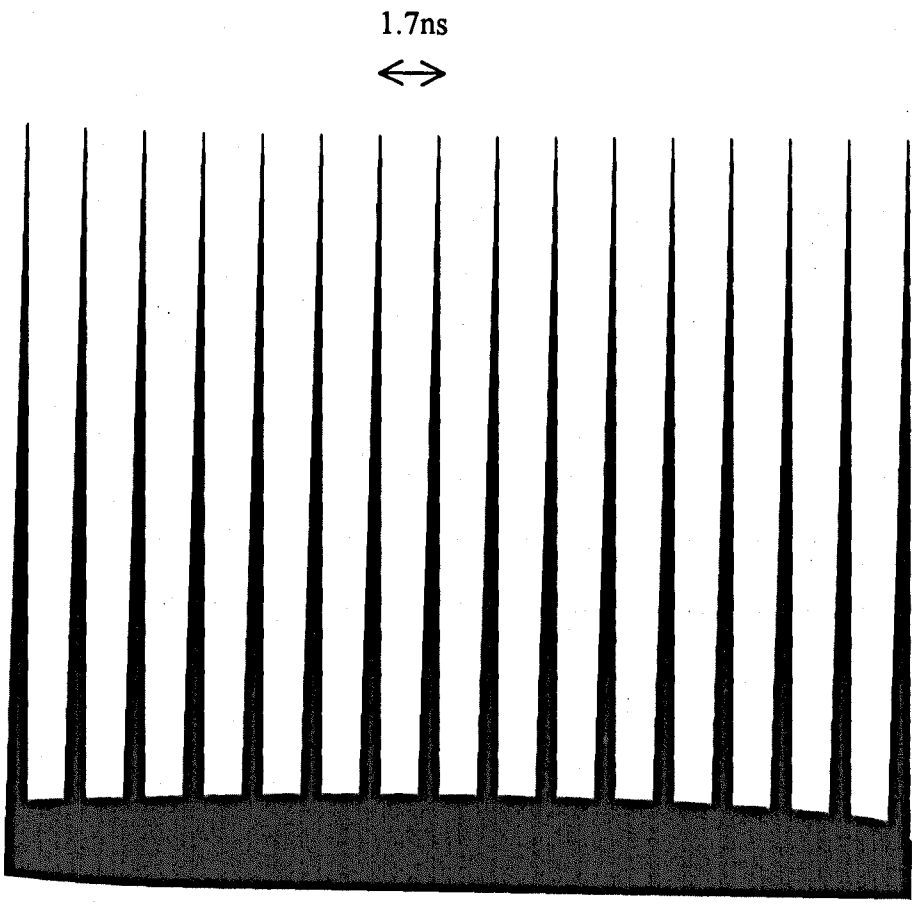

Figure 4.1 A schematic representation of the ps pulse train profile. The individual pulses are 5ps and the background 25ns.

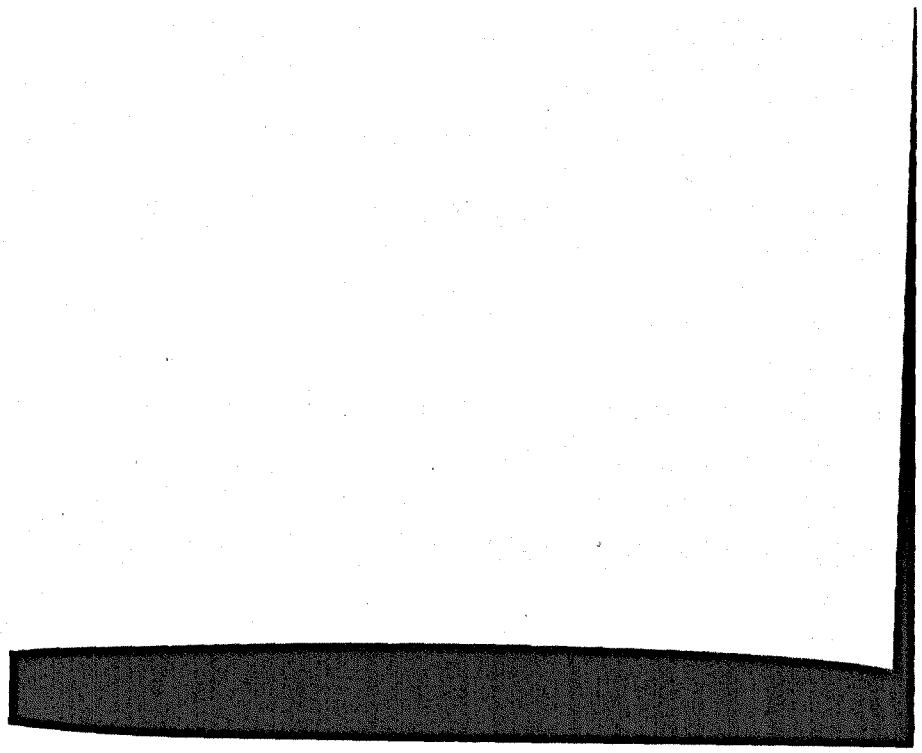

Figure 4.2 A schematic representation of the single 5ps pulse profile.

Throughout the ablation experiments discussed in this thesis the attenuation of the laser beam by the focusing lenses and chamber window was taken into account by measuring the beam energy before and after the lens/window. Typically the total attenuation amounted to 35%.

The spot sizes were taken as the region of visible damage on the target. The size of the damaged region was measured using a scanning electron microscope (SEM). In some cases the spot sizes were confirmed with Talystep stylus measurements of the crater. It must be noted that plasma heating of the target and thermal conduction can increase the area of the visible damage at the target, resulting in lower fluences being reported.

In general, taking the energy associated with the ps pulses and the measured spot sizes, the fluences of the ps pulses were found to be at least two orders of magnitude less than for ns pulse length. Overall the error in the fluence measurements was ±10%.

4.3 Determining Deposition Rates

The rate of deposition of the films being deposited was measured using a quartz crystal oscillator at a range of laser pulse energies. The oscillator control was based on a design given by Callegaro *et al.*, (1994). The film thickness, s (nm), deposited on to the crystal was calculated using

$$s = K\Delta\nu \tag{4.1}$$

where $\Delta\nu$ is the variation in frequency after deposition (Hz) and K is the constant of proportionality in nm Hz^{-1}. K is calculated using

$$K = \frac{1}{10^8 C\rho} \tag{4.2}$$

where C is the crystal quartz constant (Hz cm^2 g^{-1}) and ρ the film material density (g cm^{-3}). C was taken as 0.474×10^{-8} Hz cm^2 g^{-1} (Callegaro *et al.*, 1994). The film thickness deposited in a 10 minute period was used to determine the deposition rate at

a particular fluence. The presence of droplets on the deposited film meant that the deposition rate data could not be used to determine precisely the thickness of films to be grown. Generally, however, film thickness could be measured with the crystal to within 10% and this was confirmed from measuring the thickness of films using a Talystep instrument. Deposition rates up to 0.2nm/s were obtained.

4.4 Variations to the Pulsed Laser Ablation System

Variations to the PLAD and laser systems used in this thesis are outlined in the following sub-sections. The results in chapter 5 discuss the effect of laser wavelength, the temporal profile of the laser pulse, the use of a tape target and a homogenous beam profile on the production of droplets in the PLAD process and on deposition rates. In order to carry out these investigations facilities in the Laser Plasma X-ray Laboratory at the Rutherford Appleton Laboratory (RAL) and at Exitech, a company for advanced laser research and development were utilised. The facilities used at RAL are described in sections 4.4.1., 4.4.2 and 4.4.4 and the equipment used at Exitech is described in section 4.4.3.

4.4.1 Laser wavelength investigation

The system described in this section was used in determining the effects of the laser wavelength on the deposition rates of silver and nickel in section 5.3 and on the number of droplet produced during deposition in section 5.6.1. The system was based at the Rutherford Appleton Laboratory.

A Questec 2440 laser provided the ns pulse source. Gas mixtures ArF, KrF and XeF were used to give wavelengths of 193nm, 248nm and 351nm respectively. This laser was operated at a repetition rate of 20Hz with a pulse length of 20ns. The laser was operated at fixed energy, ~200mJ. This energy was higher than required for the ablation experiment thus a series of quartz and glass plates were used to attenuate the beam. Once attenuated, the energy per pulse was measured at ~100mJ giving a typical peak power of 5×10^6W. The beam was focused using a 0.4m focal length lens. The position of the lens needed to be adjusted at each wavelength to find the exact focus, see section 4.4.3.1. By obtaining the optimum focus, i.e., smallest spot

size, variations in the deposition rate arising for different spot sizes are minimised. The optimum focus was taken as the position giving the largest plume. Once focused, fluences ranging up to $20J/cm^2$ were available. It was found that the spot size at 248nm was larger than those measured for 193nm and 351nm, this was attributed to the fact that the brightness of the plume did not vary over a 1cm range of the lens-target distance, thus making it difficult to obtain the exact focus. The spot sizes at 193nm and 351nm were similar, so droplet densities obtained from films deposited at these two wavelengths were compared in the wavelength investigation.

The investigation was carried out using the PLAD chamber and conditions described in section 4.1. Nickel and silver targets were used and the deposition rates for these metals were determined using the quartz crystal oscillator. The results of deposition rates measured by this method are discussed in section 5.3 and 5.7.2. A series of nickel and silver films were deposited over a range of fluences on to glass substrates. Deposition times were from 5 minutes up to 1 hour. For each ablation run the beam energy was measured before and after the films were grown to monitor variations. Typically the final beam energy was 85% of the initial value. The uniformity of the films was of utmost importance both from the point of view of good experimental analysis and for the ultimate goal of producing multilayer devices. Film uniformity was monitored by masking over one of the substrates in the chamber with a 12μm thick copper grid. Thus subsequent to the deposition process, the thickness uniformity across the films was checked using a Talystep stylus instrument. The thicknesses of these films were found to have a tolerance of 5nm in 50nm. For the remaining films thickness was measured at four points around the film edge.

To estimate the droplet density and area, digital SEM images of the centres of the films were taken and analysed using an image processing package. From a series of five digital images the number of droplets on the films was calculated, the results are presented in section 5.3.1.

In the wavelength study presented in chapter 5, films deposited at similar energy fluence and where possible similar thickness are compared. Where similar thicknesses were not possible, the droplet densities were scaled accordingly.

4.4.2 The laser pulse temporal profile investigation

The temporal profiles described in this section were used in conjunction with the standard PLAD system described in section 4.1 to obtain the results presented in sections 5.7 and 5.8. Experiments using this system were performed at the Rutherford Appleton Laboratory.

The effects of the temporal profile of the laser pulse on the pulsed laser ablation deposition of metallic films was studied. ,Nickel and silver films deposited on to glass substrates using ps pulse train, single ps pulse and 20ns pulse profiles at a wavelength of 248nm were compared. The ps pulse train profile consisted of a 20ns pulse envelope operating at a repetition rate of 20Hz which contained sixteen, 5ps pulses. It was produced using an oscillator/amplifier system consisting of a sync pumped dye laser pumped by a mode locked YAG to provide pulses at 748nnm. By splitting the beam appropriately sixteen 5ps pulses were obtained forming the pulse envelope. The envelope was then amplified and converted to 248nm. Further details of the system are given in Turcu *et al.* (1994). To obtain a single ps pulse all except one beam arising from the beam splitting required for the production of the ps pulse train were blocked. The remaining pulse was amplified and converted to 248nm as for the ps pulse train. The Questec laser described in section 4.4.1 was used to give ns pulses at a repetition rate of 20Hz for this investigation.

The ps laser operated at ~0.3J/envelope. These energies were higher than required for the ablation experiment hence the beam energy was attenuated as for that of the ns pulses, section 4.4.1, using a series of glass and quartz plates. Once attenuated the peak power for a ps pulse was ~10^{12}W, with the ns envelope taken into account and 10^{9}W for the ns pulses.

The deposition of films using the ps pulse train, single ps pulses and ns pulses were carried out in the same way as described for the wavelength study, section 4.4.2,

with the results being discussed in section 5.7. For the purpose of the temporal profile investigation the focus was not altered between the series of films deposited to compare ns pulse and ps pulse train profiles deposition and between the films deposited by the ns and single ps pulse profiles.

The problems associated with ascribing fluences to the films deposited using ps pulses, see section 5.7.1, meant that films of similar thickness to those deposited using ns pulses were used to compare droplet numbers.

4.4.3 Homogenous laser beam investigation

The system described in this section was used to investigate the effects of a homogeneous energy profile on the deposition of gold films. It incorporates the standard PLAD system described in section 4.1 with a different laser and imaging optics. Experiments using this system were performed at Exitech and are presented in section 5.9.

An excimer laser operating at 308nm with a pulse length of 20ns and repetition rate of 20 Hz was used in this investigation. The size of the beam profile was large, i.e. ~10cm^2, compared to the lasers used in the previous two investigations, ~1cm^2. This meant that the beam was substantially apertured to obtain a suitable beam profile and pulse energy to be incident upon the imaging optics. The initial pulse energy of the beam was >500mJ. After the aperture the pulse energy was measured as ~20mJ. The profile was measures using a ccd camera and imaged using software provided by Exitech. Figure 4.3 shows that the energy density profile of the apertured beam was uniform. To achieve a non-uniform beam two cross hairs of around 30μm were placed at the aperture. This was imaged by the optics onto the target at ~1μm. The non-uniform beam profile is shown in figure 4.4.

4.4.3.1 The imaging optics

In this investigation the beam at an aperture was imaged on to the target, rather than focused as with the other studies. Simple optics show that the focal length of the lens l, image distance v and object distance u are related by equation 4.3.

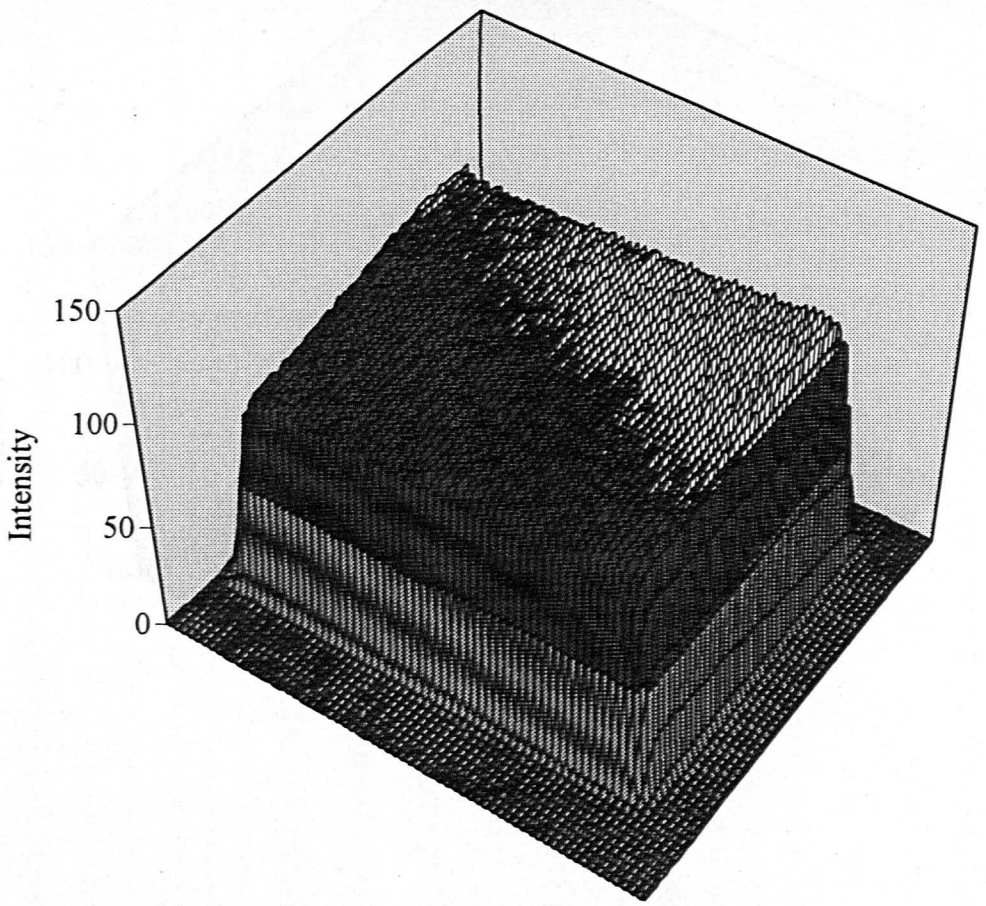

Figure 4.3 Intensity of uniform beam profile

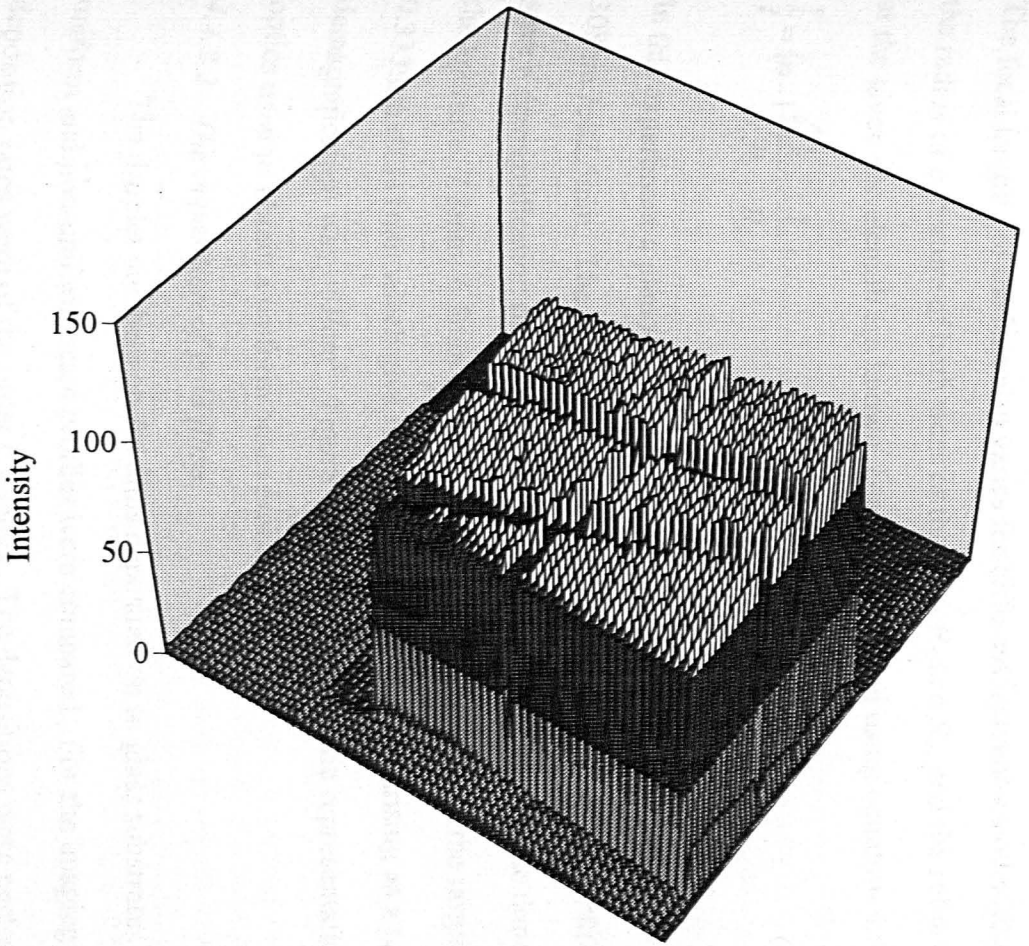

Figure 4.4 Intensity of non-uniform beam profile

$$\frac{1}{l}=\frac{1}{u}+\frac{1}{v} \qquad (4.3)$$

These parameters can be chosen to give a demagnification of the aperture resulting in a sufficiently high energy density on the target for ablation. The demagnification M is given by

$$M=\frac{u}{v} \qquad (4.4)$$

The focal length l of the lens also varies for different incident wavelengths. Provided the radius of curvature of both sides of the lens, R_1 and R_2, and the refractive index, n, at the given wavelength are known, l can be calculated using equation 4.5.

$$\frac{1}{l}=(n-1)\left(\frac{1}{R_1}-\frac{1}{R_2}\right) \qquad (4.5)$$

In this experiment a plano-convex lens was used, which meant that $R_2=\infty$ and at 308nm l=82.5mm. The lens was placed such that u=1984.5mm and v=86.1mm which gave a demagnification of 23. This was confirmed by comparing the dimensions of the aperture, 7.8mm×6.5mm with the dimensions of the spot on the target, 0.333mm×0.311mm which give ratios of ~23. The fluence arising as a result of the demagnification was ~5J/cm^2. Figure 4.5 shows a schematic representation of the optics used to obtain a uniform beam profile.

4.4.3.2 The deposition of gold films

The droplet numbers on Au films deposited on to glass substrates using the uniform and non-uniform beam profiles were compared. For the imaging optics the deposition rates were of the order 0.05nm/s. The depositions were performed in the chamber described in section 4.1 with a fluence of the order 5J/cm^2 and a repetition rate of 20Hz. The spot sizes were determined as for the spots produced using a focused beam and film thicknesses were measured with a Talystep instrument.

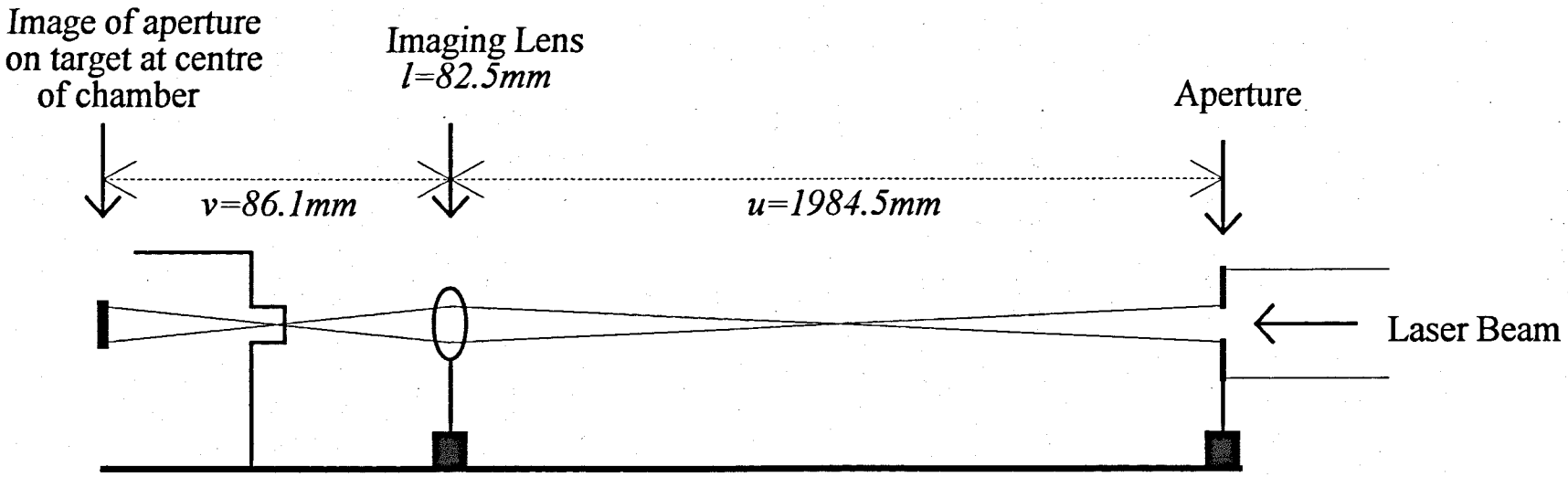

Figure 4.5 A schematic representation of the homogenising optics used for depositing gold films at Exitech.

4.4.4 The use of a tape target in PLAD

The system described below was used to deposit copper films using a spooled tape target and the ps pulse train profile described in section 4.4.2. The experiments were performed at the Rutherford Appleton Laboratory and are discussed in section 5.10.

The tape target was spooled at ~0.02m/s. The ps pulse train punched a hole through the 25μm Cu tape and some material was ejected behind the tape. Scanning electron micrographs of the samples were taken to measure the droplet density on the films.

The chamber was a large chamber situated in the Laser Plasma X-ray Laboratory at RAL. The system used was basically as for the production of x-rays by Turcu *et al.* (1991) with a few variations, see figure 4.6. The chamber was evacuated using a turbo pump to 10^{-5}mbar, as opposed to the usual operation in an atmosphere of Ar. The substrate/quartz crystal holder described in section 4.3 was placed into the chamber so that deposition rates could be determined. Typical deposition rates were 0.05nm/s. The target-substrate distance was 6cm, slightly larger than for previous deposition experiments. The details of the laser parameters and pulse production are as for those in the pulse length investigation in section 4.4.2.

4.5 Details of the Deposition of Metallic Multilayers

Multilayers of platinum and permalloy (Py), a nickel-iron alloy ($Ni_{0.8}Fe_{0.2}$), were deposited by two different pulsed laser ablation deposition systems and by sputtering. Details of the deposition techniques are given below. These multilayers were then analysed by cross sectional TEM and x-ray reflectivity to characterise the multilayer deposition. In addition the magnetoresistance of the multilayer samples was measured using a dc, four point probe method. Magnetisation curves are also presented for selected samples to confirm whether or not they are ferromagnetic.

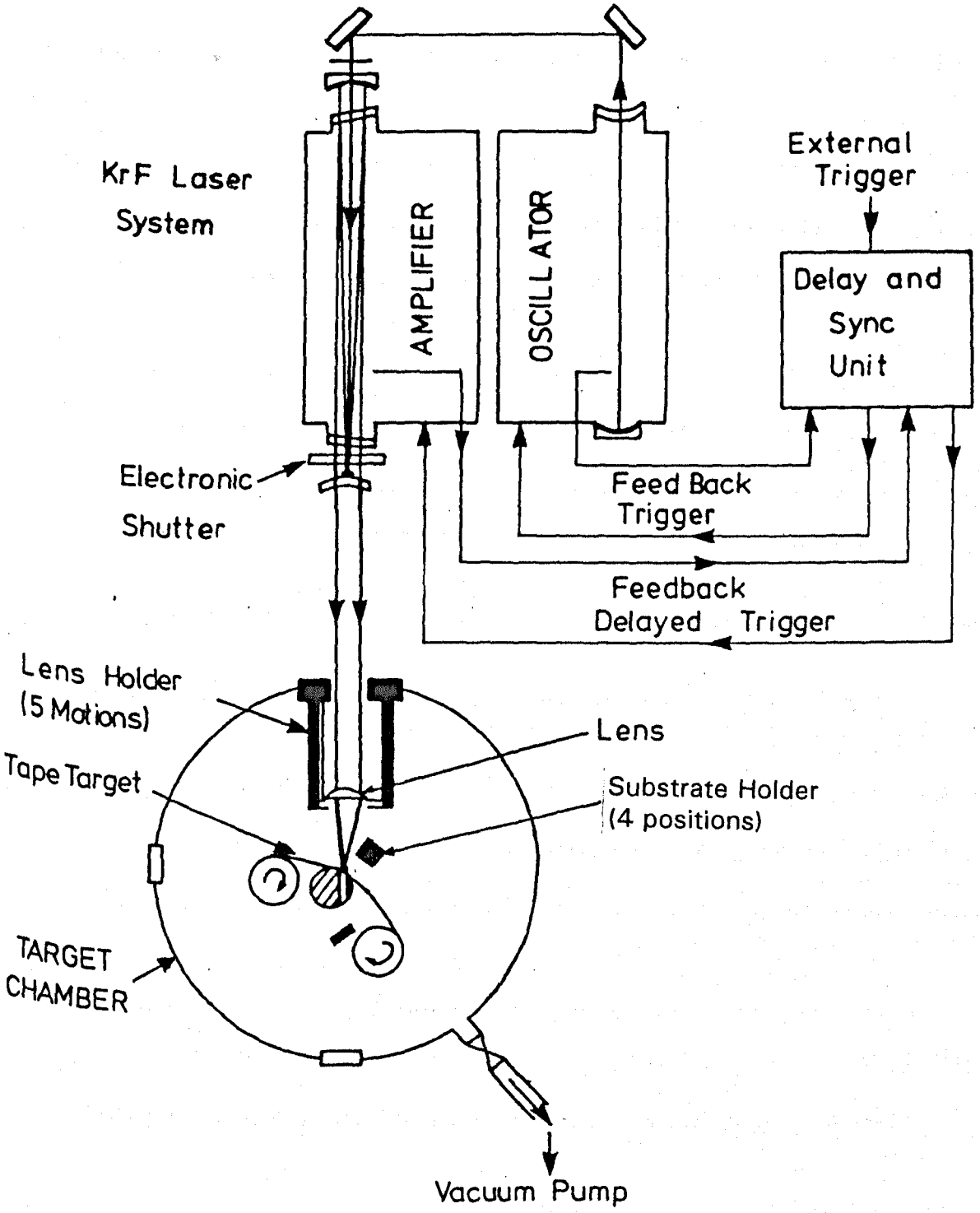

Figure 4.6 A schematic representation of the tape target and ps pulse train deposition system at the Rutherford Appleton Laboratory. (Turcu et al., 1991)

4.5.1 Pulsed laser ablation deposition of multilayer samples at the University of Warwick

The deposition conditions and target preparation used to deposit the multilayers were as for the standard PLAD chamber described in section 4.1. The Py target was prepared by pressing the powder into a pellet using a load of 20ton on a 1½ inch die followed by sintering at 1200°C for 1 hour. Three silicon substrates and a quartz crystal oscillator were placed in the substrate holder. Two each of Pt and Py targets were placed on the target holder. At a fluence of 3-4J/cm^2 and repetition rate of 30Hz, deposition rates of Pt and Py were measured as ~0.05nm/s and ~0.07nm/s respectively. From the measured deposition rates a known thickness of each layer could be deposited. Samples PyPt2, PyPt3 and PyPt4 are deposited by this method their layer thicknesses are shown in Table 6.1. The deposition rates did vary during the deposition of the multilayer samples. Thus they were determined at intervals throughout the deposition process, and the times for layer deposition were adjusted accordingly.

4.5.2 Pulsed laser ablation deposition at the Moscow Engineering Physics Institute

The pulsed laser evaporation deposition equipment described here is situated at The Moscow Engineering Physics Institute, Department of Solid State Physics. The differences between this system and that described in the previous section are that fluences close to threshold are used in the Russian system. Thus, in addition to ablation, the lower fluences give rise to a substantial amount of evaporation. The deposition was carried out using a Nd-YAG laser at a wavelength of 1064nm and pulse length of 15ns. At a repetition rate around 30Hz and fluence of ~3J/cm^2 the deposition rates were of the order of 0.03nm/s. The base pressure of the chamber was 4×10^{-9}mbar. The system was fully automated with the lens position being adjusted to achieve the threshold fluence for each individual target material. The structure of the Py/Pt multilayer sample m6 deposited on to silicon substrates is summarised in Table 6.1.

4.5.3 RF magnetron sputtering

These samples were prepared at the Centre for Data Storage Materials at the University of Coventry. The samples were prepared by RF magnetron sputtering in a Nordiko 2000 system. The base pressure was ~1.3×10^{-7}mbar and the sputtering pressure ~4×10^{-3}mbar. The power used to sputter the targets ranged from 80-250W. and deposition rates of the order 0.1nm/s were achieved. Py/Pt multilayers with tantalum buffer layers were deposited at room temperature on to microscope slides. Both the targets and substrates were sputter cleaned in situ before deposition was carried out. In order to deposit Ni-Fe alloy mosaic targets were used. The structures of the multilayers are summarised in Table 6.1. The samples deposited by this method are nm23 and nm25.

4.6 Cross Sectional Transmission Electron Microscopy of Multilayer Samples

Cross sectional specimens of the multilayer samples were prepared in order to compare the uniformity of the multilayers deposited by the different deposition methods and to support the x-ray reflectivity data collected.

4.6.1 Preparation of samples

To prepare cross sectional samples for TEM, two strips ~2mm wide of each multilayer sample were cut using a diamond scribe. These strips were stuck film side together using standard Araldite which was gently heated to remove bubbles. The double strips were then set using warmed Araldite in a brass tube with a total diameter of 3mm, this was the size of the specimens required for the TEM specimen holder. Disks were cut from the tube using a diamond saw. These disks were mechanically polished/thinned and dimpled to a thickness of ~50μm. The final thinning stage was carried out by argon ion beam thinning at a low angle of 15° and an ion energy of 5-6keV. Problems were experienced during the ion beam thinning of the sputtered samples deposited on to glass substrates, i.e., sample nm23 and nm25. Thus thin sections to view in the TEM were limited in these samples.

4.6.2 Imaging of the multilayer samples using TEM

The layers of the cross sectional samples were imaged on a 2000FX JEOL 200kV transmission electron microscope. In order to image the layers very low illumination intensities were required at a magnification of 250kX. The maximum magnification of the microscope is 800kX giving a resolution of the order 0.3nm. At the high magnification and low illumination the imaging was difficult and very sensitive to appropriate imaging conditions. Calibration of the microscope at the magnification of 250kX showed that the scale markers were 15% too long. This meant that samples appeared smaller than they really were. The multilayers appeared as a series of light and dark layers. The contrast arises because higher density materials scatter more strongly and thus appear darker in the image. In this case Pt has a higher density, 21.450g/cm^3, than Py, which, based on the $Ni_{0.8}Fe_{0.2}$ ratio, has a density of the order 8.7g/cm^3 (Kaye and Laby, 1986). Thus Pt appears darker in the micrographs presented in section 6.3.2.

4.7 X-ray Reflectivity of Multilayer Samples

X-ray reflectivity of the multilayer samples were measured by performing a θ-2θ scan at low angles on a Philips high resolution diffractometer. The small x-ray wavelength makes it useful for studying atomic dimensions and their penetration allows sub-surface regions to be analysed. The scans were performed for θ=0-2°. Modelling is required for detailed analysis of multilayer structures, including the amount of diffusion between layers and the roughness and variation of thickness of the layers. However for the purposes of this investigation the important features of the x-ray reflectivity curves can be used to determine the repeat layer thickness and give an indication of the roughness.

The curves obtained in this thesis show strong Bragg peak reflections and smaller peaks between the Bragg peaks. The intensities and widths of the Bragg peaks and smaller peaks give important information concerning the multilayer structure.

The position of the Bragg peak, θ, can be used to determine the bilayer thickness, d, of the multilayer sample from the Bragg condition.

$$d = \frac{m\lambda}{2\sin\theta} \qquad (4.6)$$

where m is the m-th order Bragg peak and λ the x-ray wavelength. In this case the source was $CuK\alpha_1$ with λ=0.1541nm The total layer thickness can be determined from the subsidiary peak separation by using the angular separation in the Bragg condition equation 4.6. The precision of the diffractometer was 0.01°, however broadening due to roughness increased the error in determining peak positions.

Roughness in the sample results in the intensities and shapes of the Bragg and subsidiary peaks being altered and can arise from two sources. Roughness that is propagated from layer to layer, usually arising from an imperfection at the substrate, is known as correlated roughness. Local diffusion and roughness at layer interfaces and variations in layer thickness generally gives uncorrelated roughness. Uncorrelated roughness results in the decrease in intensity of the Bragg peaks whilst the correlated roughness broadens the Bragg peaks. The subsidiary peaks are also affected by roughness in the multilayers, one of the major features being the smearing of the oscillatory behaviour. Modelling of x-ray reflectivity data allows these features to be quantified and can give detailed information about the diffusion and roughness in the multilayer sample (Kim *et al.*, 1996). In the data shown in chapter 6 the reduction in intensities of the data at higher angles and the broadening of the peaks are compared to allow a qualitative conclusion of the varying amount of roughness and diffusion between samples.

4.8 Magnetoresistance Measurements of Multilayer Samples

A standard four point probe method was used to measure the magnetoresistance of the multilayer samples. The probes were spring loaded points mounted in a line. A constant current of 2mA was maintained in the films through the

outer most probes. This was provided by a Thurlby PL320 power supply connected across a 32Ω resistor, in series with the sample. Provided the resistance of the sample was less than 32Ω the current remained constant. Typically the sample resistance was of the order of 10Ω. The potential across the inner two probes was measured using a nano-voltmeter. The change in the potential across the sample was measured as a function of applied magnetic field. Typically the change in voltage was a few mV. Thus the change in resistance of the sample with magnetic field was calculated from the potential drop and constant current.

The applied magnetic field was supplied by an electromagnet. Between the pole pieces a maximum field of up to 0.88kA/m ($\mu_0 H$=1.1T) was possible with good field uniformity across the sample space. The field was measured using a hall probe placed at the pole pieces, and close to the position of the sample.

The sample holder was restricted by the gap between the pole pieces. Thus the samples were 8mm×3mm. The sample was placed between the pole pieces such that the applied magnetic field was in the plane of the film. The sample could be rotated within the applied magnetic field to obtain measurements with the current parallel or perpendicular to the magnetic field. These measurements were used to ascertain whether the magnetoresistance was isotropic or not.

The field cycle for measurement of the MR was as follows. The magnetic field was set at a maximum applied field strength. Once this was obtained the potential across the sample was measured. The magnetic field was then set to zero and the potential measured again. This gave an idea of the overall change in the MR thus allowing an absolute value of the change to be determined straight away. The field was then returned to maximum and swept through zero into the reverse direction and back to the initial field setting. The potential of the sample was measured during the sweeping of the magnetic field. The step sizes for the field were less in the region near to zero magnetic field. In the case of anisotropic magnetoresistance the rate of change in resistivity greatly increases at low field. Thus smaller steps enabled the change in resistance at low magnetic field to be more precisely recorded. The cycling

of the magnetic field described above meant that virgin curves for MR measurement were not obtained.

4.9 Magnetisation Curves of Warwick Multilayer Samples

The magnetoresistance results presented in section 6.4 suggest that samples PyPt2, PyPt3 and PyPt4 are not ferromagnetic, thus the magnetisation curves were measured to establish whether or not they were.

An Oxford Instruments MagLab vibrating sample magnetometer (vsm) was used to measure the magnetisation curves of these samples. The samples were measured in five quadrants, starting at zero field and rising to an applied field of 0.80A/m ($\mu_0 H$=1T), sweeping through zero to –0.80A/m and back to 0.8A/m.

The raw magnetisation curves had to be corrected to take out the diamagnetic response of the silicon substrates. The diamagnetic response due to the platinum in the samples was found to be negligible since the mass of platinum was 2.2×10^{-5}% of the mass of the silicon. The diamagnetic response of silicon was measured using the vsm and subtracted from the raw magnetisation curves. In addition the diamagnetic response for the silicon substrates was calculated from the diamagnetic magnetisation per atom, Δm_0, given by

$$\Delta m_0 = -\frac{\mu_0 e^2 r^2 HZ}{6m_e} \qquad (4.7)$$

where r is the atomic radius, Z the outer electrons of the atom (4 for silicon) and m_e the mass of the electron. From the mass of the sample the value for the diamagnetic response of the multilayer samples was determined. Both of these correction methods are discussed in section 6.5.

Chapter 5

5 An Investigation into the Effects of Pulsed Laser Ablation Deposition Parameters on the Deposition of Metallic Films

5.1 Introduction

In this chapter the effects of changing four parameters of the PLAD technique on the deposition of metallic films are presented. In particular we see how these parameters affect the deposition rates of the films and the density of droplets deposited on them. Equations 2.1 and 2.2 show that the removal of material from the target by PLAD is dependent upon the laser pulse length and laser wavelength through the thermal diffusion length and optical absorption depth respectively. Therefore the effects that changing the laser wavelength and temporal profile of the laser pulse have on the deposition rates and production of droplets are investigated. In addition the use of a tape target and a uniform energy beam profile on the production of droplets are also investigated. The results presented elucidate some aspects of the laser-target interaction mechanisms that take place during ablation. These might be exploited for the control of deposition rates and the reduction in droplet formation.

5.2 The Effects of Laser Fluence and Film Thickness on the Deposition Rate Characteristics of Nickel and Silver

The results presented in this section were obtained from experiments performed at the Rutherford Appleton Laboratory using the PLAD system described in section 4.4.1.

The deposition rates in this section are quoted in units of nm/pulse/cm^2. Whilst the nm/pulse is measured at the substrate as a deposition rate, this value is scaled with the ablation spot seen on the target to allow some comparison between ablation experiments with different spot sizes. However it must be noted that

different spot sizes give rise to different plume expansion and therefore it is not necessarily valid to assume that the deposition rate varies linearly with the area of the spot size. The errors in the fluences and deposition rates are ±10%, however for clarity the errors bars are left out of some deposition rate figures.

The data presented here highlight different deposition characteristics for nickel and silver. For silver, figures 5.1 and 5.2, we see that at higher fluences the deposition rates tend to tale off or reduce in magnitude, thus showing saturation. Similar behaviour is seen for nickel in figure 5.3 at fluences above 9J/cm^2. In figure 5.4, however, saturation of the deposition rates at 193nm, 248nm and 351nm is not observed. The data at 248nm do not contradict the results shown in figure 5.3 because the fluences do not exceed 9J/cm^2, thus a tendency towards saturation is not observed.

In section 2.4.1 self sputtering is suggested as the origin of the saturation characteristics of the deposition rates. The deposition rate data in figures 5.1, 5.2 and 5.3 suggest that a portion of incoming ions are energetic enough for self sputtering to occur at fluences >5J/cm^2 in silver and >9J/cm^2 in nickel. This is in agreement with the sputtering yield expressions, figure 2.2, which show that silver is more easily removed by either incoming nickel or silver ions. The data also suggests that the thickness of films already present on the quartz monitor can affect the deposition rate of incoming material. This is in accordance with the self sputtering phenomenon which points to the importance of the order in which deposition rate data are determined as to what value is obtained. For example, if a film of silver is present on the quartz crystal at the start of a silver deposition then the deposition rate of silver is found to be different to the case where a film of nickel is initially present on the substrate. Thus the order of in which deposition rates are determined influences the results. To test the theory of self sputtering, as the origin of the saturation characteristics observed, further details of the deposition procedures are outlined below. Where deposition rate series are not discussed directly in the text details of the deposition measurements are given in appendix A for further reference.

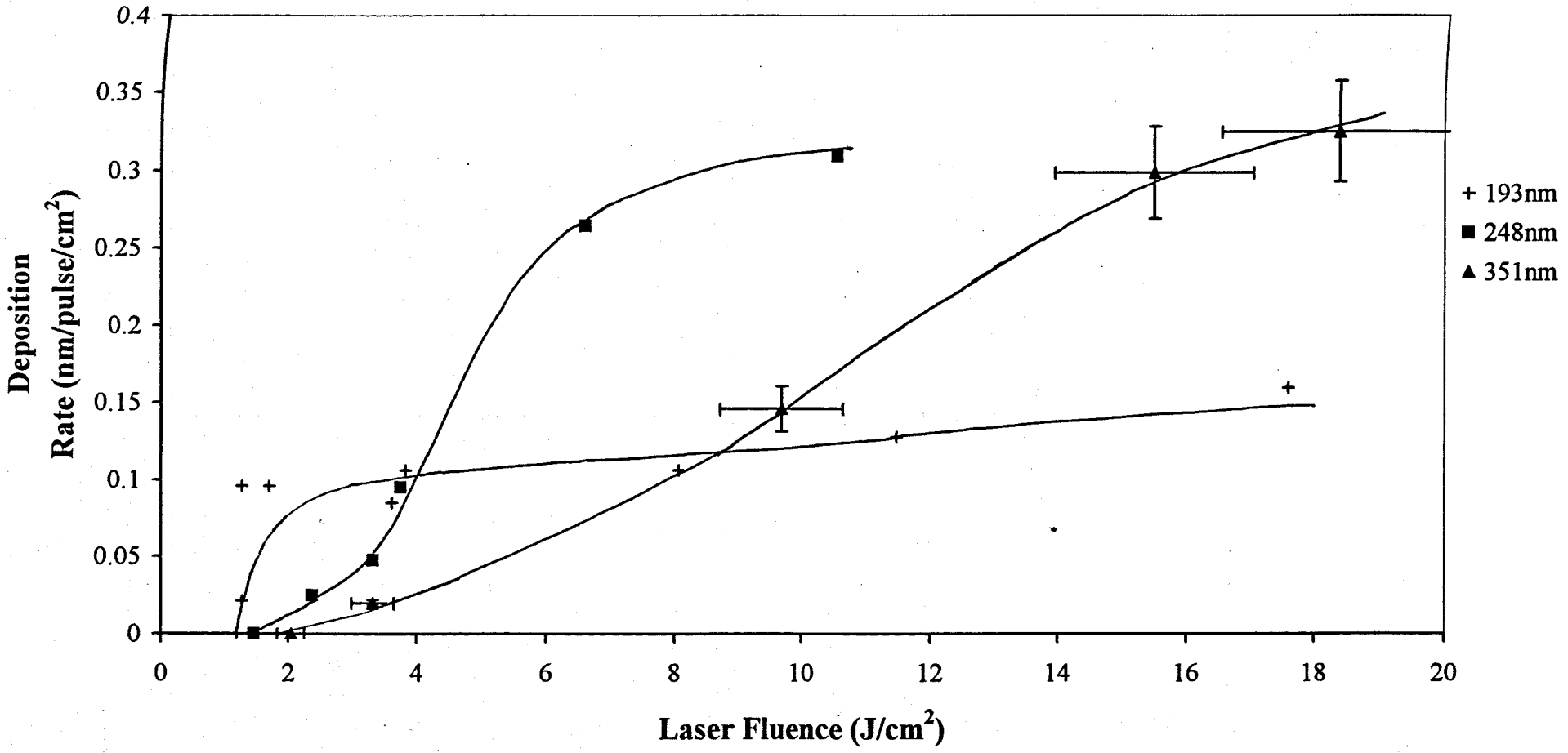

Figure 5.1 A series of deposition rates determined for silver using laser wavelengths 193, 248 and 351nm. Laser pulse length is 20ns. For clarity error bars are shown for 351nm only.

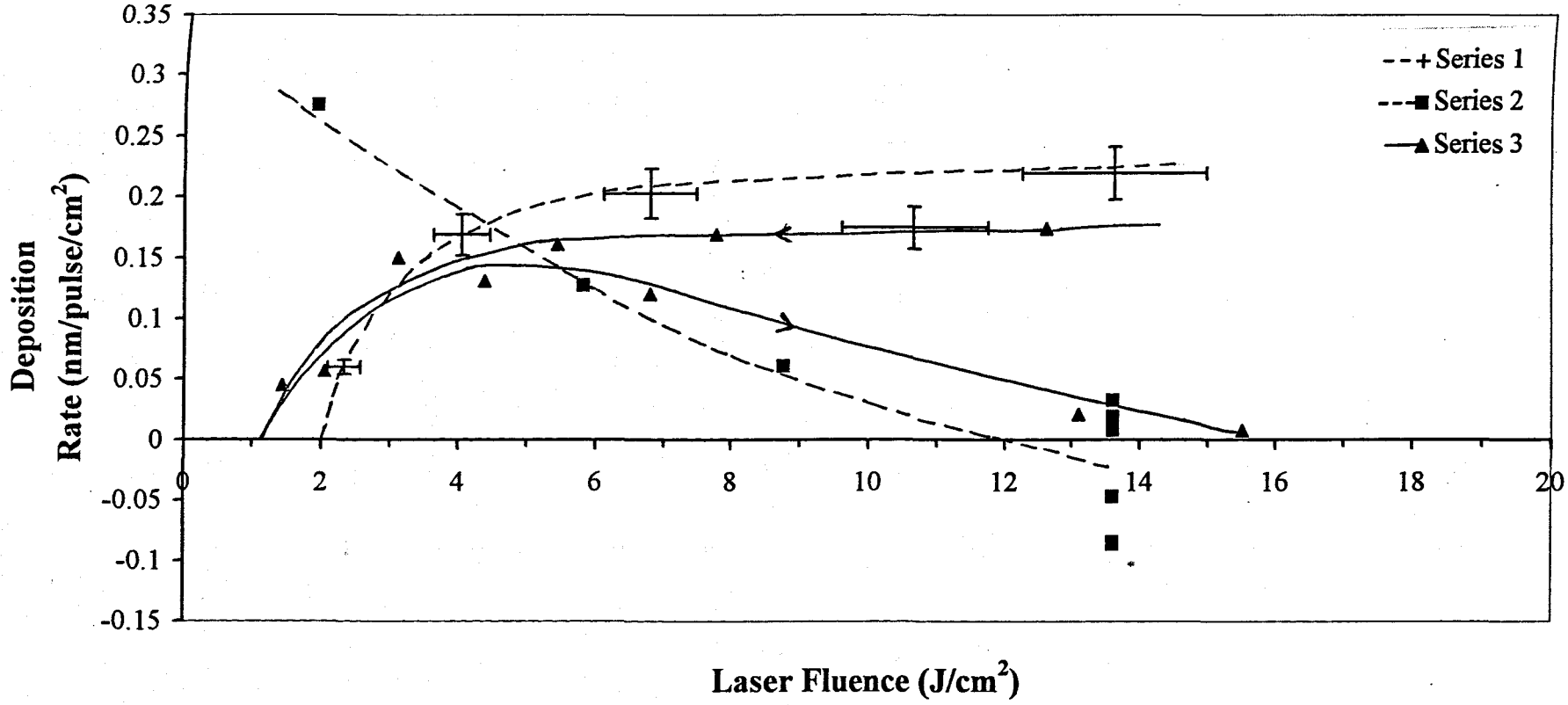

Figure 5.2 A series of deposition rates determined for silver using 248nm laser radiation, 20ns pulse length. Sputtering of the films is evident from the low deposition rates at high fluences. For clarity error bars shown for one series only.

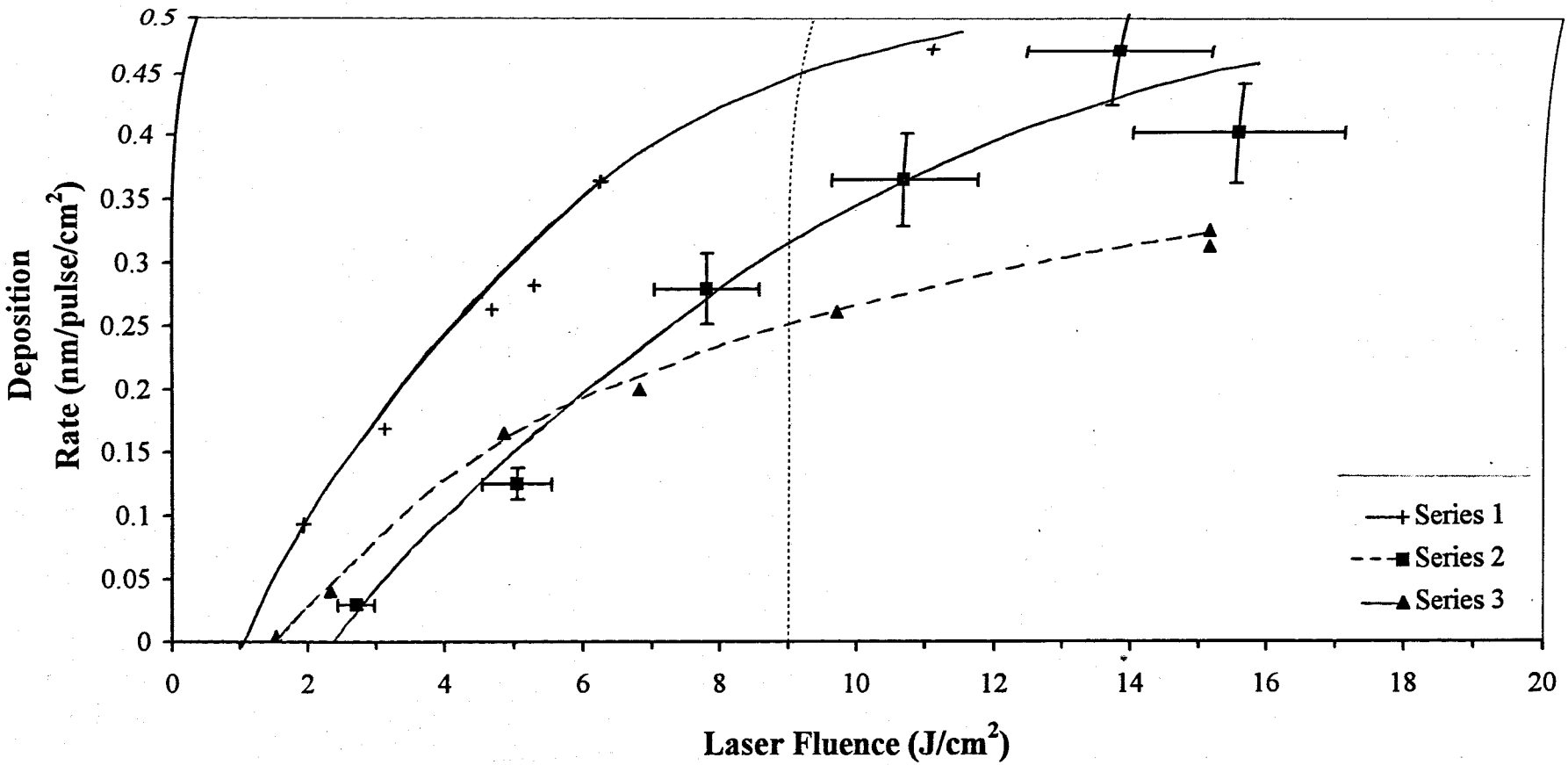

Figure 5.3 Deposition rates of nickel using 248nm laser radiation, 20ns pulse length. The vertical line at 9J/cm^2 indicates the maximum fluence in figure 5.4. Below this value saturation in the deposition rate is not evident.

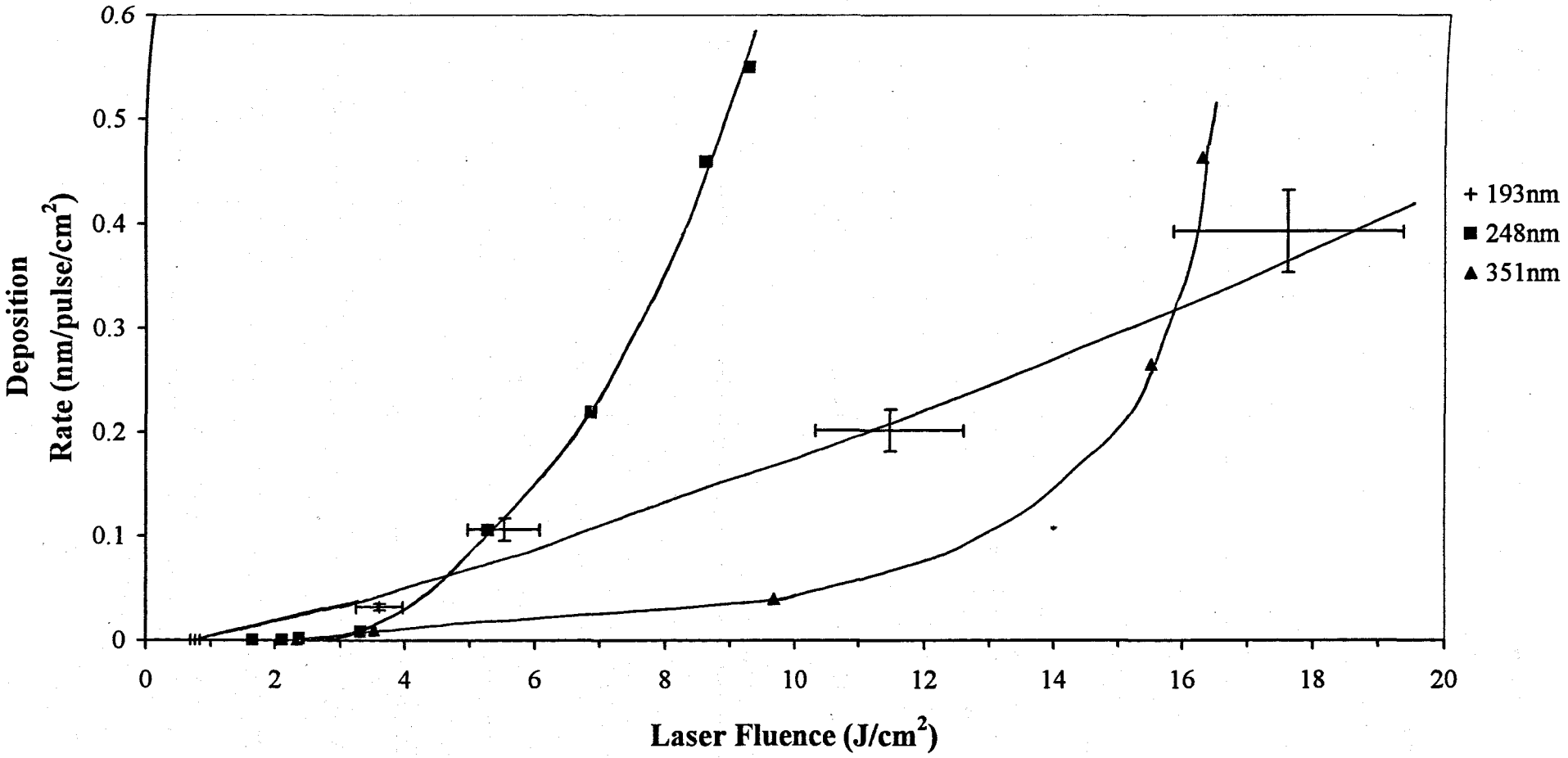

Figure 5.4 A series of deposition rates determined for nickel using laser wavelengths 193, 248 and 351nm. Laser pulse length is 20ns. For clarity error bars are only shown for 193nm series.

Order	Fluence (J/cm^2)	Deposition rates $nm/pulse/cm^2$	Thickness Deposited (nm)	Accumulated Thickness On Quartz Monitor (nm)
Series 1				New Crystal
1	14	0.54	54	54 (Ag)
2	14	0.22	22	76 (Ag)
3	4.1	0.17	17	93 (Ag)
4	11	0.17	17	110 (Ag)
5	6.8	0.20	20	130 (Ag)
6	2.3	0.060	6.0	136 (Ag)
Series 2				136 (Ag)
1	14	-0.086	-8.5	127.5 (Ag)
2	14	-0.085	-8.4	119.1 (Ag)
3	14	-0.047	-2.8	116.3 (Ag)
4	8.8	0.061	6	122.3 (Ag)
5	5.8	0.13	12	134.3 (Ag)
6	1.9	0.28	27	161.3 (Ag)
7	14	0.007	0.7	162.0 (Ag)
Series 3				100.0 (Ni)
1	13	0.17	18	18 (Ag)
2	7.8	0.17	17	35 (Ag)
3	5.5	0.17	16	51 (Ag)
4	3.1	0.15	15	66 (Ag)
5	2.1	0.058	5.7	71.7 (Ag)
6	1.4	0.045	4.4	76.1 (Ag)
7	4.4	0.13	13	89.1 (Ag)
8	6.8	0.12	12	101.1 (Ag)
9	13	0.021	2.5	105.6 (Ag)
10	16	0.008	2.1	105.7 (Ag)

Table 5.1 The silver deposition measurements of *series 1, 2, and 3* shown in figure 5.2. λ=248nm.

The first indication that sputtering of the depositing film occurred was the low/negative deposition rate seen in the silver deposition at high fluence, shown in Table 5.1 by measurements 1, 2 and 3 of *series 2*, which pointed to material being removed from the crystal. For example deposition 1 was carried out on to 136nm of silver at a fluence of 13.6J/cm^2 giving a deposition rate of –0.086nm/pulse/cm^2.

In contrast silver layers deposited onto nickel layers had higher deposition rates. For example deposition 1 of *series 1* in Table 5.1 gives a higher deposition rate of 0.54nm/pulse/cm^2 at the same fluence as the conditions described previously. This difference is also highlighted when silver and nickel depositions are alternated. For example a silver deposition rate of 0.007nm/pulse/cm^2 was measured when depositing on to 162nm of silver at a fluence of 11J/cm^2. Whereas a higher deposition rate of 0.032nm/pulse/cm^2 was measured for silver deposited on to 37nm of nickel at the same fluence. This was followed by a decrease in the deposition rate of silver to 0.015nm/pulse/cm^2 as the silver film thickness increased. Thus the behaviour was consistent with the deposition rate being dependent upon whether a silver or nickel layer had previously been deposited on to the crystal. This is shown in figure 5.5, where the deposition rates of silver films onto different accumulative thickness of silver are plotted for fluences >5J/cm^2, from the data in Tables 5.1 and 5.2. 5J/cm^2 was chosen as the cut off for high fluence because this is the point at which the saturation of silver becomes evident. The figure indicates that where silver was deposited at high fluences on to ~100nm layers of silver the deposition rates tended to be reduced whereas when deposited on to thinner layers of silver a comparatively higher deposition rate was measured. This observation helps to explain the shape of the *series 3* deposition in figure 5.2. Initially (deposition 1, *series 3*) silver is deposited on to 100nm of nickel, at 13J/cm^2, 18nm of silver is deposited overall. As the silver film deposits some self sputtering occurs. The second deposition, at a fluence of 7.8J/cm^2, gives the same deposition rate. At this lower fluence one would expect less material to be removed from the target but also expect less sputtering to occur at the substrate therefore keeping the overall deposition rate the same. The

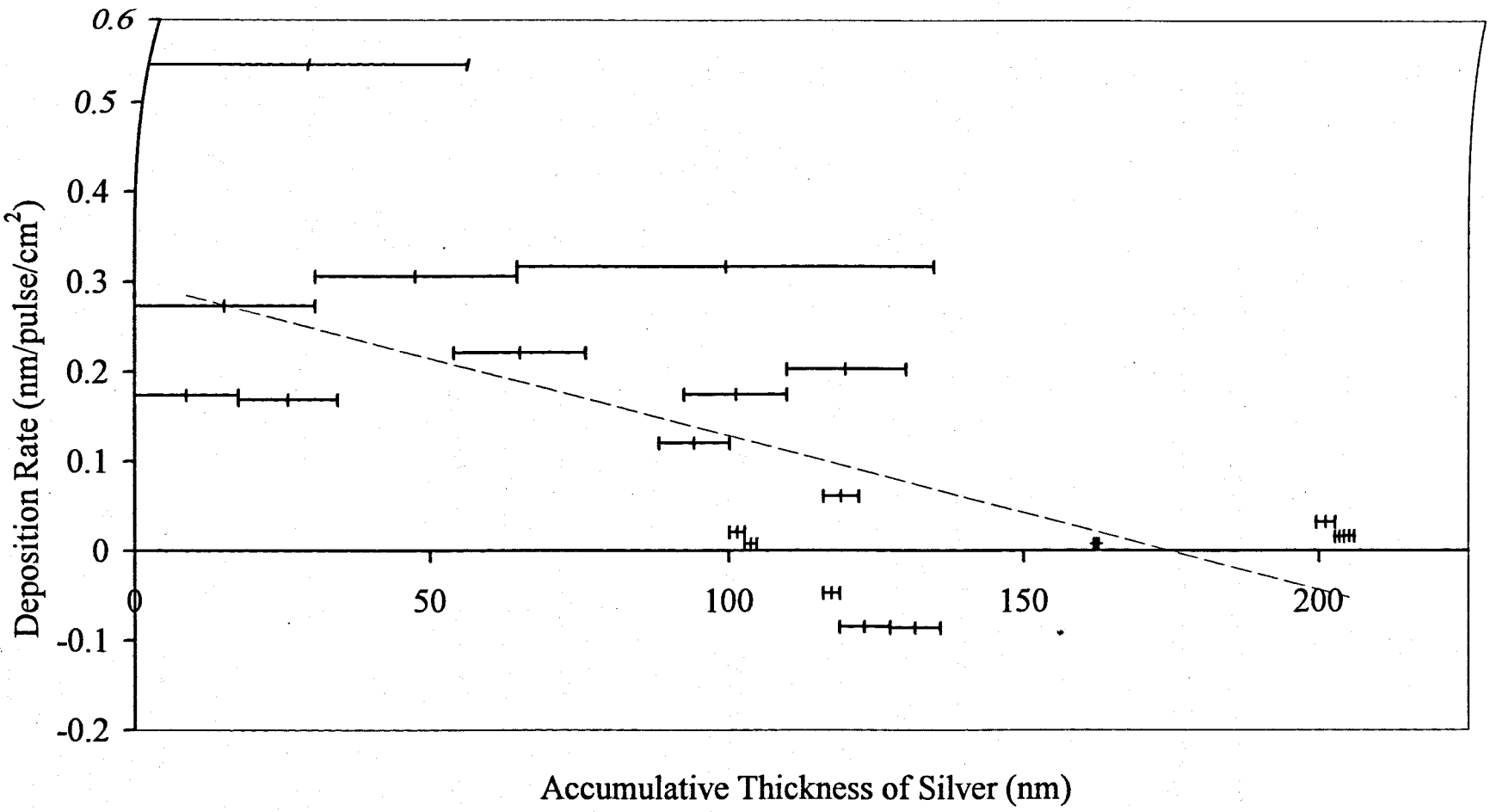

Figure 5.5 Deposition rate of silver measured at fluences >6J/cm^2 at different accumulative thickness given in Tables 5.1 and 5.2. Line shows least squares fit of data.

third deposition is at 5.5J/cm^2 where the effects of sputtering are less again so the overall deposition rate does not decrease. The next three deposition rates down to 1.4J/cm^2 are all below the threshold for sputtering to occur, i.e. <5J/cm^2, and thus the deposition rates give an indication of the amount of material being removed from the target. As the fluences are increased again the 7th measurement is still below the sputtering threshold and does not show a lowered deposition rate. The final depositions, 8, 9 and 10 are all above the sputtering threshold and are carried out onto ~100nm of silver. From the observations in figure 5.5, which suggests that once 100nm of silver is laid down the effects of sputtering can become significant, one might conclude that for depositions, 8, 9 and 10 the rates should be lower than for the first deposition in this series. However a physical explanation supporting the sputtering characteristics observed in figure 5.5 is difficult to describe since the mean free path of silver ions with energy in the region of 30-300eV is much less than 100nm. Hence further work is required to investigate this observation more fully as described in section 7.1. One further point concerns measurement 6 in *series 2*. This measurement appears to have a high deposition rate at a low fluence. The origin of this is not known and it appears to be beyond the spread of the data presented in figure 5.5.

This explanation for the rate limiting deposition can also explain the data in figures 5.1 and 5.4. However, the low fluences and the order in which the depositions were measured (see Table 5.2) mask the effects that previously deposited material have upon deposition rates.

Order	Fluence (J/cm^2)	Deposition rates ($nm/pulse/cm^2$)	Thickness Deposited (nm)	Accumulated Thickness On Quartz Monitor (nm)
Series 248nm				305.7 (Ni)
1	6.6	0.273	30.4	30.4 (Ag)
2	6.6	0.305	34	64.4 (Ag)
3	10.5	0.316	70.3	134.7 (Ag)
4	3.8	0.097	21.3	156 (Ag)
5	2.4	0.025	5.6	161.6 (Ag)
6	3.3	0.049	10.5	172.1 (Ag)

Table 5.2 The silver deposition measurements at 248nm shown in figure 5.1.

In nickel, however, the deposition rates remain fairly stable irrespective of the previous layer. This is indicated in figure 5.6, which shows deposition rates, at fluences $>9J/cm^2$. Figure 5.6 shows that there is no reduction in the deposition rates when depositing nickel on to a nickel layer and suggests that nickel layers are not as readily self sputtered. A tendency for rate limitation at higher fluences may be suggested in figure 5.3, although this is not borne out in figure 5.6. Thus further work at higher fluences is required to establish whether sputtering of nickel films does occur through PLAD.

5.3 The Effects of Laser Wavelength on the Deposition Rates of Nickel and Silver

The results presented in this section were obtained from experiments performed at the Rutherford Appleton Laboratory using the PLAD system described in section 4.4.1.

5.3.1 Threshold fluence

The threshold fluences of nickel and silver are determined from figures 5.1, 5.2, 5.3 and 5.4 are shown in Table 5.3. The values in figures 5.1 and 5.4 were measured as the fluence at which the plasma was no longer visible. The values determined from figures 5.2 and 5.3 were inferred from the other deposition rate data. It is apparent that the threshold fluences for ablation decrease with decreasing

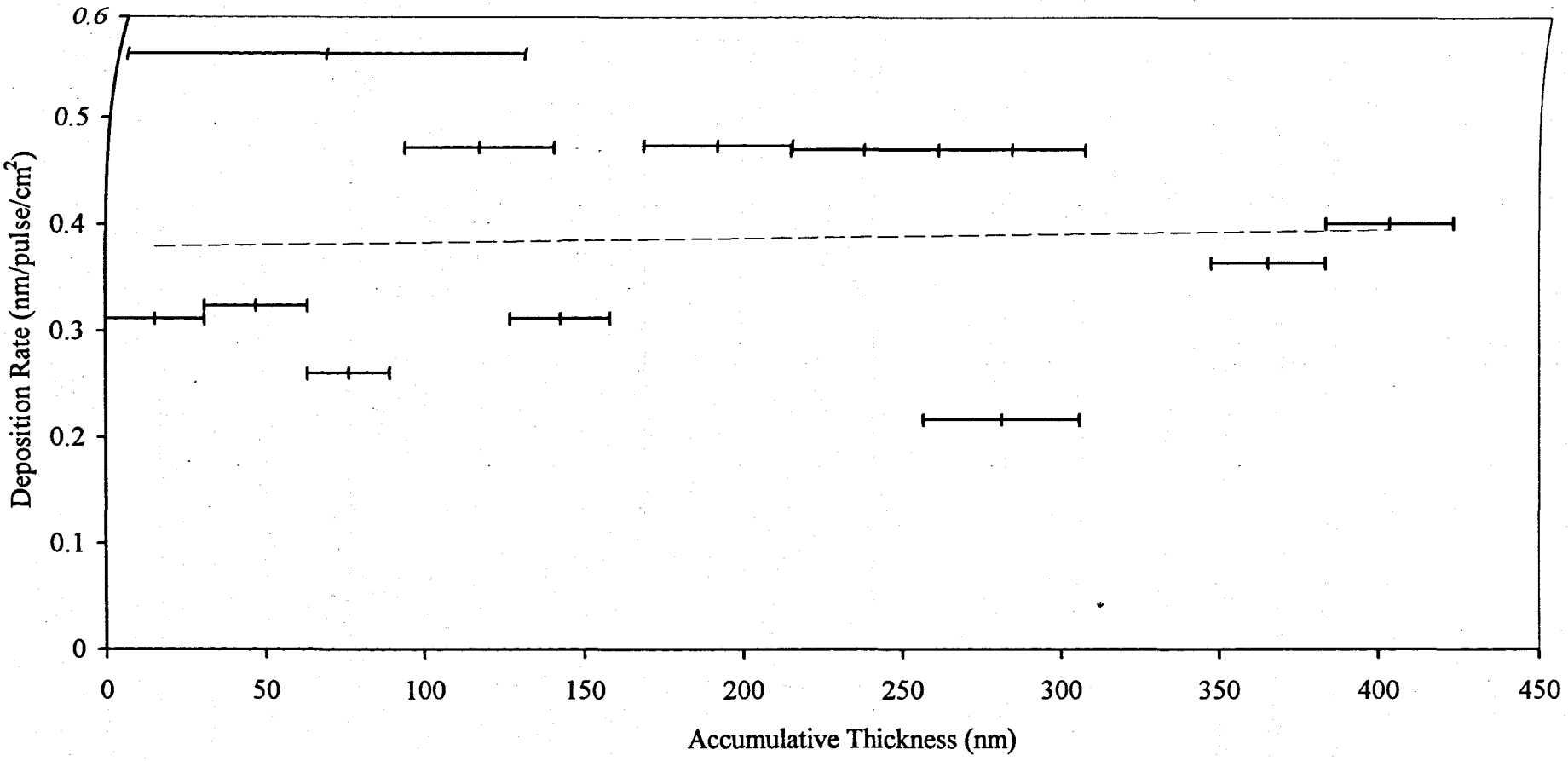

Figure 5.6 Deposition rate of nickel measured at fluences >9J/cm^2 at different accumulative thickness given in Tables A.2 and A.4 (see appendix A). Line shows least squares fit of data.

wavelength for both nickel and sliver. From equation 2.6 we see that the threshold fluence for metals is dependent on the laser wavelength via the reflectivity of the surface. The model predicts that the threshold fluence increases with increasing wavelength as seen in the results. The values calculated in Table 2.1 are however much higher than those obtained from experiment. The model takes into account the energy required to overcome the latent heat of vaporisation. Clearly this is an over simplified model and other processes are involved in laser ablation (Saenger, 1993). For example the model does not take into account absorption of the laser energy by the forming plasma. Although inverse Bremsstrahlung has been ruled out as an absorption mechanism, absorption does still occur although the mechanisms have not yet been clarified (Lunney and Jordan, 1998). However models that do take absorption into consideration give ablation fluences closer to experiment than the model discussed here.

Sample	Wavelength nm	Threshold Fluence J/cm^2 ±10%	Saturation Fluence J/cm^2 ±0.5J/cm^2
Ni	193	0.8	
	248	1.7	
	248*	1.4	
	351	2.3	
Ag	193	1.2	1.8
	248	1.5	4.5
	248*	1.8	3.0
	351	2.0	15.2

Table 5.3 Threshold fluences and saturation fluences for nickel and silver. * signifies values obtained from figures 5.2 and 5.3.

5.3.2 The onset of saturation in the deposition rate

The onset of saturation in the deposition rate is defined as the point at which the initial rise in the deposition rate and saturation deposition rate coincide. These

values are determined from figure 5.1 for silver at 193, 248 and 351nm and from figure 5.2 at 248nm as given in Table 5.3. It is apparent that the onset of saturation in silver occurs at lower fluences at shorter wavelengths until at 193nm saturation it is almost immediate. Chuang and Tam (1989) report a similar wavelength dependence of the saturation of deposition rates. The error in the values determined from these figures is estimated at $\pm 0.5 J/cm^2$. The error arises as a result of the subjectivity of drawing a guide to the eye. This is evident when comparing the saturation fluences determined for 248nm from figures 5.1 and 5.2. In order to reduce the errors involved in determining the saturation fluence further measurements are required.

The saturation deposition rates are all different. This is due to the difficulty of taking spot size and subsequent plasma expansion into account, as discussed in section 5.2. If the deposition data were adjusted so that the saturation deposition rates all coincided then we would see that the initial deposition rate of silver is highest at 193nm and lowest at 351nm in addition to the saturation of the deposition rate occurring at lower fluences for 193nm as shown in figure 5.7. We have seen that the deposition rates of silver are dependent upon the energy of the incoming species and the thickness of silver previously deposited. At 193nm and 351nm the amount of silver previously deposited is usually less than 50nm (see Tables A.1 and A.3 in appendix A) and thus has no significant consequences for self sputtering. Therefore it is the energy of the incoming species that is of most importance in governing the deposition characteristics at the different wavelengths. Metev (1994) has shown that for titanium the average energy of the species in the plasma is lower for shorter wavelengths, see figure 5.8. This would suggest that for the same fluence on the target the average energy of species in the plasma is in fact lower at 193nm than at 351nm. Thus at 193nm there would be less chance of sputtering occurring. This explains why the initial deposition rates for silver are greater at 193nm than at 351nm. It is widely known (Jordan *et al.*, 1995; Fahler and Krebs, 1996) that the average energy of the ions increases with increasing fluence thus as the fluence increases for

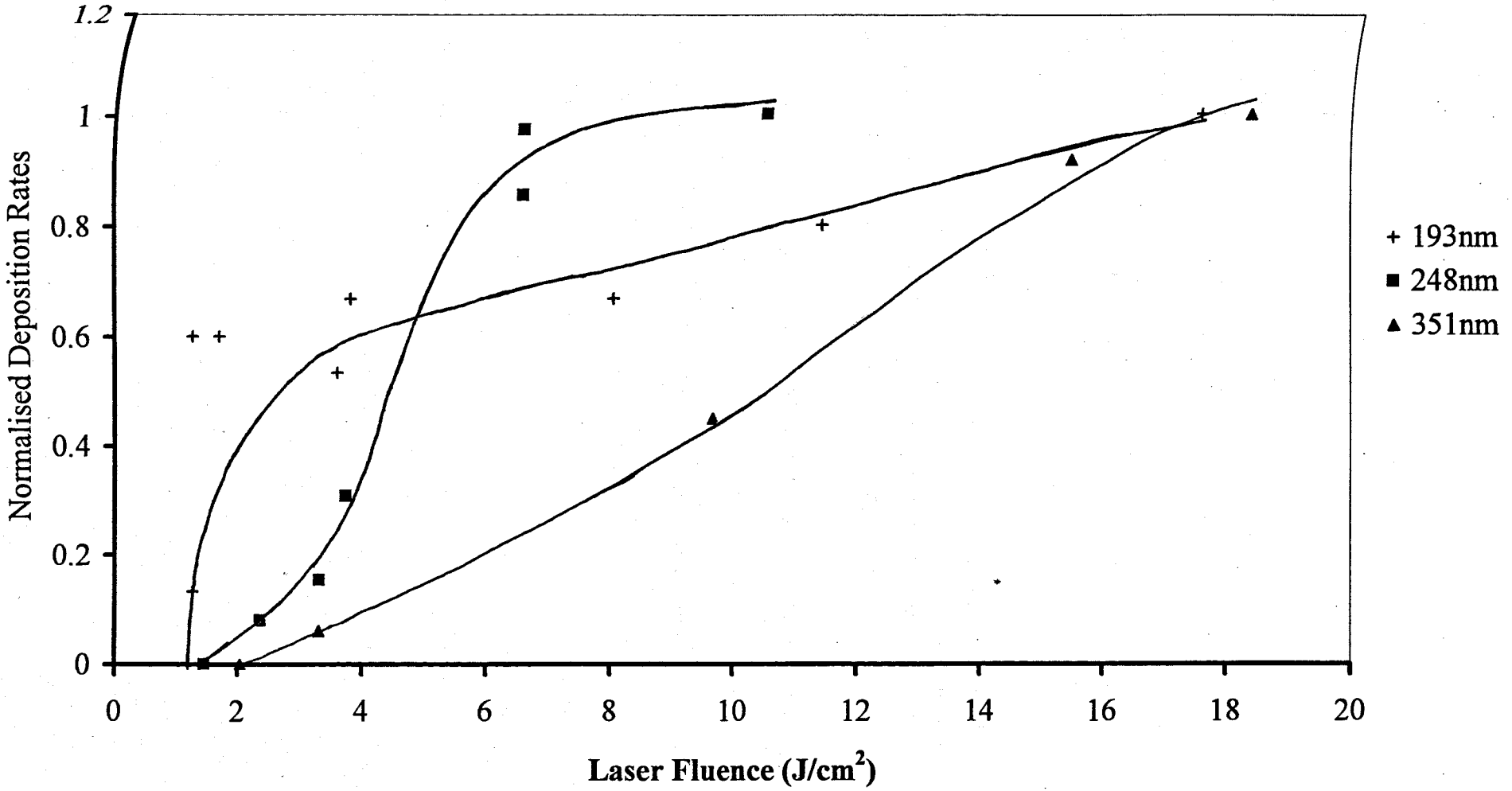

Figure 5.7 Normalised deposition rate for silver

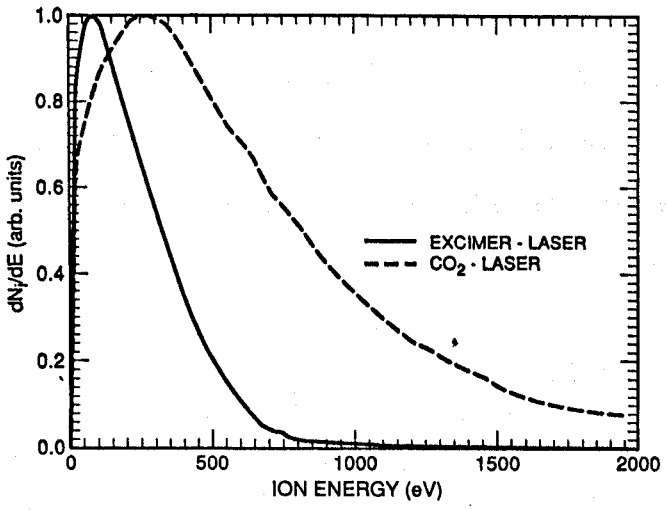

Figure 5.8 Energy distributions of ions in a titanium plasma flux produced using an excimer laser (308nm, τ_p=20ns) and a pulsed CO_2 laser (10.6μm, τ_p=100ns). The energy density is 15J/cm^2. (Metev, 1994).

all of the wavelengths the saturation condition appear to be reached where sputtering becomes significant.

5.4 Discussion of Deposition Rate Characteristics

The deposition rate data in figures 5.1 to 5.6 show that the characteristics of nickel and silver deposition rates could be ascribed to sputtering of the depositing layer. Sputtering yields for silver and nickel ions incident upon silver substrates are much higher than for those ions incident upon nickel. This is indicated in figure 2.2, where the highest sputtering yield is for the self sputtering of silver which is indicative of the reduced deposition rates seen when depositing silver films especially on to a silver surface. Deposition rates of silver on to nickel will be initially high since the yield of nickel from the surface will be negligible in comparison with incident silver ions. As a silver film develops the deposition rate will start to decrease with increasing thickness, as shown by figure 5.5.

For the deposition of nickel on to a silver surface one would expect that silver would be sputtered off giving a lower deposition rate. However since the self sputtering of nickel is negligible a nickel film quickly develops preventing the sputtering of silver from the surface. Thus saturation of nickel deposition rates would only be possible at much higher fluences than for silver.

In general, features of the nickel and silver deposition rates are in agreement with other reported data for metals. For example Svendsen *et al.* (1996) show deposition rates at 355nm for silver that indicate saturation and are thus reminiscent of data reported here in figure 5.1.

Van de Riet *et al.* (1993a) and Jordan *et al.* (1995) have demonstrated the sputtering of species from the substrate by energetic particles in the plasma. Van de Riet *et al.* (1993a) discuss the problem of non-stoichiometric film deposition as a result of preferential etching of species from the substrate. In ablating FeSiRuGa targets is was found that above 3.2J/cm^2 the percentage of gallium in the films was reduced through preferential etching. In the case of copper ablation Jordan *et al.*

(1995) find that at a fluence of only 2J/cm^2 there is significant sputtering at the substrate.

Metev (1986) discusses the laser power density dependence of the maximum film thickness deposited per laser pulse. The maximum film thickness per pulse is shown to saturate at high power densities, this is attributed to sputtering from the substrate by energetic species in the plasma.

Svendsen *et al.* (1996) also show threshold fluences in general agreement with those reported here. From Table 5.3 we see that at 351nm the threshold fluence for nickel is 2.3 J/cm^2, compared with 1J/cm^2 at 355nm measured by Svendsen *et al.* Another feature of the Svendsen *et al.* (1996) results is the scatter in the deposition rate data above 10J/cm^2. This is ascribed to difficulties in reproducibility of the laser beam profile. The results presented here suggest that above 10J/cm^2 sputtering contributes most significantly to the variation in measurements.

From the data presented here we have seen that the deposition rates are dependent upon a number of factors including the thickness of material previously deposited on the substrate and the incoming energy of the species in the plasma. Thus it is concluded that self sputtering does play a significant role in the deposition of films via PLAD. However, in order to make more conclusive statements regarding the role of self sputtering in PLAD a more detailed study of the effects of underlying material on the substrate and further depositions at higher fluences are required. In addition the energy distribution of the ions present in the plasma during deposition should be measured.

5.5 A Comparison of Ablation Rates Measured at the Target

Table 5.4 compares the calculated ablation rates of nickel and silver from the target with measured values. The experimental values were determined from craters left on the target after a 10second exposure to the laser operating at 5.6J/cm^2. This is equivalent to 200 pulses. Calculated values were determined using equation 2.12 (Kelly and Rothenberg, 1985a) in which the temperature was taken as the boiling point temperature and the vapour pressure as 1atm.

	Nickel	Silver
Calculated depth/pulse (nm/pulse)	0.081	0.065
Measured depth/pulse (nm/pulse)	5	4

Table 5.4 Evaporation rates for nickel and silver. Calculated values were obtained using equation 2.12, after Kelly and Rothenberg (1985a). Measured values were obtained from crater depths left on the targets by 200 pulses at 5.6J/cm^2.

We find that the measured removal rate at the target is far higher than estimated from the kinetic evaporation model. This is due in part to the fact that the kinetic model does not extend well to higher temperature and pressures which occur during ablation and therefore the model predicts low ablation depths. For example the evaporation model in Lunney (1995) is not used to estimate ablation rates in copper much beyond 2J/cm^2 where the boiling point tempertaure of the target is exceeded. In the region of 2-3J/cm^2 the model predicts ablation rates of 0.04-20nm/pulse for copper. Above 3J/cm^2 ablation rates of 25-50nm/pulse were measured which agree more closely with the theory presented by Phipps *et al.* (1988), and are much higher that the ablation rates determined using the evaporation model discussed in section 2.2. Boardman *et al.* (1996) show ablation rates for copper, from experiment and theory, as high as 100nm/pulse at fluences of 6J/cm^2. At these higher fluences the ablation rate rises rapidly once the boiling point temperature of the target is exceeded. Svendsen *et al.* (1996) report ablation rates of 1nm/pulse for silver at 2J/cm^2 and 1nm/pulse for nickel at 5J/cm^2. These values are similar to those determined in this thesis for silver and nickel at a fluence of 5J/cm^2. The results in Table 5.4 suggest that the ablation rates measured here are somewhere between values predicted by the evaporation model discussed in section 2.2 and the values obtained for higher fluences as discussed by Lunney (1995) and Boardman *et al.*

(1996). In addition the ablation rates may also be raised if material is also being expelled in the liquid state as droplets.

5.6 The Production of Droplets in Pulsed Laser Ablation Deposition.

The results presented the following subsections were obtained from experiments performed at the Rutherford Appleton Laboratory using the system described in section 4.3.1.

5.6.1 The effect of laser wavelength

The droplet density and the area they cover have been studied as a function of wavelength. In figures 5.9 and 5.10, two nickel films grown at 193nm and 351nm respectively are compared. Similarly figures 5.11 and 5.12 show micrographs of silver films. In each case the films being compared are grown at the same fluence to the same thickness, allowing a direct visual comparison; their growth conditions are summarised in Table 5.5. Two nickel films, grown at the same fluence to different thickness, are also considered where the droplet densities and the area covered for the thinner film are scaled for comparison.

From figures 5.9 and 5.10 it is clear that there are more droplets on the film grown at 351nm and that these droplets appear larger when compared with the film grown at 193nm. A similar trend is seen for the silver films, figures 5.10 and 5.11. This visual comparison is confirmed by the quantitative analysis, showing that fewer droplets are present on the films grown at shorter wavelength.

The results suggest that in the case of metal ablation droplet numbers may depend on the wavelength used. However the reduction in droplet numbers is nowhere near as marked as seen in oxide materials, see for example Misra and Palmer (1991). This is because of the difference in the optical absorption and thermal diffusion between metals and oxides. In oxides $\alpha^{-1} > L_{th}$ where as in metals $L_{th} > \alpha^{-1}$. Therefore in metals one might expect wavelength dependence to be less marked than in oxides since changes in wavelength alter the optical absorption depth.

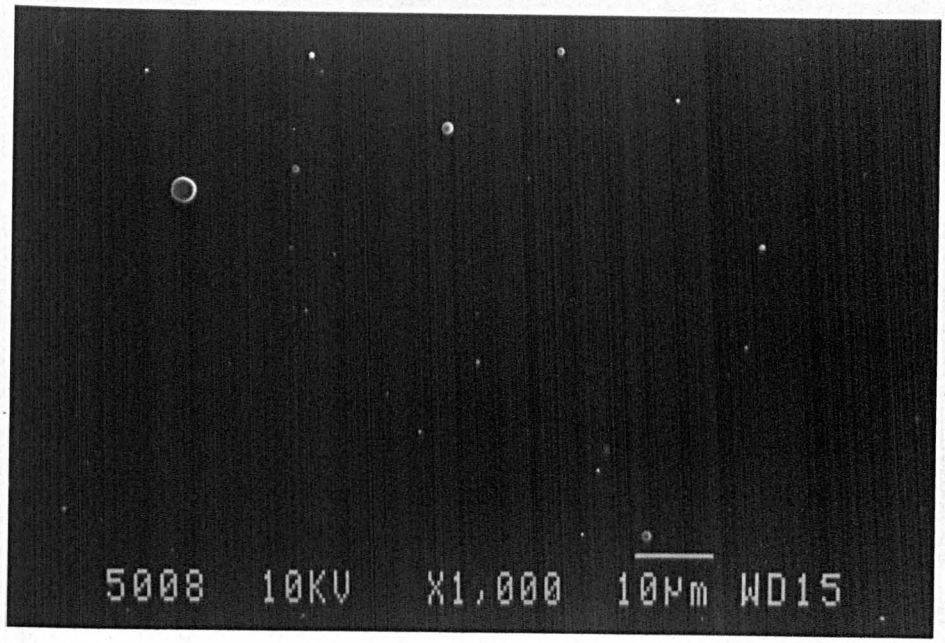

Figure 5.9 Ni film deposited at a fluence of 9.8J/cm^2 to a thickness of 26nm. λ=193nm, τ_p=20ns.

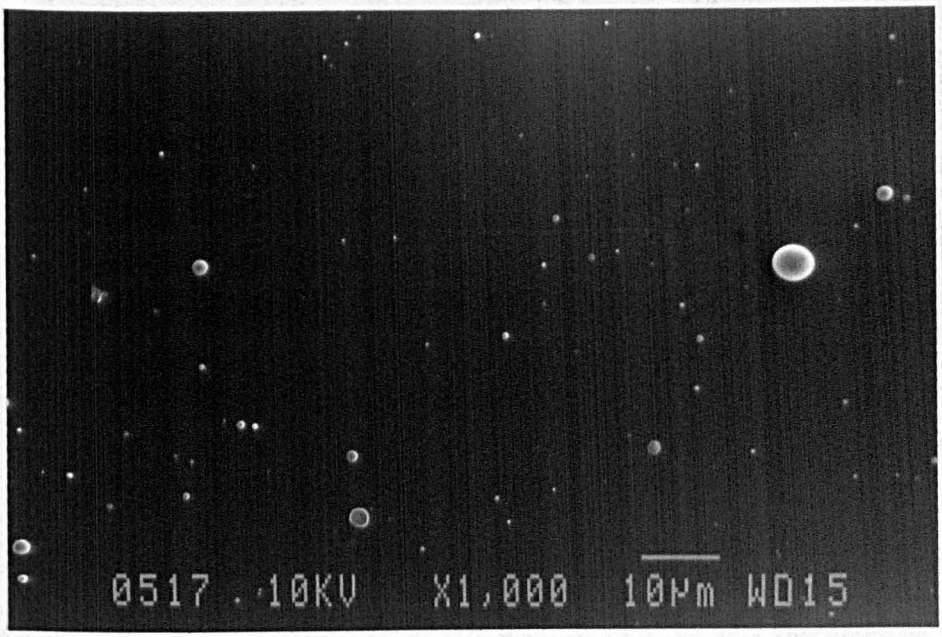

Figure 5.10 Ni film deposited at a fluence of 10J/cm^2 to a thickness of 33nm. λ=351nm, τ_p=20ns.

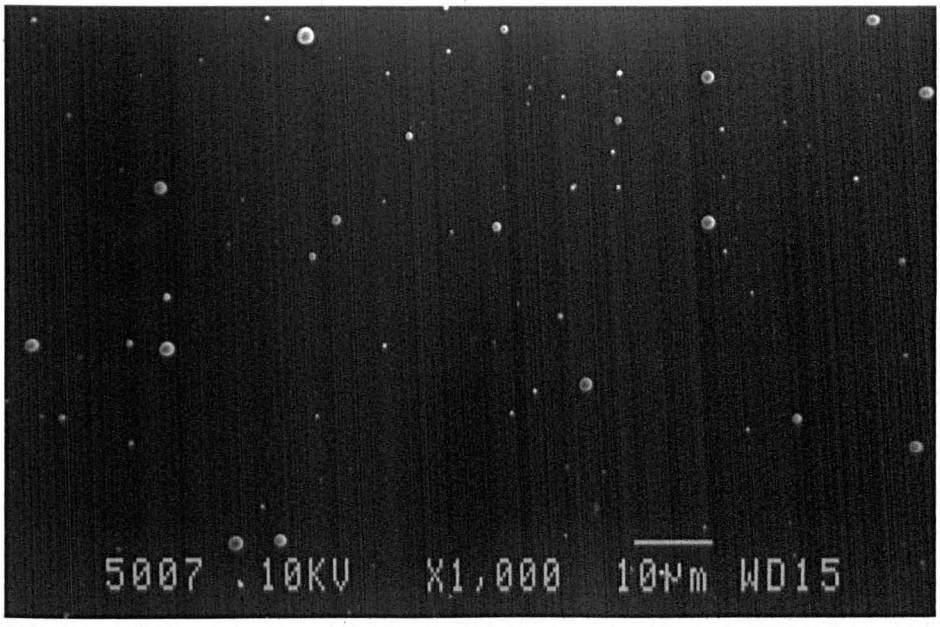

Figure 5.11 Ag film deposited at a fluence of 16J/cm^2 to a thickness of 44nm. λ=193nm, τ_p=20ns.

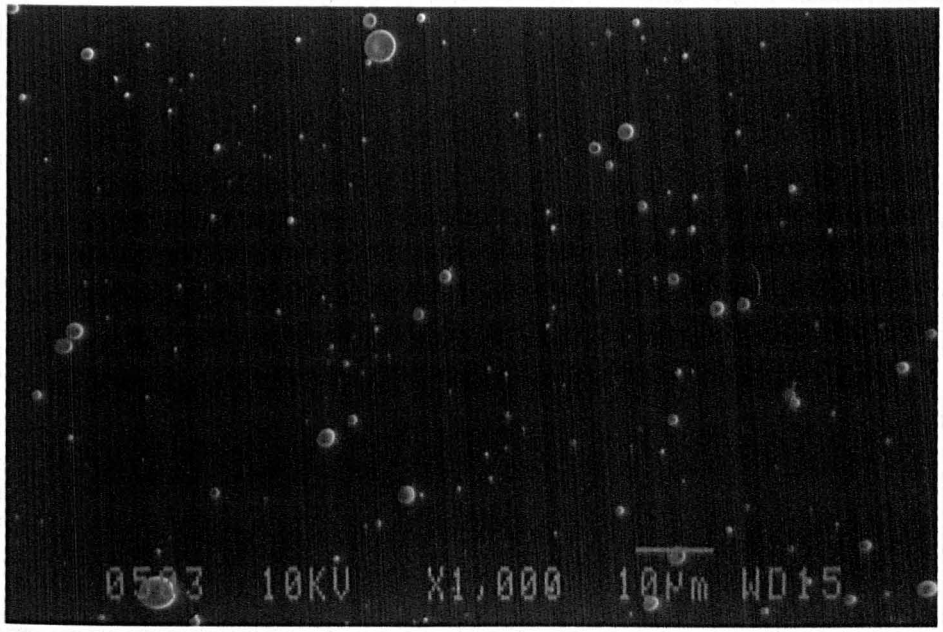

Figure 5.12 Ag film deposited at a fluence of 15J/cm^2 to a thickness of 40nm. λ=351nm, τ_p=20ns.

Sample/ Wavelength	Growth Fluence (J/cm^2) ± 10%	Film Thickness (nm) ± 5nm	Droplet Density ($No./\mu m^2$)x10^{-3} ± 15%	% Area Covered By Droplets ± 15%
Ni 193nm	9.8	26	3.2	0.3
Ni 351nm	10.0	33	7.2	1.1
Ni 193nm	12.4	23	2.5*	0.3*
Ni 351nm	12.7	46	9.2	3.8
Ag 193nm	15.7	44	7.5	1.0
Ag 351nm	15.4	40	13.4	2.2

Table 5.5 Growth conditions and droplet analysis for films grown at different wavelengths. * Values multiplied by 2 to take account of difference in thickness.

5.6.2 The effect of pulse number on droplet production

Some work has shown that droplet numbers vary with the number of pulses that a target sees. For example Kautek *et al.* (1990) and van de Riet *et al.* (1993b) show that the number of droplets increases with roughness at the target which in turn increases with the number of laser pulses incident upon the target. Only a weak dependence of droplet number on wavelength is suggested in the previous section. The dependence of droplet density on the number of pulses during deposition is therefore examined.

The droplet density on the depositing film per laser pulse is determined via the overall droplet density and the deposition time. This assumes that the production of droplets stays constant throughout the deposition time. The translation of the target prevents one area from being repeatedly hit by the laser and thus reduces the overall damage to the target surface. This ensures that the number of droplets does not increase significantly due to the damage at the target surface. In order to test this, further work on ablation from 'virgin' targets and damaged targets would be required.

Films deposited at the same fluence are required in order to compare samples since the differences in fluence lead to differences in droplet production. However the variation in droplet numbers with fluence is not clear. Many workers see an increase

in droplets with increasing fluence (Weaver, 1998; Blank *et al.*, 1992). Whilst a reduction in droplet number with increasing laser fluence has also been reported (van de Riet *et al.*, 1993b; Guilfoyle *et al.*, 1997).

In addition one cannot simply plot droplet density vs number of pulses. Films of similar thickness are required to allow a fair comparison, therefore figures 5.13 shows droplet density/pulse vs thickness of silver films deposited at ~8.1J/cm^2 and of nickel films deposited at 9J/cm^2. Depositions at 193, 248 and 351nm are included in both sets of data. Figure 5.13 shows that the presence of a variation in droplet numbers with the number of pulses is convincing for silver and may occur in nickel. The overall number of droplets produced in nickel is less and therefore further data are required to confirm this.

In contrast the droplet density/pulse for the silver films shown in figures 5.11 and 5.12 and for the nickel film in figure 5.9 and 5.10 are summarised in Table 5.6. Despite the fact that these films have been deposited at the same fluence and thickness there seems to be no correspondence between droplet density and number of pulses. This suggests that further work would be required to establish whether the pulse number dependence or the wavelength dependence has the greatest effect on droplet numbers.

Sample/ Wavelength	Droplet Density (No./μm^2)x10^{-3} ± 15%	Number of Pulses	Droplet Density/Pulse (No./μm^2)x10^{-8} /pulse ± 15%
Ni 193nm	3.2	54540	5.9
Ni 351nm	7.2	60000	12.0
Ag 193nm	7.5	67440	11.12
Ag 351nm	13.4	23080	58.1

Table 5.6 Summary of droplet number/pulse for nickel and silver films shown in figures 5.9, 5.10, 5.11 and 5.12.

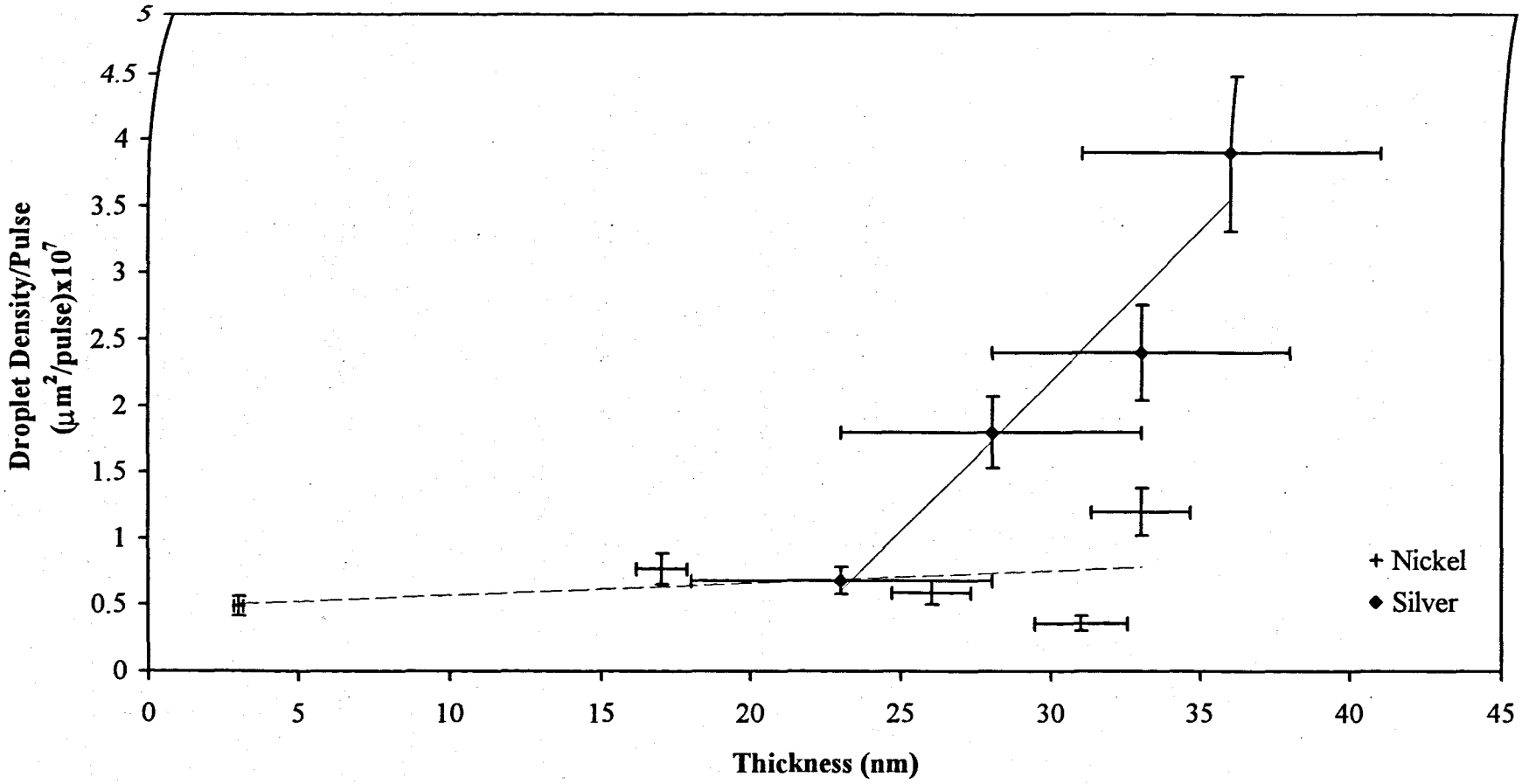

Figure 5.13 Droplet Density/Pulse vs Thickness for nickel films deposited at ~9J/cm^2 and for silver films deposited at ~8.1Jcm^2. Line shows least squares fit of data.

5.6.3 Features on targets irradiated with nanosecond pulses

Figures 5.14 and 5.15 show the targets of nickel and silver after 10 shots of ns pulses. For the silver target the development of asperities leading to droplet emission are apparent. Their sizes are ~3μm, in accordance with the droplet sizes seen on silver films. The same highly developed asperities are not visible on the nickel targets indicating that, compared to silver, droplet emission is not as prevalent. Figures 5.14 and 5.15 indicate that fewer droplets might be expected on nickel films when compared with silver films grown at similar fluences and thickness. For example one should compare figure 5.12, a silver film, with figure 5.16, a nickel film grown at similar fluence to a similar thickness.

The presence of asperities forming on the silver target indicates that the 'most dangerous wavelength' condition for droplet emission has been achieved. From figure 5.15 we measure this characteristic wavelength at A as ~10μm. This is of the same order of magnitude as the values calculated in Table 2.2. The absence of forming asperities on the nickel target suggests that such a condition has not yet been reached, therefore we do not give a measured characteristic wavelength.

By calculating the melt depths of nickel and silver the differences in the features on the targets can be explained. For a target that has melted the surface temperature can be calculated using a modified version of equation 2.3. As it stands equation 2.3 calculates the surface temperature without taking into account the energy required to melt the target. Thus the latent heat of fusion, ΔH_{sl}, can be introduced as an equivalent temperature giving

$$T_s - T_0 \approx \frac{(1-R)I\tau_p}{\rho_m c_{pm} L_{th}} - \frac{\Delta H_{sl}}{c_{pm}} \qquad (5.1)$$

where T_0 is the initial temperature of the target, which for the purposes of this calculation is taken as room temperature. An approximation of the temperature profile can be found in (Weaver, 1998)

$$T(x,\tau_p) = T_{s,\tau_p} e^{-2.2x/L_{th}} \qquad (5.2)$$

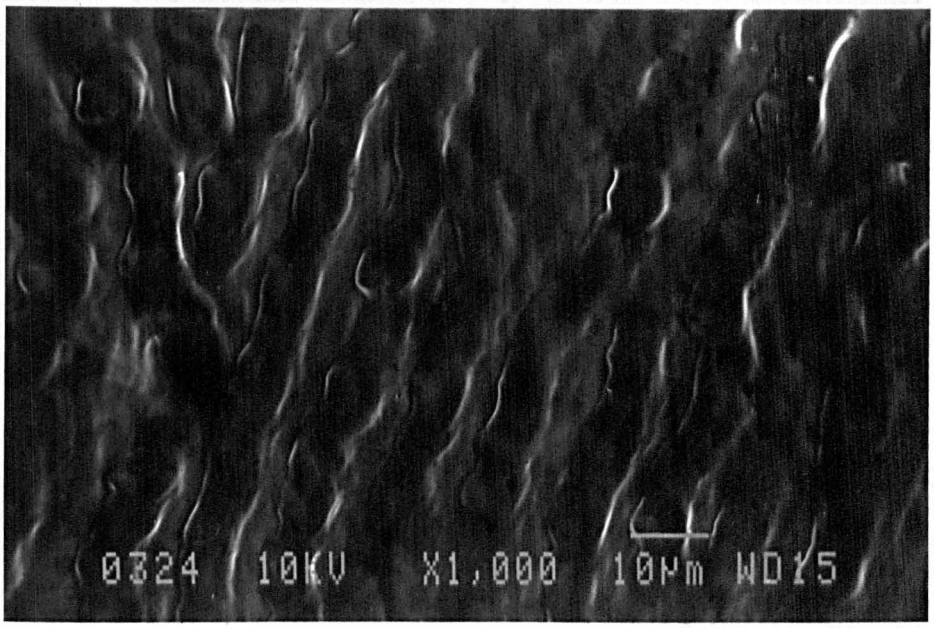

Figure 5.14 Ablated Ni target after 10 pulses at a fluence of the order of 10J/cm^2. λ=248nm, τ_p=20ns.

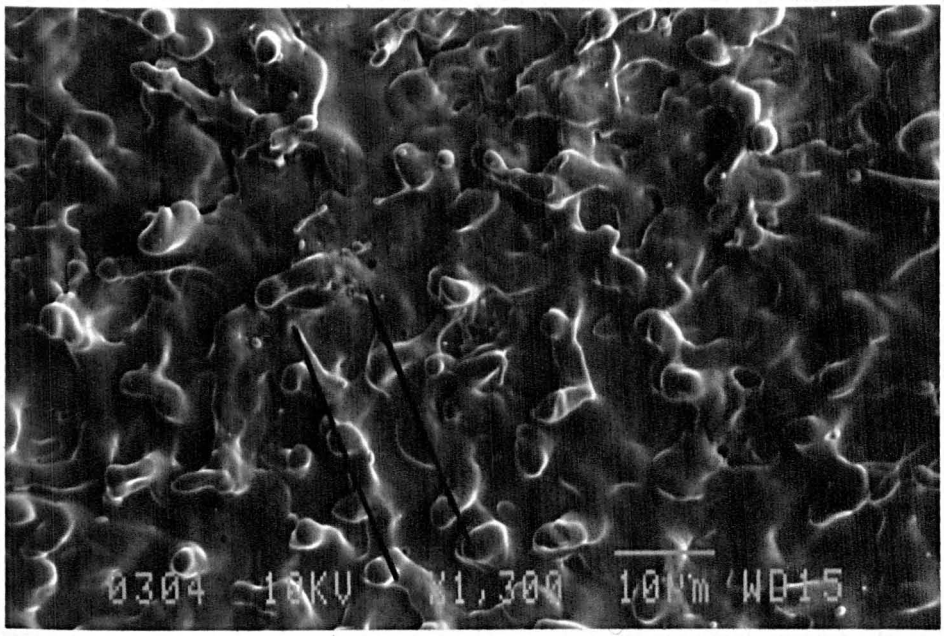

Figure 5.15 Ablated Ag target after 10 pulses at a fluence of the order of 10J/cm^2. λ=248nm, τ_p=20ns. The characteristic wavelength is indicated at A.

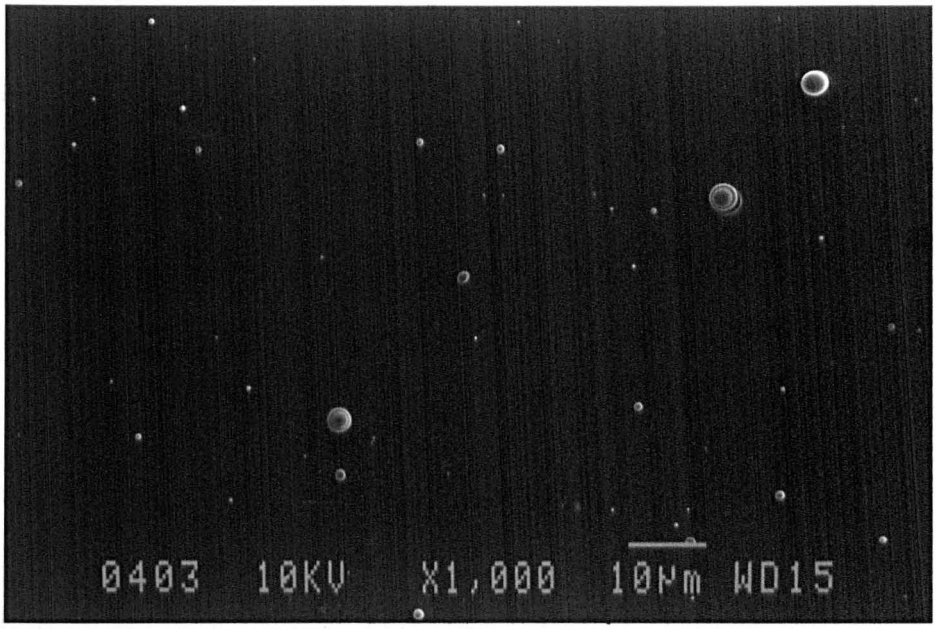

Figure 5.16 Ni film deposited at a fluence of 16J/cm^2 to a thickness of 39nm. λ=351nm, τ_p=20ns.

where $T_{s,\tau p}$ is taken as the surface temperature at the end of the laser pulse. The melt depth x_m is then given by

$$x_m = \frac{L_{th}}{2.2} \ln\left(\frac{T_{s,\tau_p}}{T_m}\right) \qquad (5.3)$$

Using equation 5.1 and 5.3 the melt depths after one pulse were calculated as 0.5μm and 1.9μm for nickel and silver respectively. Where the fluence was 5.6J/cm^2, τ_p=20ns and L_{th} was 0.68μm and 2.6μm for nickel and silver respectively. Although the targets shown in figures 5.14 and 5.15 have been subjected to 10 pulses there is sufficient time between pulses for the region of interest on the target to cool completely. Therefore the melt depths for nickel and silver are calculated for one pulse, i.e., 0.5μm and 1.9μm respectively. This calculation shows that for the same fluences less melting occurs on nickel than on silver. This is borne out in figures 5.14 and 5.15, which show less melting on nickel than on silver. Thus the production of droplets from nickel is less prevalent than for silver at the same fluence as already shown by figure 5.12 and 5.16. It must be noted that this calculation only gives an approximate value for the melt depths since the calculation of the surface temperature gives values in excess of the critical temperatures determined by Martynyuk (1983) which far exceeds the validity of the model.

5.7 The Effects of Laser Pulse Temporal Profile on the Deposition Characteristics of Nickel and Silver.

The data presented in this section was intended to show the effects of reducing the laser pulse length on the deposition rate characteristic and the production of droplets in PLAD. However for technical reasons associated with the production of ps pulse lengths at a wavelength of 248nm it is questionable whether a purely ps regime was achieved.

The results presented in the following subsections were obtained from experiments performed at the Rutherford Appleton Laboratory using the deposition system described in section 4.4.2.

5.7.1 The laser pulse profiles

Schematic representations of the pulse profiles seen on an oscilloscope are shown in figures 4.1 and 4.2 of the experimental procedures. The pulse profiles shown in figures 4.1 and 4.2 are 25ns envelope with an associated background energy. Superimposed upon the background are firstly sixteen 5ps pulses for the pulse train profile (figure 4.1) and secondly a single 5ps pulse for the single ps profile (figure 4.2). The background present in these pulse profiles is attributed to amplified spontaneous emission (ASE). Hence we need to calculate the energy associated with each part of the envelope to know how much the background energy associated with the pulse envelopes contributes to the ablation process.

During deposition the repetition rate of these envelope was 20Hz. From the average power, P_{ave}, measured using a power meter, see section 4.2, the power per pulse envelope was given by $P_{ave}/20$. To determine the energy associated with each part of the pulse an approximation of the areas under the pulses is required. For figure 4.2 we approximate the pre-pulse area as $\frac{1}{2}\times25\times10^{-9}\times0.8=1.0\times10^{-8}$units of area and similarly for the ps pulse $=1\times10^{-11}$units of area. This implies that most of the energy associated with the envelope is associated with the background radiation. A similar process applies for the ps pulse train with less than 0.1% of the energy of the pulse envelope being associated with individual ps pulses.

To calculate how much each part of the pulse profile contributes to the heating of the target we will use equation 2.3, which predicts the change in the surface temperature. For 5ps pulses the thermal diffusion length is calculated as 1.1×10^{-6}cm for nickel and 4.1×10^{-6}cm for silver. For a measured average power of 0.6W the fluence associated with the ns background is 3.86J/cm^2 and for a ps pulse $3.9\times10^{-3}\text{J/cm}^2$, using the method described earlier in this section. The change in temperature for nickel and silver due to the ns and ps parts of the pulse profile are shown in Table 5.7.

Pulse Length	Change in Surface Temperature (K)	
	Nickel	Silver
25ns	5600	4000
5ps	400	280

Table 5.7 shows the change in surface temperature of nickel and silver targets for isolated ns and ps features of the pulse profile as predicted by equation 2.3. The values take into account the ±10% error associated with the fluences of the ns and ps parts of the pulse profile.

This shows that the amount of energy associated with the ps part of the pulse profile has little effect on the heating of the target. The fluence associated with the background is significant for metal ablation and thus it is expected that the background makes a significant contribution to the ablation process. This brings into question the validity of considering the pulse profiles as single, isolated picosecond pulses. These points are borne in mind when interpreting the deposition data and the number of droplets produced in the deposition process.

5.7.2 The deposition rates of nickel and silver

The deposition rate data for single 5 picosecond pulses and a train of sixteen 5ps pulses in a 25ns envelope are compared in figures 5.17 and 5.18. The production of these pulses is described in section 4.4.2. Deposition rates are presented in nm/pulse/cm^2 to take into account the different number of ps pulses per second and nm/envelope/cm^2 to allow comparison with ns ablation in section 5.2. From figure 4.1 we see that the envelope contains 16 picosecond pulses and from figure 4.2 it contains 1 picosecond pulse. The fluences associated with the individual ps pulses and the ns background are also shown. The errors in the deposition rates and fluences are 10%. In some cases the error bars are omitted from the figures for clarity.

The two contributing factors, i.e., the ps pulses and the ns background, make it difficult to interpret the deposition rate data in the two picosecond profiles. In figure 5.17 the deposition rates are of the same order of magnitude as those seen for

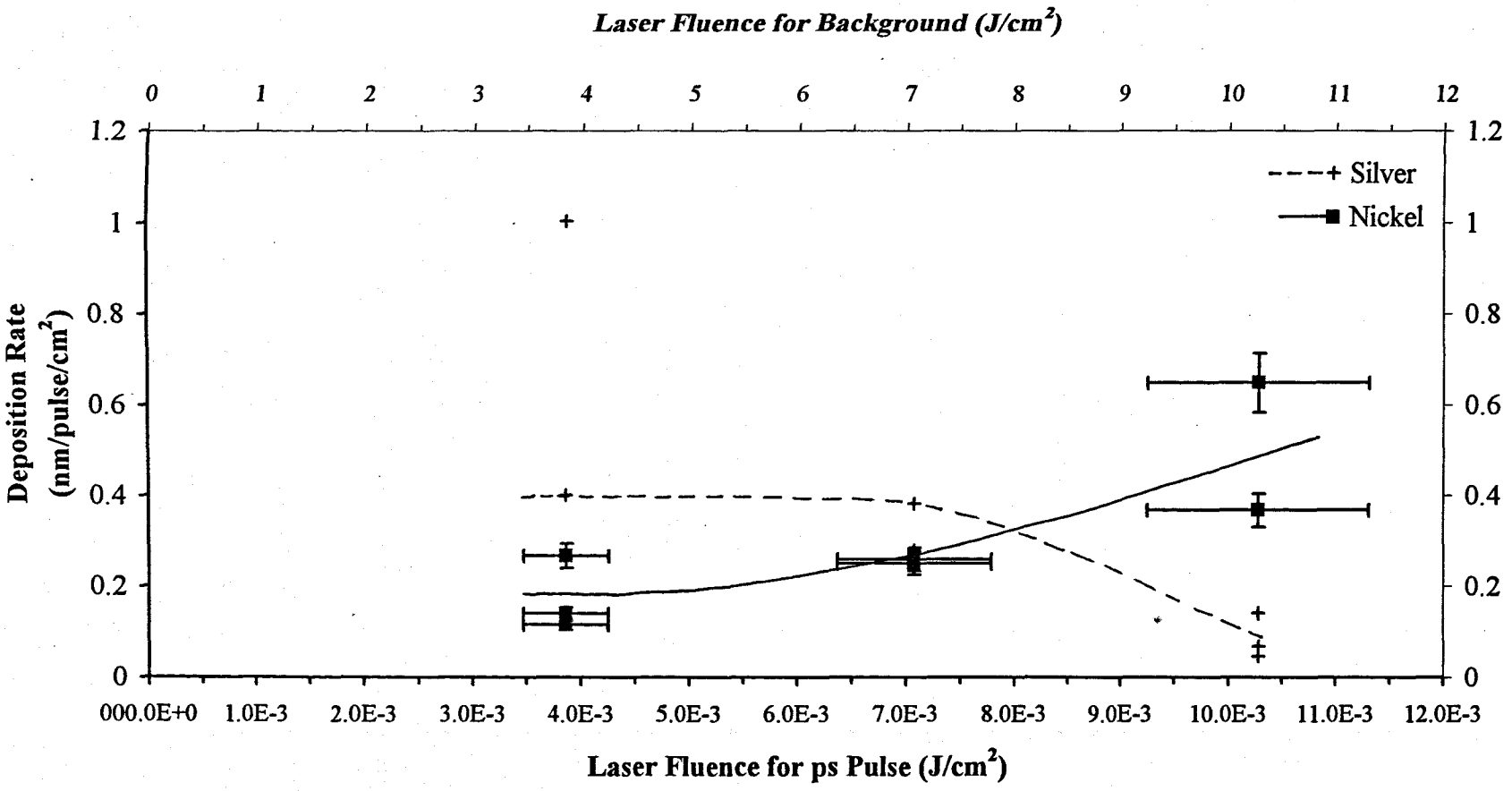

Figure 5.17 Deposition Rates of silver and nickel using the single ps pulse profile. The bottom x-axis values are the fluence of the individual ps pulses and the top axis is associated with the ns background. For clarity error bars are show for Ni only.

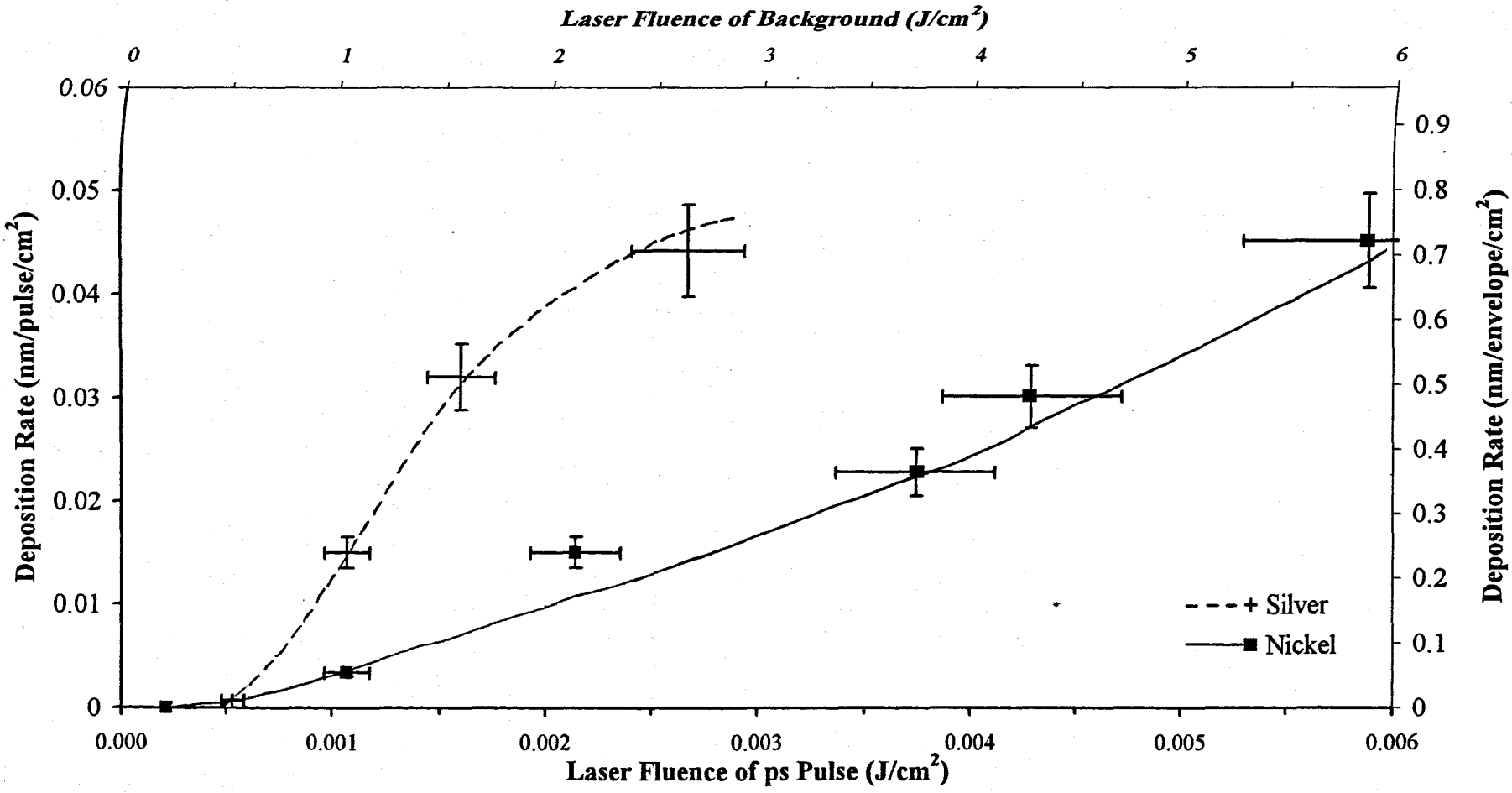

Figure 5.18 Deposition rates for silver and nickel using ps pulse train profile. The deposition rates per ps pulse and per envelope are shown on the y-axes. The fluences for the ps pulses and background are shown on the x-axes.

ns pulses (figures 5.1, 5.2, 5.3 and 5.4) suggesting that the background radiation has a strong influence on the ablation process. For the silver deposition (figure 5.17) there is a wide spread in the data. This is attributed to an increased amount of self sputtering and illustrates the difficulty in achieving reproducibility.

Order	Fluence (ps/ns pulses) (J/cm^2)		Deposition rates ($nm/pulse/cm^2$)	Thickness Deposited (nm)	Accumulated Thickness On Quartz Monitor (nm)
Single ps profile	ps	ns			55 (Ag)
1	0.007	7.4	0.28	10	65 (Ag)
2	0.007	7.4	0.26	9.2	9.2 (Ni)
3	0.01	10	0.37	13	22.2 (Ni)
4	0.01	10	0.14	5.1	5.1 (Ag)
5	0.01	10	0.069	2.5	7.6 (Ag)
6	0.004	4	1.0	36	43.6 (Ag)
7	0.004	4	0.12	4.2	4.2 (Ni)
8	0.004	4	0.14	5.0	9.2 (Ni)

Table 5.8 The nickel and silver deposition measurements shown in figure 5.17. λ=248nm.

The deposition rate data in figure 5.17 is a mixture of measurements taken using a quartz crystal monitor and rates determined from deposited films of known thickness and deposition time. The order in which the deposition rates of silver and nickel were measured on the crystal are summarised in Table 5.8.

If we compare the first silver deposition rate of 0.28nm/pulse/cm^2 at a ns fluence of 7.4J/cm^2 (i.e., a ps fluence of 0.007J/cm^2) it is the same as that seen in figure 5.1. At a higher fluence the deposition rate falls to 0.14nm/pulse/cm^2 and is further reduced to 0.069nm/pulse/cm^2 as the silver layer starts to form. Again these values correspond with those seen previously for ns ablation of silver. Finally the deposition at the lower fluence of 4J/cm^2 is elevated at 1.0nm/pulse/cm^2. This result does not fit with the remaining data and exceeds the high deposition rate seen in *series 2* of figure 5.2. This suggests that an error occurred whilst measuring this result. One possibility is that a jump in the frequency of the crystal oscillator occurred. The similarities of the deposition rate data with those shown in figures 5.2 and 5.1 further confirms that the ns background is the dominant contributor to the ablation process. In addition for ns fluences of 7.4J/cm^2 and 10J/cm^2 sputtering would be expected and this is suggested for the silver deposition rate data by the reduction in deposition rate as fluence increases.

For nickel there is an increase in the deposition rate with fluence as expected. Again we see that the deposition of nickel is less problematic and this is attributed to the reduced amount of sputtering that occurs during the nickel deposition compared with silver deposition. The deposition rate for nickel at 7.4J/cm^2 is given as 0.2nm/pulse/cm^2. This compares favourably with values of 0.2-0.4nm/pulse/cm^2 seen in figures 5.3 and 5.4 at similar fluences.

Despite reporting the deposition rate data in units of nm/pulse/cm^2 to show the deposition per ps pulse it is clear that the dominance of the ns background in the ablation process masks this measurement. The deposition rate data are associated with the entire pulse envelope as reflected by the results.

In figure 5.18 the deposition rates per ps pulse and per pulse envelope are shown. The effects of the ps and ns parts of the profile are difficult to elucidate for the ps train profile. When compared with the ns ablation of silver in figures 5.1 and 5.2 the deposition rates per envelopes are far too high for the laser fluences associated with the ns background. For example, in figure 5.1 the deposition rate at 248nm is

less than 0.05nm/pulse/cm^2 below 3J/cm^2. This is more comparable with the deposition rate associates with the ps pulses in figure 5.18. However the method used in calculating the deposition rates associated with the ps pulse may explain why this is the case and lead us again to the conclusion that the ns background is dominant in the ablation process.

The deposition rate is determined by dividing the deposition rate per second by 20 to get the deposition per envelope and then again by 16 to get the deposition per ps pulse. However, while the ps pulse is 5ps long, the time allocated to calculating the ps pulse deposition rate is 1.7ns. 5ps is only 0.3% of this time and thus for 99.7% of the time only the ns background is incident upon the target. Therefore the influence of the background is also important in the ps pulse train regime.

From the data given it is difficult to say whether the silver deposition rate saturates. According to the ns saturation characteristics we would not expect to see saturation at fluences as low as 3J/cm^2. Thus if the ns background is dominant we would not expect saturation to occur. However it could be suggested from the deposition rate data that saturation may occur even though there is evidence that the individual ps pulses do not contain sufficient energy to increase the kinetic energy of the ablated species to cause sputtering at these low fluences. To confirm whether saturation does occur more data are required in this and higher fluence regions.

In summary, deconvoluting the ps and ns contributions to the ablation process causes difficulty in interpreting deposition rate data obtained using the ps profiles. The values of the deposition rates indicate that the ns background contributes most significantly to the ablation process. As for the silver deposition rates seen in figures 5.1 and 5.2 there is evidence for some sputtering of the depositing films at higher fluences seen in figure 5.17. This results in a reduction in the deposition rates at high fluences and also makes reproducing data more difficult. For nickel, where sputtering is not so prevalent, the reproducibility of the deposition rate characteristics is much improved.

5.7.3 Threshold fluences for picosecond pulse profiles

The calculated and measured threshold fluences for the ns background and the individual ps pulses are given in Table 5.9. The values are calculated using equation 2.6. As for the threshold fluences determined in Table 5.3 the calculated values are larger than the measured values.

	Measured Threshold Fluences (J/cm^2) ±10%		Calculated Threshold Fluences (J/cm^2)	
	ps pulse	ns background	ps pulse	ns background
Nickel	0.014	1.4	0.10	7.3
Silver	0.014	1.4	0.13	9.0

Table 5.9 shows the measured and calculated threshold fluences for ps pulses and ns background. The ps pulse data is determined from figure 5.18.

The measured values for the ns background are similar to the values determined for silver and nickel in Table 5.9. This further increases support for the ns background being dominant in the ablation process for the ps profiles.

5.7.4 Ablation rates measured at the target for picosecond profiles

Ablation rates calculated for individual ps pulses and for the ns background are shown in Table 5.10. These values are calculated using equation 2.12.

	Nickel	**Silver**
ps pulse ablation rate (nm/pulse)	2.0×10^{-5}	1.6×10^{-5}
ns background ablation rate (nm/pulse)	0.100	0.081

Table 5.10 Evaporation rates for nickel and silver for the ps profile. The values are calculated using equation 2.12, after Kelly and Rothenberg (1985a).

A measured ablation rate of 1.4nm/pulse was determined for nickel. The silver target was too rough to determine the ablation rate. The measured value is higher than the calculated values for both the ps pulse and ns background. As already discussed in section 5.3.1 the calculated values are only determined at boiling point temperatures and a pressure of 1atmosphere since the model does not extend well to elevated temperatures and pressures. We also see that the calculated values show that ablation due to the ps pulses is negligible compared to the ns background as indicated throughout these results.

5.8 The Effects of Laser Pulse Profile on the Production of Droplets in Pulsed Laser Ablation Deposition.

The results presented in the following subsections were obtained from experiments performed at the Rutherford Appleton Laboratory using the deposition system described in section 4.4.2.

As already seen for ns pulses molten droplets are a feature of the ablation process, where molten material at the target is expelled by the recoil pressure associated with the developing plume. The reduction of such melting might result in the elimination of droplets from metal films deposited by PLAD.

Thus in metals when using shorter pulse lengths for deposition the transfer of energy to the lattice which heats the target and causes melting needs to be taken into consideration. Work on laser drilling of metallic samples using ns, ps and fs pulses indicates less melting of metals at shorter pulse lengths (Luft *et al.*, 1996; Chichkov *et al.*, 1996; Jandeleit *et al.*, 1996). At shorter pulse lengths the heat affected zone in the laser drilled holes is also reduced. This suggests that moving to even shorter pulse lengths could be advantageous in avoiding droplet production. However this would be at the expense of high deposition rates (Preuss *et al.*, 1995). However for silver and nickel the electron-phonon relaxation times, $\tau_{e\text{-}p}$, are 1-2 ps (Groneveld *et al.*, 1995; Preuss *et al.*, 1994) and thus for 5ps pulses there is sufficient time for melting to occur. In addition we also have the melting due to the ns background. Thus

molten material is present on the target and leads to droplets being expelled on to the film.

In this section the number of droplets on films deposited using the ps pulse train and the single ps pulse profile described in section 4.4.2 are compared with films deposited using a 20ns pulse as in section 4.4.1. Films of similar thickness are compared to show visually the differences in the ns and ps regimes. Figure 5.19 is a silver film deposited using ns pulses at a fluence of $6.8J/cm^2$. Figure 5.20 shows a silver film deposited using single ps pulses with a fluence of $3.9\times10^{-3}J/cm^2$, with a background fluence of $3.9J/cm^2$. Both films are 10±2nm thick. Figures 5.21 and 5.22 are silver films deposited by ns pulses and ps pulse trains respectively. The fluence for the ns pulses is $7.2\ J/cm^2$ and for the ps pulses $1.6J/cm^2$ for the background and $1.6\times10^{-3}J/cm^2$ for the ps pulses. Both films are 28±2nm thick. In both cases the silver films deposited in the ps pulse regime have the greater number of droplets on them despite being deposited at a lower background fluence. A similar correspondence is seen on nickel films when comparing figure 5.23 with figure 5.24 and figure 5.25 with figure 5.26. Again more small droplets are present on the nickel films deposited using the ps pulses, although with droplets being less prevalent on nickel films it is not as easily shown.

Despite the expectation that moving to a shorter pulse length would reduce the number of droplets the results have not shown this. Suggestions have already been presented to explain this counter intuitive result. One factor affecting the ablation in both of the ps regimes is the background radiation associated with each envelope. This background basically gives nanosecond ablation characteristics which heats the target and causes melting at the surface. The ps pulses then provide an additional impulse which results in the recoil of the molten surface splashing molten material onto the films. This process is discussed in detail below showing the extent of melting caused by the background radiation and the increased pressure exerted on the molten surface by a ps pulse which results in an increased number of droplets being deposited onto the films.

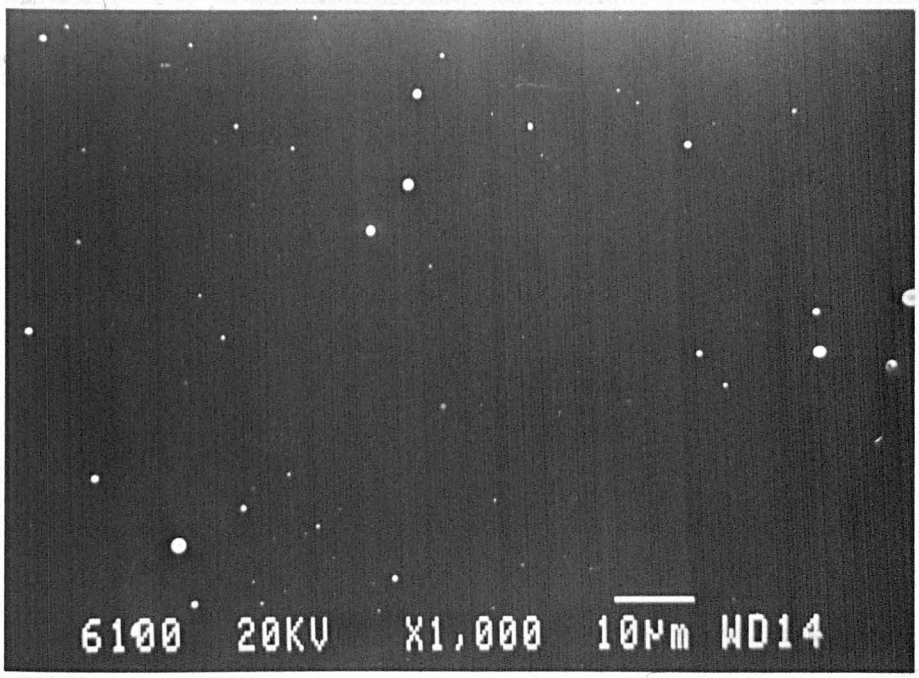

Figure 5.19 A 10nm silver film deposited using 20ns pulse length, 6.8J/cm^2. λ=248nm.

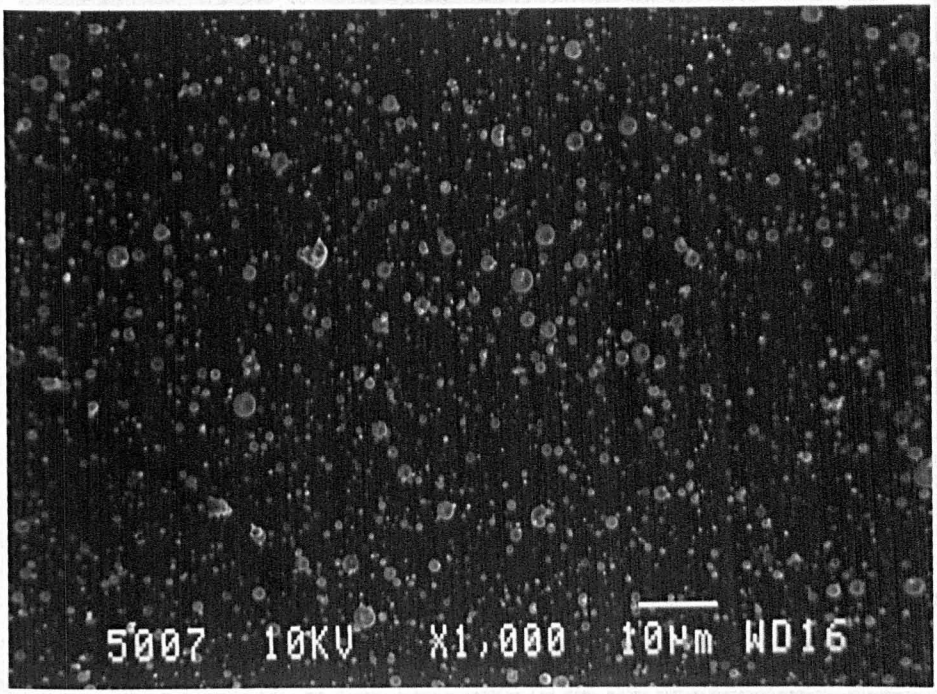

Figure 5.20 A 10nm silver film deposited using the single ps pulse regime, with individual ps pulse fluence of 3.9×10^{-3}J/cm^2 and ns background fluence 3.9J/cm^2. λ=248nm.

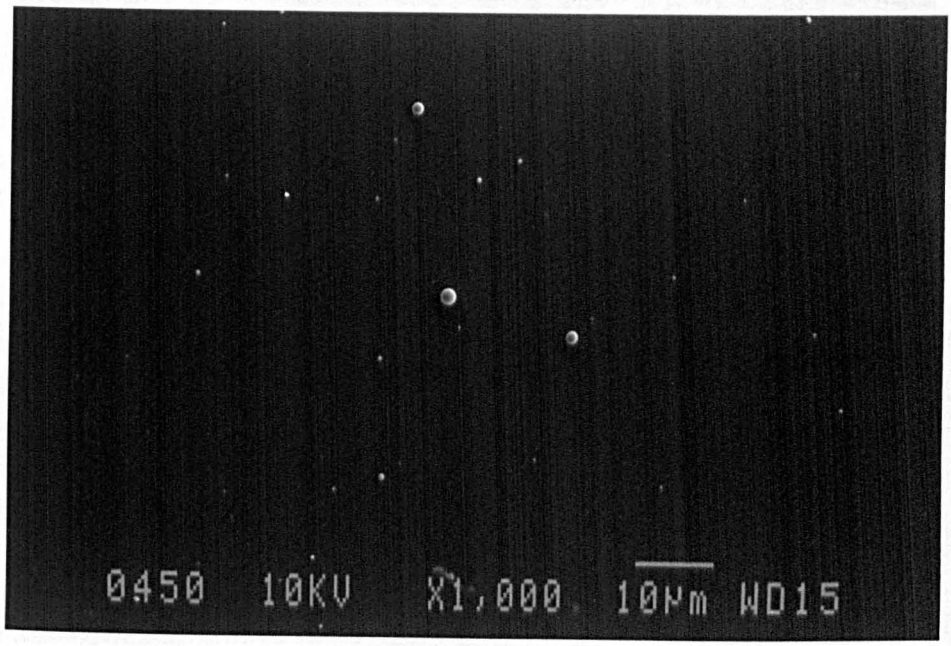

Figure 5.21 A 28nm silver film deposited using 20ns pulse length, 7.2J/cm^2. λ=248nm.

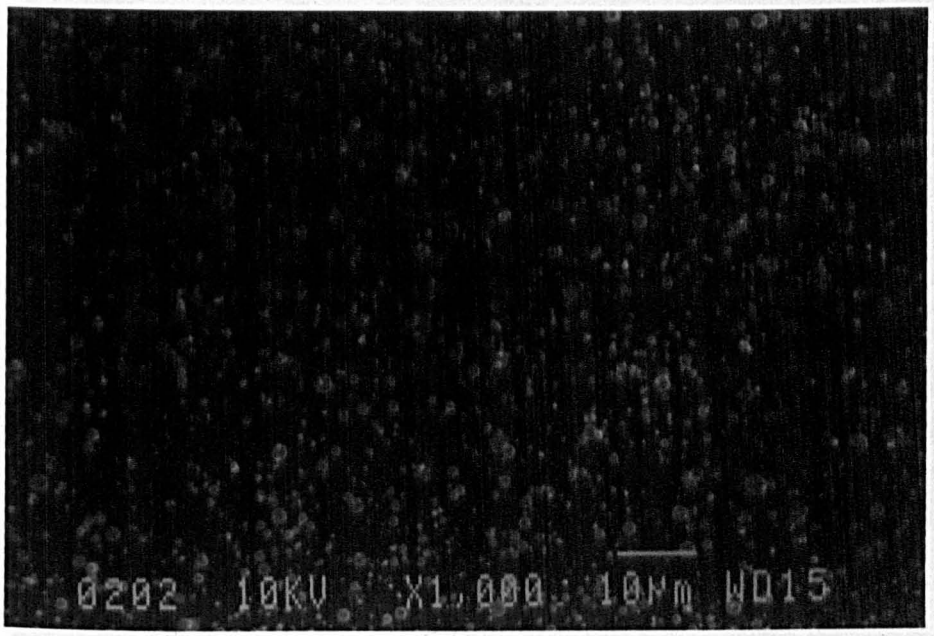

Figure 5.22 A 28nm silver film deposited using the ps pulse train, with individual ps pulse fluence of 1.0×10^{-3}J/cm^2 and ns background fluence 0.01J/cm^2. λ=248nm.

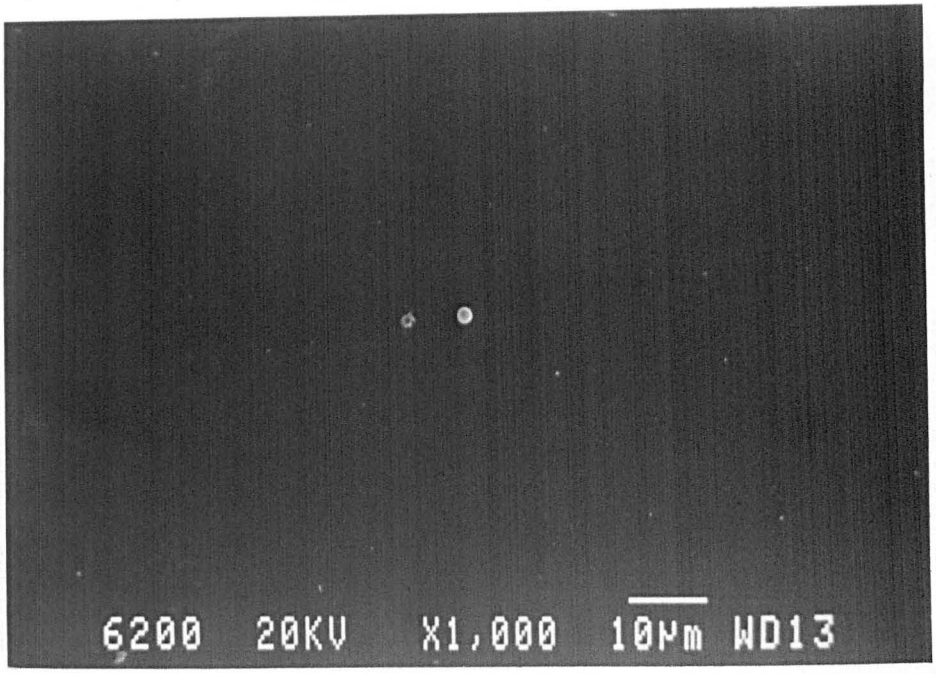

Figure 5.23 A 27nm nickel film deposited using 20ns pulse length, 15J/cm^2. λ=248nm.

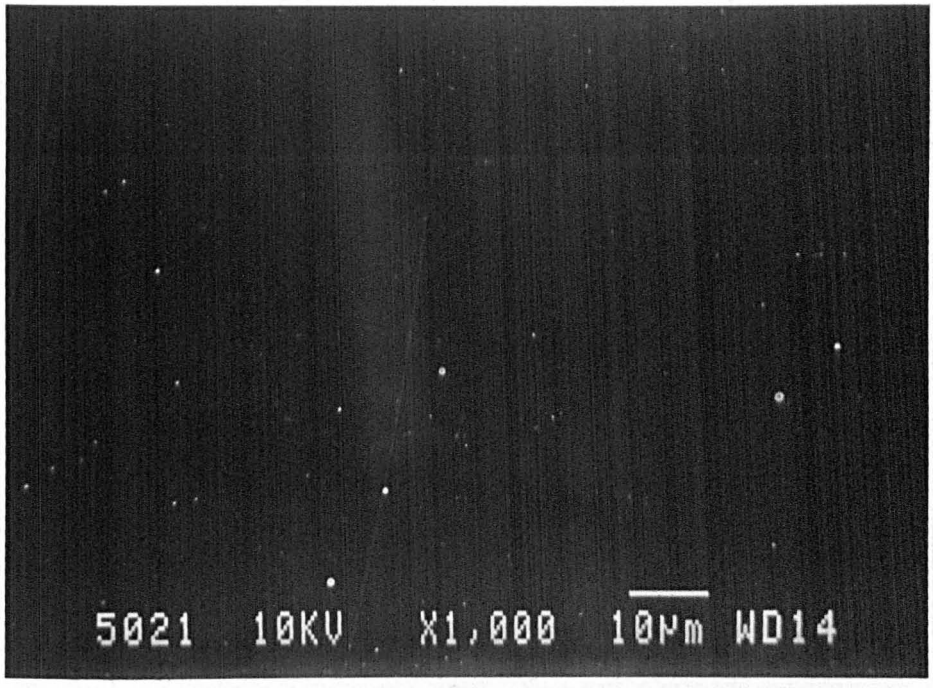

Figure 5.24 A 24nm nickel film deposited using the single ps pulse regime, with individual ps pulse fluence of 3.7×10^{-3}J/cm^2 and ns background fluence 3.7J/cm^2. λ=248nm.

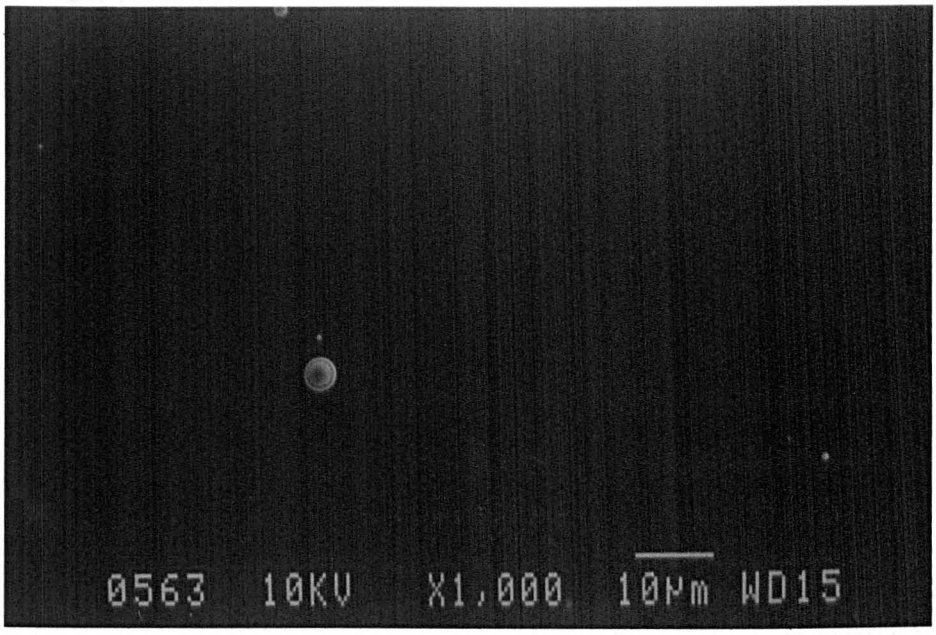

Figure 5.25 A 33nm nickel film deposited using 20ns pulse length, 6.9J/cm^2. λ=248nm.

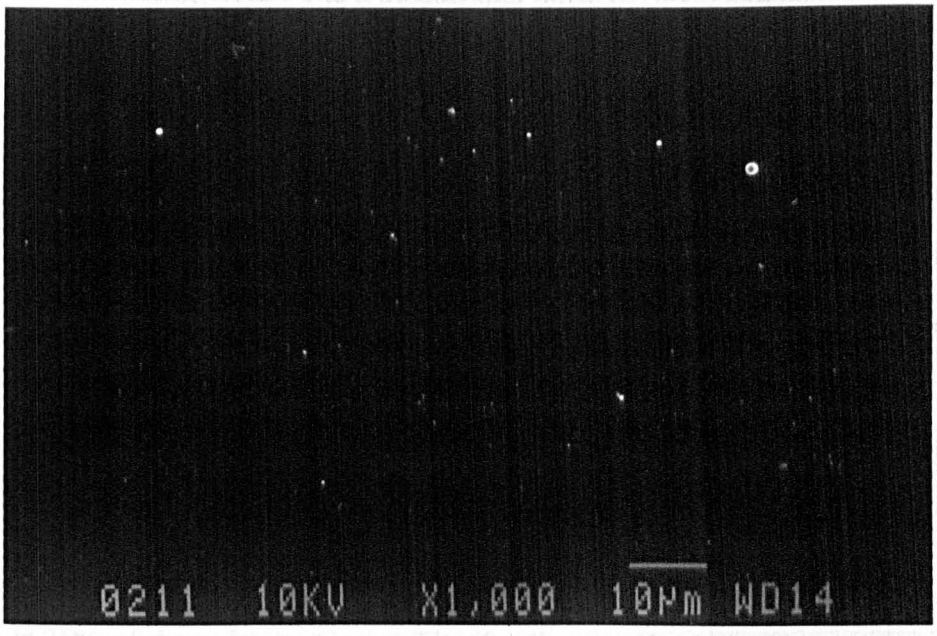

Figure 5.26 A 36nm nickel film deposited using the ps pulse train, with individual ps pulse fluence of 1.0×10^{-5}J/cm^2 and ns background fluence 0.01J/cm^2. λ=248nm.

This might also suggest that the number of pulses has an effect on the number of droplets seen on deposited films. For example we could say that a film deposited using the ps pulse train profile experiences roughly 16 times more pulses than a film deposited using the single ps pulse profile. However when comparing figure 5.20, a silver film deposited using the single ps profile, with figure 5.22, silver film deposited using the ps train profile one cannot say that the former figure shows fewer droplets than the latter, which would be expected if pulse number was a dominant feature of droplet production. A similar argument holds for the nickel films shown in figures 5.24 and 5.26. In addition we have already shown that the effect of the ps pulse is significant in producing droplets because of the vast increase in droplet numbers going from ns ablation to the single ps pulse profile, which is broadly the same number of pulses.

5.8.1 The picosecond ablation model

The single picosecond pulse envelope is described as a 25ns background radiation containing 0.023J and a picosecond pulse of 5ps containing 2.3×10^{-5}J. This gives energy densities of the separate parts of the pulse as up to a maximum of 3.9J/cm^2 and 0.004J/cm^2 respectively.

We have shown in section 5.6.3 the changes in target temperature associated with the background and individual ps pulses. The calculation shows conclusively that the heating due to the background energy is sufficient to melt the target and that the effects of heating due to the ps pulses are negligible. In the case of the single ps regime the target is definitely melted by the time the ps pulse arrives at the target. However in the case of the ps pulse train some of the ps pulses may arrive before the target has melted. Using equation 2.7 we estimate that the target melts within 6.5ns, which is 25% of the pulse envelope. Thus by the time the fifth pulse arrives the target surface is molten and therefore a substantial number of the ps pulses from the train reach the target whilst the surface is molten.

5.8.1.1 Ablation pressure

Having established that the target surface becomes molten before or whilst the ps pulses reach the target, we show that the effect of these shorter pulses on a molten surface is to eject material from the target surface as a result of the increased ablation pressure exerted on the molten surface by the expanding plasma. We follow the model presented by Phipps, Jr., *et al.* (1988), which gives an expression for the ablation pressure P_a (dyn/cm^2) as

$$P_a = 5.83\, A^{-1/3} \Psi^{2/3} I^{3/4} \left(\lambda \sqrt{\tau_p}\right)^{-1/4} \tag{5.4}$$

where

$$\Psi = \frac{A}{2\left[Z^2(Z+1)\right]^{1/3}}, \tag{5.5}$$

λ is in cm, A is the atomic number of the target, Z is the average degree of ionisation within the plume and I the power density at the target. The expression suggests that if the power density remains constant, the ablation pressure increases as the pulse length is reduced. In this case, the power densities for the ns and ps regimes are very different therefore we replace the power density with the flux density, where $I=F/\tau_p$, giving equation 5.4 in terms of the laser fluence at the target.

$$P_a = 5.83\, A^{-1/3} \Psi^{2/3} F^{3/4} \lambda^{-1/4} \tau_p^{-1/8} \tag{5.6}$$

where F in J/cm^2. If we take the maximum fluences available in the 25ns pulse as 10J/cm^2 and that for the 5ps pulse as 0.01J/cm^2 then the magnitude of the ratios of the fluence term to the pulse length term, i.e., $F^{3/4}\tau_p^{7/8}$, are 3.6×10^{10} and 2×10^{11} respectively. Thus the value for the ps pulse is an order of magnitude greater than for the ns pulse. This implies that the ablation pressure exerted by the plasma resulting from ps pulses is potentially greater than that for ns pulses.

Care must be taken when considering this approximation since Phipps, Jr., *et al.* (1988) consider that short pulse, long wavelength experiments are not described

by this model. The experimental data supporting this model includes pulse lengths down to 500ps, which are two orders of magnitude greater than the 5ps pulse, thus, it appears that we are just in the short pulse length regime. However, Phipps, Jr., *et al.* (1988) stress that the model presented is valid for $L_{th}>\alpha^{-1}$. For λ=248nm and τ_p=5ps we see that this condition is satisfied for silver, where L_{th}=41nm and α^{-1}=15nm, and just satisfied for nickel, where L_{th}=11nm and α^{-1}=9nm, and thus the model can be applied.

One can also show that the Phipps, Jr., *et al.* model predicts ablation depths at the target which are comparable to the value measured for nickel in section 5.7.4, i.e., 1.4nm/pulse. Phipps, Jr., *et al.* give the mass ablation, $\dot{m}$, as

$$\dot{m} = 2.66\times10^{-6} A^{-1/4}\Psi^{3/8}(I/\lambda)^{1/2}\tau_p^{-1/4}\text{g/cm}^2/\text{s} \qquad (5.7)$$

From which the ablation depth, x_a, at the target is given by

$$x_a = \frac{\dot{m}\tau_p}{\rho} \qquad (5.8)$$

where ρ is the density of the target material. For 0.01J/cm^2, the maximum fluence associated with the ps pulses, and τ_p=5×10^{-12}s, ablation depths per pulse of 0.82nm and 0.58nm were calculated for silver and nickel respectively. Although the calculated values are less than the measured value one must take into account that the measured value also incorporates ablation due to the ns background. However the calculated values show a reasonable estimation of ablation depth per pulse and further suggest that the ps regime presented in this thesis can be described using the Phipps, Jr., *et al.* model.

5.8.1.2 Droplet sizes in the picosecond pulse regime

The calculation of droplet sizes in the ps regime following the method set out in section 2.4.1.1 is summarised in Table 5.11. The calculation for ps pulses give small values. Many small droplets are seen on both the nickel and silver films deposited by the single ps pulses and the ps pulse train. There are in addition larger

droplets reminiscent of the droplets seen on the films deposited using ns pulses. These can be attributed to the ablation affects of the ns background. Despite this, the model presented in section 2.4.1.1 does not agree well with the droplet sizes seen on the films, in particular the silver films.

Sample (τ_p)	λ_D (μm)	D (μm)	$2r_{min}$ (μm)
Ni (ps)	0.035	0.0078	0.010
Ag (ps)	0.029	0.0064	0.008

Table 5.11 Characteristic surface damage wavelength, λ_D, for Ni and Ag and minimum droplet diameters, D and $2r_{min}$, (Bennett *et al.*, 1995; Kelly and Rothenberg, 1985a) for isolated 5ps pulses.

As for many of the models developed for PLAD, their extension to ps pulse lengths, and thus extremely high power densities on the target, is unsuccessful. Many models assume that the transfer of heat energy to the target is instantaneous which is no longer valid for ps pulse lengths. There are several problems facing the models used for calculating droplet sizes in the ps regime.

With the model presented by Kelly and Rothenberg (1985a) the thermal expansion of asperities (equation 2.12) is not valid in the ps regime. We have shown that the ps pulses do not contribute significantly to the heating of the target and thus to the thermal expansion of forming asperities upon which this model is based. Furthermore, in the case of an isolated ps pulse the time scale upon which thermal expansion takes place is much greater than the pulse length. Hence any model involving thermal expansion in the formation of droplets cannot describe the ps regime.

The model presented in section 2.4.1.1, which follows Bennett *et al.* (1985) also struggles to describe ablation by ps pulses. The model relies on calculating acceleration of the melt. However the ps pulses do not play a significant role in heating and thus melting of the target, therefore determining an acceleration for ps pulses is meaningless.

There are a wide range of models in the literature predicting the removal of material from the target surface, some of which are summarised by Chan and Mazumder (1987). The most satisfactory explanation for the evolution of droplets in the ps pulse configurations is the movement of molten material as a result of the plasma on the molten surface, for example Brailovsky *et al.* (1995). However any extension of this model must be carried out with caution, since ideally at shorter pulse lengths the problem of melting and therefore droplet production may be eradicated completely. Similar problems are faced when trying to extend other droplet models. From the point of view of the work presented here the ps profile ablation consists of contributions from the ns and ps pulse elements. To apply these both to droplet models is difficult. In addition, the assumptions made for ns ablation, i.e., that the heating of the target is instantaneous with respect to the pulse length, is not valid. At shorter pulse lengths the transfer of energy to the target as heat may not occur within the duration of the pulse. A further limitation of droplet models when extended to ps pulses is that they do not correctly predict the number of droplets that are formed.

Other work (Muller *et al.*, 1993) investigating the particulates on silicon and copper films deposited using 500fs pulses show that for silicon the films are smoother than those deposited using ns pulses. However for copper the film quality is described as consisting of many sub-micron granules when deposited with 500fs pulses and is smoother when deposited with ns pulses. This may indicate that for pulse lengths shorter than the electron-phonon relaxation time the ablation of metals is accompanied by particulates breaking off from the target, i.e. by exfoliation (Kelly and Miotello, 1994), rather than the expulsion of molten droplets as in the hydrodynamic model (Kelly and Rothenberg, 1985a).

5.8.1.3 Target features

Figures 5.27 and 5.28 show two silver targets ablated using single ps pulses and ns pulses respectively. It is clear that more turbulence occurred on the target irradiated with the ps pulse profile. This occurs because of the superposition of ps pulses onto a molten surface and is due to the increased ablation pressure predicted by Phipps, Jr., *et al.* (1988). Developing features on this target correspond to smaller droplets being emitted.

5.9 Uniform Laser Beam Profile

The results presented in this section were obtained from experiments performed at Exitech using the PLAD system described in section 4.4.3.

This section addresses whether a uniform beam profile results in the elimination of droplets in the PLAD process. Comments seen in the literature (Scheibe *et al.*, 1990) suggest that a uniform beam profile prevents hot spots arising on the target and thus reduces the possibility of instabilities in the laser-target interaction giving rise to droplets. The work presented in this thesis shows gold films that have been deposited with uniform and non-uniform beam profiles. Figures 5.29 and 5.30 show gold films deposited using the uniform and non-uniform profiles in figures 4.3 and 4.4 respectively. The production of these profiles is discussed in section 4.4.3. The films thickness are 14±2nm and 10±2nm, deposited with fluences of 8.7J/cm^2 and 3.6J/cm^2 respectively. Droplets are present on both films. The differences between the deposition conditions of these films makes it difficult to compare directly the droplet numbers on the films. For example figure 5.30 was deposited at a lower fluence which is generally considered to give fewer droplets in metals (Blank *et al.*, 1992). These films are shown however to draw attention to the fact that a uniform beam profile does not eliminate droplets in the PLAD process as suggested by some authors.

Despite the fact that droplets may not be completely eradicated from the PLAD process by a uniform beam profile, it may be true that a uniform profile is still desirable to achieve reproducible deposition conditions. There is a distinct difference

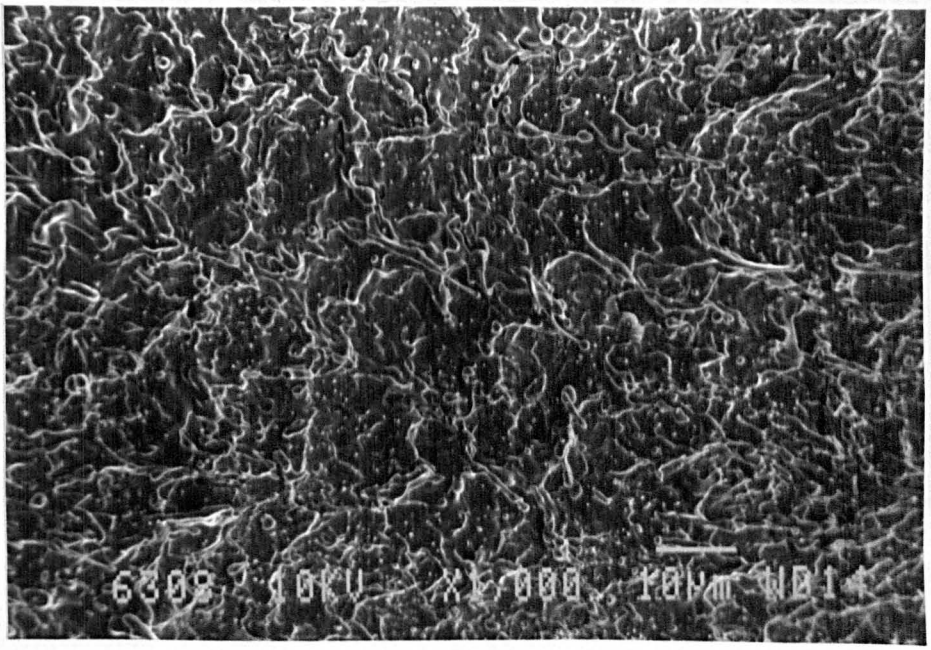

Figure 5.27 Damage caused on a silver bulk target by single ps pulses.

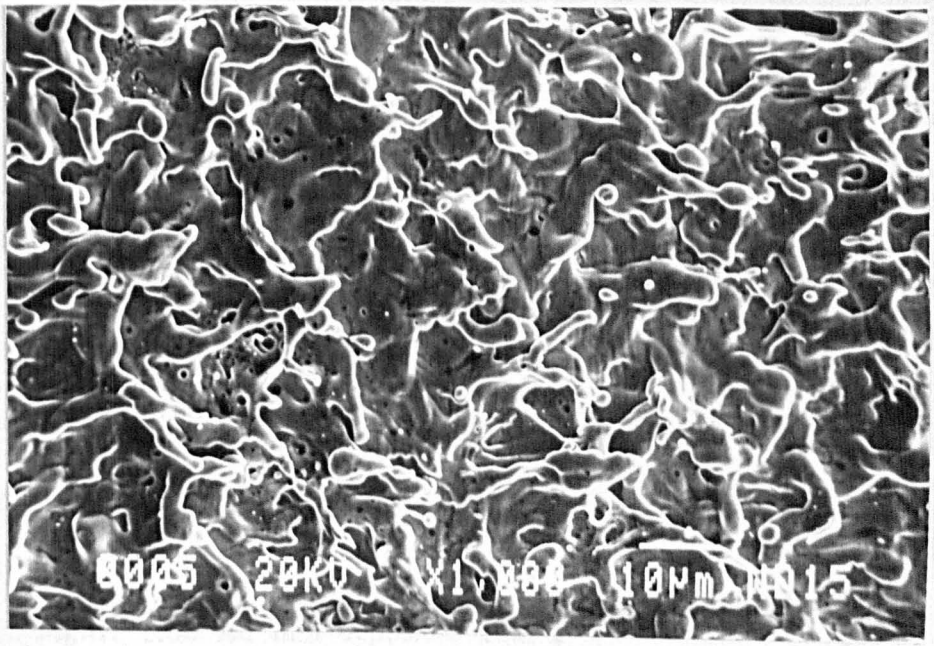

Figure 5.28 Damage caused on a silver bulk target by ns pulses.

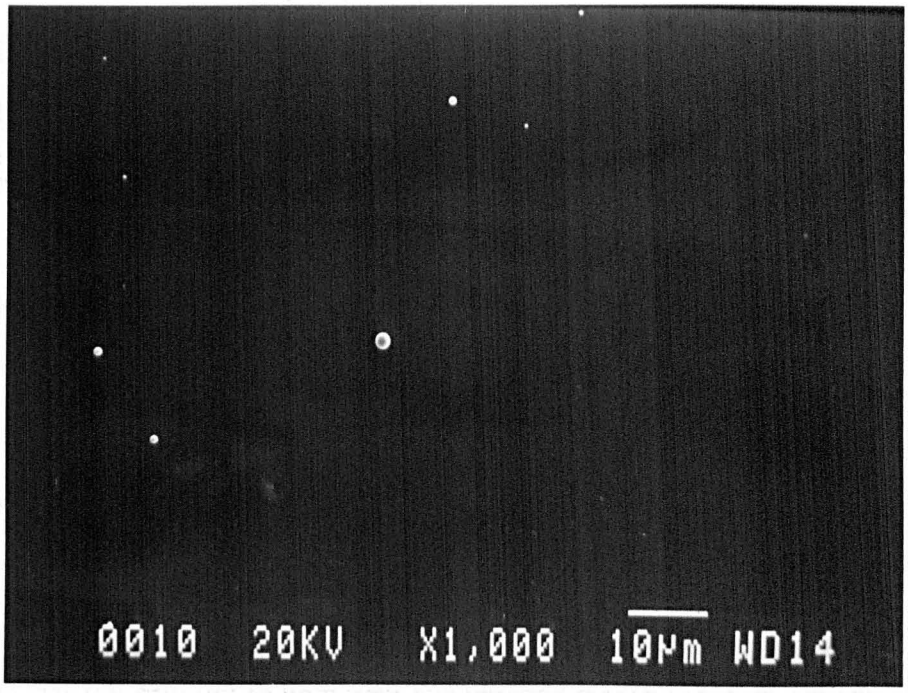

Figure 5.29 Au film deposited with a uniform beam profile at a fluence of 8.7J/cm^2 to a thickness of 14nm. λ=308nm, τ_p=20ns.

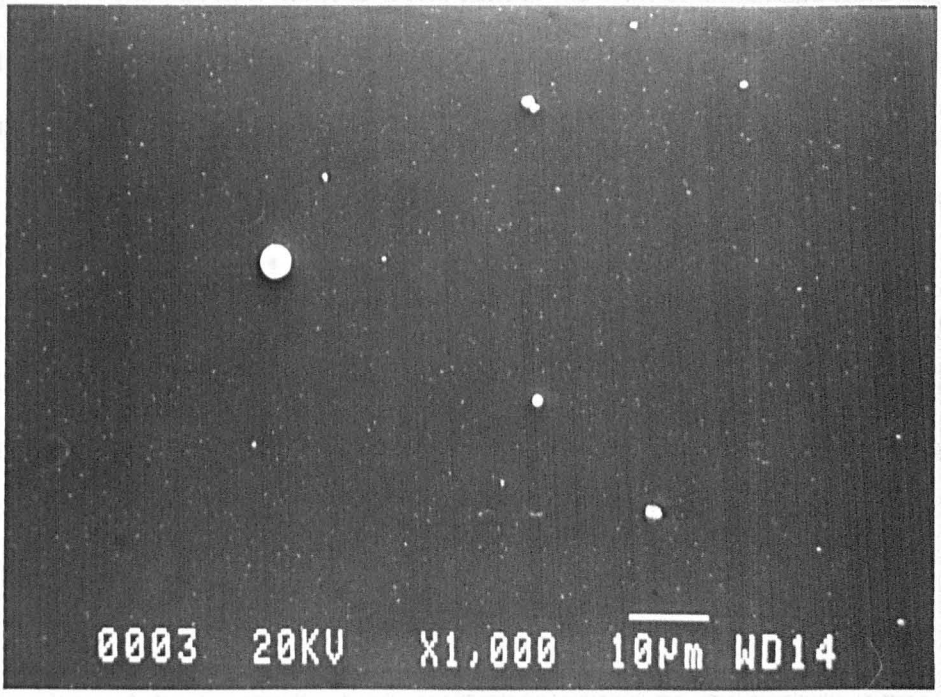

Figure 5.30 Au film deposited with a non-uniform beam profile at a fluence of 3.6J/cm^2 to a thickness of 10nm. λ=308nm, τ_p=20ns.

between the focused spot profile and the uniform beam profile. The latter involves imaging the beam at an aperture onto the target using optics to obtain a significant de-magnification to achieve a high enough energy density for ablation. This differs from a focused beam which has a Gaussian profile. On the target the energy tails of the Gaussian profile result in lower fluence edges of the spot.

5.9.1 Discussion

Documentation of the effects of using uniform energy density laser beam profiles in PLAD and the production of droplets is limited. Comments concerning the effects of a uniform beam are usually brief statements within the context of a larger subject and are not well substantiated. Private communication, PLAD Workshop (1997), has not brought to light well documented evidence for the advantages of a uniform beam profile. The origin of the comments pertaining to the advantages of uniform beam profiles for the reduction of droplets are shrouded in mystery despite the fact that the use of a uniform beam profile for reducing droplets is as well known to the PLAD community as translating the target, which in contrast is well documented (van de Riet *et al.*, 1993b).

To illustrate the problem we consider the comments made by Green *et al.* (1996).

'A homogenous uniform laser output is required for good-quality deposition work. Hot spots and deviations from uniformity should be avoided as much as possible. This is especially important when working with multicomponent deposition targets. Poor beam quality can result in non-stoichiometric films as well as undesirable droplet formation.'

These comments are followed by a discussion of the factors affecting beam uniformity and do not cite literature supporting claims for the improved film quality resulting from a uniform beam. This paragraph does however point to the reasoning behind using a uniform beam, the avoidance of hot spots. The presence of hot spots is likely to cause some areas of the target to ablate and heat more than others thus causing pressure gradients which disturb the molten surface (Brailovsky *et al.*, 1995).

In the case of metal ablation this would allow instabilities to form at the molten surface encouraging droplet emission. However Bennett *et al.* (1995) show that despite the use of a uniform beam ridge formations still develop on gold which lead to the production of droplets. Such droplet and ridge formations are evident on gold targets at near-threshold fluences in the absence of a plasma. The surface topography increases with the angle of incidence of the laser beam and with an increased number of laser pulses. The decision to use a uniform beam arises from the results presented by van de Riet *et al.* (1993b), which shows an increase in the number of droplets emitted at low fluences. Van de Riet *et al.* made use of a homogenous beam profile to avoid low fluence edges of the ablation spot which were shown to emit a greater volume percentage of droplets in FeSiGaRu and a range of other metals including aluminium, cobalt, iron and titanium. The increased number of droplets was due to the development of a columnar structure on the target surface. However in the case of copper and gold van de Riet *et al.* found that this type of roughening did not occur. By comparison the copper and gold targets were flat. Despite showing less roughening at the target it was found that copper emitted few droplets whilst gold emitted many. This is in agreement with Bennett *et al.* (1995), which shows wavelike structures occurring on gold targets that emit droplets even when using a uniform beam profile. Therefore it is not clear whether the use of a uniform beam profile does lead to the reduction of droplets numbers in metal deposition.

Scheibe *et al.* (1990) ascribe the lack of clusters present on diamond like carbon films to the uniform power distribution on the target. This is in comparison to Sato *et al.* (1987) who focus the laser beam directly onto the carbon target and thus report graphite particles on the diamond like carbon films.

The work presented here adds to the literature relating to beam uniformity. The results for gold are in agreement with Bennett *et al.* (1995) and van de Riet *et al.* (1993b) showing that droplet production in gold is not prevented by a uniform laser profile. It appears that in the case of metals, surface features develop irrespective of hot spots, although the elimination of hot spots may help to reduce numbers. This

suggests that the effect of the pressure exerted on the molten surface of the target by the developing plume contributes most widely to the development of instabilities at the target surface that give rise to droplets. Despite this it is recognised that a uniform beam profile provides increased reproducibility in the ablation process which is necessary for PLAD to be developed as a reliable, repeatable process, (Svendsen *et al.*, 1996).

5.10 Tape Target in PLAD

The results presented in this section were obtained from experiments performed at the Rutherford Appleton Laboratory using the PLAD system described in section 4.4.4.

In general a bulk target is used in PLAD. However some problems are associated with bulk targets in particular the roughening of the target leading to enhanced droplet emission. It has been demonstrated (van de Riet, 1993b) that the damage to the target surface increases with the number of pulses on that area. This problem has led many to translate the target either to reduce the number of shots on a particular area of the target or to ensure a new area is always exposed to the laser pulse.

Thus a method for introducing a clean target area for every laser pulse was suggested by Turcu (private communication). It was proposed that by using a tape target spooled throughout the ablation process that the number of droplets could be reduced. Thus a PLAD system was adapted to use a spooled copper tape as the target. In addition to having a new area available to each laser pulse, each pulse was also sufficient to punch a hole through the tape and thus expelled some material backwards through the hole. However the results show that molten material is still expelled from the tape in the direction of the substrate thus depositing droplets onto the films.

Figure 5.31 shows a copper film deposited using this method. The experiment was carried out using the ps pulse train temporal profile. The fluence of the individual ps pulses in the ps pulse train were 3.0×10^{-4}J/cm^2 and the fluence of the background

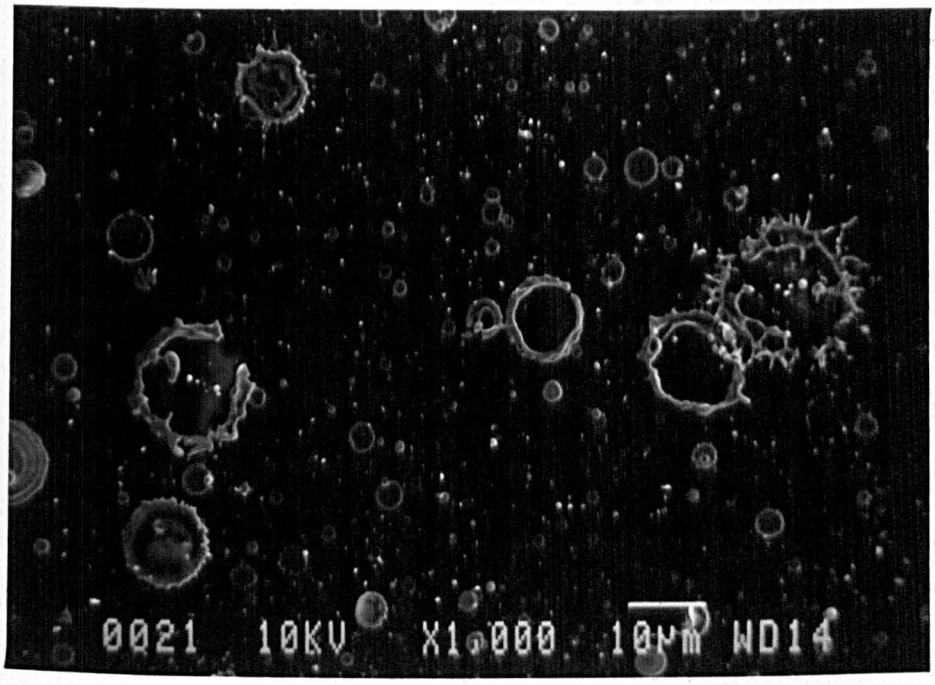

Figure 5.31 A 16nm copper film deposited using the tape target and ps pulse train temporal profile. The individual ps pulse fluence was 3.0×10^{-4}J/cm^2 and ns background fluence was 0.3J/cm^2. λ=248nm.

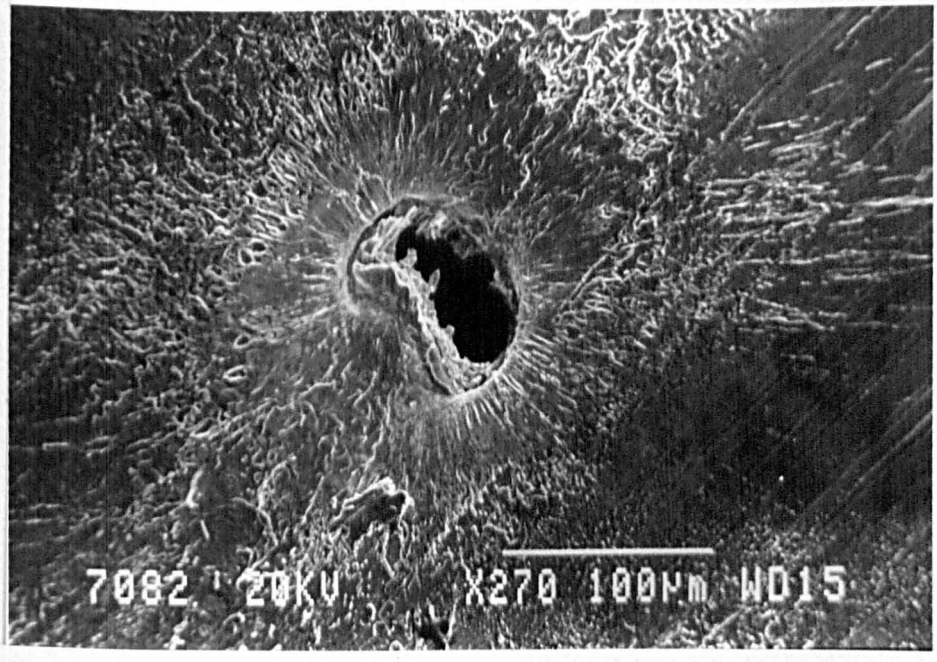

Figure 5.32 Damage to a 25µm Cu tape by a ps pulse train envelope.

$0.3J/cm^2$. The deposition rate was $0.625nm/cm^2$/pulse which is high compared to the ps pulse train on a bulk target. The film is covered in large droplets which are obviously molten in origin. Figure 5.32 shows the damaged region of the tape. There is evidence of melting as for the bulk material and that the removal of molten material is a violent process. As the tape is 25μm in thickness this is far greater than the dominant optical absorption length, α^{-1}~15nm for copper at 248nm and also the thermal diffusion length, L_{th}~1μm associated with the 25ns background in the ps pulse train. On the time scale for producing a hole in the tape target there is sufficient time for the surface to melt, for a plume to form and exert a pressure on the tape expelling molten material as for the bulk target. Bostanjoglo *et al.* (1994) show that the ejection of the melt is complete within 5ns which is relatively fast when compared with the 25ns pulse envelope.

5.11 Conclusions

In conclusion we see that the elimination of droplets in metal ablation is not achieved by using the ps pulse profile or by altering the laser wavelength. However careful choice of laser parameters and homogenous beam profile may go some way to reducing droplet numbers and increasing the control available for deposition via the PLAD technique.

Chapter 6

6 A Comparison of Metallic Multilayer Samples Deposited Using Different Deposition Methods.

6.1 Introduction

This chapter compares and contrasts a series of platinum (Pt) and nickel-iron permalloy (Py) multilayer systems deposited by two pulsed laser ablation deposition (PLAD) systems and RF sputtering. The three techniques are discussed in detail in sections 4.5.1, 4.5.2 and 4.5.3 respectively. The comparative study was an initiative arising from the present work and lead to a request to Andrei Zenkevich and co workers at the Moscow Engineering Physics Institute, Department of Solid State Physics for a supply of Pt/Py multilayer samples by their Nd:YAG PLAD system and to the Centre for Data Storage Materials group at the University of Coventry for the supply of a series of sputtered Pt/Py multilayer samples.

The layer structures are based on the approach by Parkin and Rabedeau (1996) which reports resistance changes per unit field of >10%/mT in multilayers of Py and Au. Such values make these materials potentially important for sensitive magnetoresistance devices. The use of transition metals, including the noble metals, in metallic multilayers is discussed by Parkin (1991) and here we have extended the investigation to use Pt. Parkin (1991) and related work are discussed in detail in section 1.1.3.

A series of multilayers were deposited by the three methods mentioned above. A selection of samples which show a range of magnetoresistance behaviour were analysed. Scanning electron microscopy (SEM) was used to characterise the surface finish of the samples, transmission electron microscopy (TEM) to examine the layer structure and x-ray reflectivity to study the uniformity of the layers and give an indication of the extent of roughness between them. In addition magnetisation curves for some of the samples were also measured.

6.2 Py/Pt Multilayer Samples

Table 6.1 shows the samples that are compared in this chapter. The intended growth structures are summarised for each specimen. The real structures of these samples are investigated throughout this chapter and are used to assess the suitability of the three deposition methods for metallic multilayer preparation. The sputtered samples were deposited without knowing the exact deposition rates and thus the precise thickness of the layers being deposited was unknown. The results presented later in this chapter suggest what the actual structures are. In addition the magnetoresistance (MR) measurements of these samples are presented. These results are correlated with the information from the characterisation of the multilayer structures.

Sample Name	Deposition Technique	Substrate	Growth Structure
m6	$PLAD_{mos}$	Si	(1.5nm Py/1.5nm Pt)$_{20}$
nm25	Sputtering	Glass	Ta/(Py/Pt)$_{20}$*
nm23	Sputtering	Glass	Ta/(Py/Pt)$_{20}$*
PyPt4	$PLAD_{war}$	Si	3nmPt/(3nm Py/0.5nm Pt)$_{20}$/ 3nm Py/4nm Pt
PyPt3	$PLAD_{war}$	Si	3nmPt/(3nm Py/1nm Pt)$_{20}$/ 3nm Py/4nm Pt
PyPt2	$PLAD_{war}$	Si	3nmPt/(3nm Py/1.5nm Pt)$_{20}$/ 3nm Py/4nm Pt

Table 6.1 Shows the intended structures of Py/Pt multilayer specimens compared in this chapter. The preparation of all the samples is summarised in section 4.5. The subscripts 'war' and 'mos' denote the different PLAD systems described in sections 4.5.1 and 4.5.2 respectively. * The thicknesses of these layers are unknown.

6.3 Multilayer Structure

In this section the multilayer structures of the samples listed in Table 6.1 are investigated. The aim is to see how the uniformity of samples compares for the different deposition techniques. The results obtained for the sample thicknesses using TEM and x-ray reflectivity are summarised in Table 6.2.

Errors in the film thickness determined from the x-ray reflectivity data is taken as the square root of the standard deviation of the range of values obtained for the interference fringe separations. The error in the bilayer thickness is based on the full width half maximum of the n=1 Bragg peak. The errors in the dimensions obtained from the TEM micrographs are given as the error in taking measurements from the micrographs.

Sample	nm25	nm23	m6	PyPt4	PyPt2
Film thickness from x-ray reflectivity (nm)	68±7	39±5	75±10	55±8	not known
Bilayer thickness from x-ray reflectivity (nm)	3.40±0.05	1.72±.0.02	3.0±0.1	not determined	not known
Thickness from TEM micrographs (nm)	48±4	not known	63±4	59±4	82±4
Bilayer thickness from TEM micrographs (nm)	2.4±0.2	not known	3.2±0.2	2.7±0.2	3.9±0.2

Table 6.2 A summary of the total and bilayer repeat thicknesses obtained for a series of samples using x-ray reflectivity and TEM micrographs.

6.3.1 X-ray reflectivity data

The reflectivity data presented in this section give information about the uniformity of the multilayer structures deposited. The data obtained from the samples investigated in this thesis show broadened peaks and a reduction in x-ray intensities. This makes precise determination of peak positions more difficult and increases the error in the thicknesses obtained. Thus the data are used to give an indication of the

total thickness and bilayer thickness of the multilayer samples. The data shown, support observations about the uniformity of the multilayers seen in micrographs in the next section. A comprehensive analysis of the diffusion and roughness of the multilayers in not performed since this requires detailed computer modelling. For the purposes of this work the variation in the x-ray intensities and peak broadening is sufficient to allow a qualitative comparison of samples to determine which deposition technique gives the most discrete layering. Furthermore the broadening of the peaks does not allow computer modelling to determine the layer and film dimensions more precisely. Details of the analysis of x-ray reflectivity data are given in section 4.7.

6.3.1.1 X-ray reflectivity of films multilayers deposited by RF sputtering at the University of Coventry

Figure 6.1 shows the x-ray reflectivity data for sample nm25. The feature of particular importance is the n=1 Bragg peak and the regular spacing of the interference fringes superimposed. These features are related to the bilayer periodicity of the multilayer and the total thickness of the sample respectively, as discussed in section 4.7. Thus using these features the layer thickness and total sample thickness for nm25 can be determined. The values obtained are summarised in Table 6.2. For example the n=1 Bragg peak position is θ=1.30±0.02°. Using equation 4.6 this gives a bilayer repeat distance of 3.40±0.05nm. From the deposition conditions it is expected that up to two thirds of this bilayer is Py, i.e., ~2.3nm Py and 1.1nm of Pt. This is in agreement with the MR results obtained in section 6.4.1 with the strongest AMR effect being present in sample nm25, which has the most Py in the sample. From the separation of the interference fringes, taken as $\delta\theta$=0.065°, the total layer thickness is calculated, using equation 4.6, as ~68nm. The error arising from the differences in the interference fringe separations is as much as 7nm. These values are in good agreement with 20 bilayer thicknesses being equal to the total thickness determined from the spectrum, figure 6.1, i.e., 20×3.4nm=68nm.

For sample nm23, figure 6.2, interference fringes related to the total thickness and the n=1 Bragg peak related to the bilayer repeat distance of the sample are

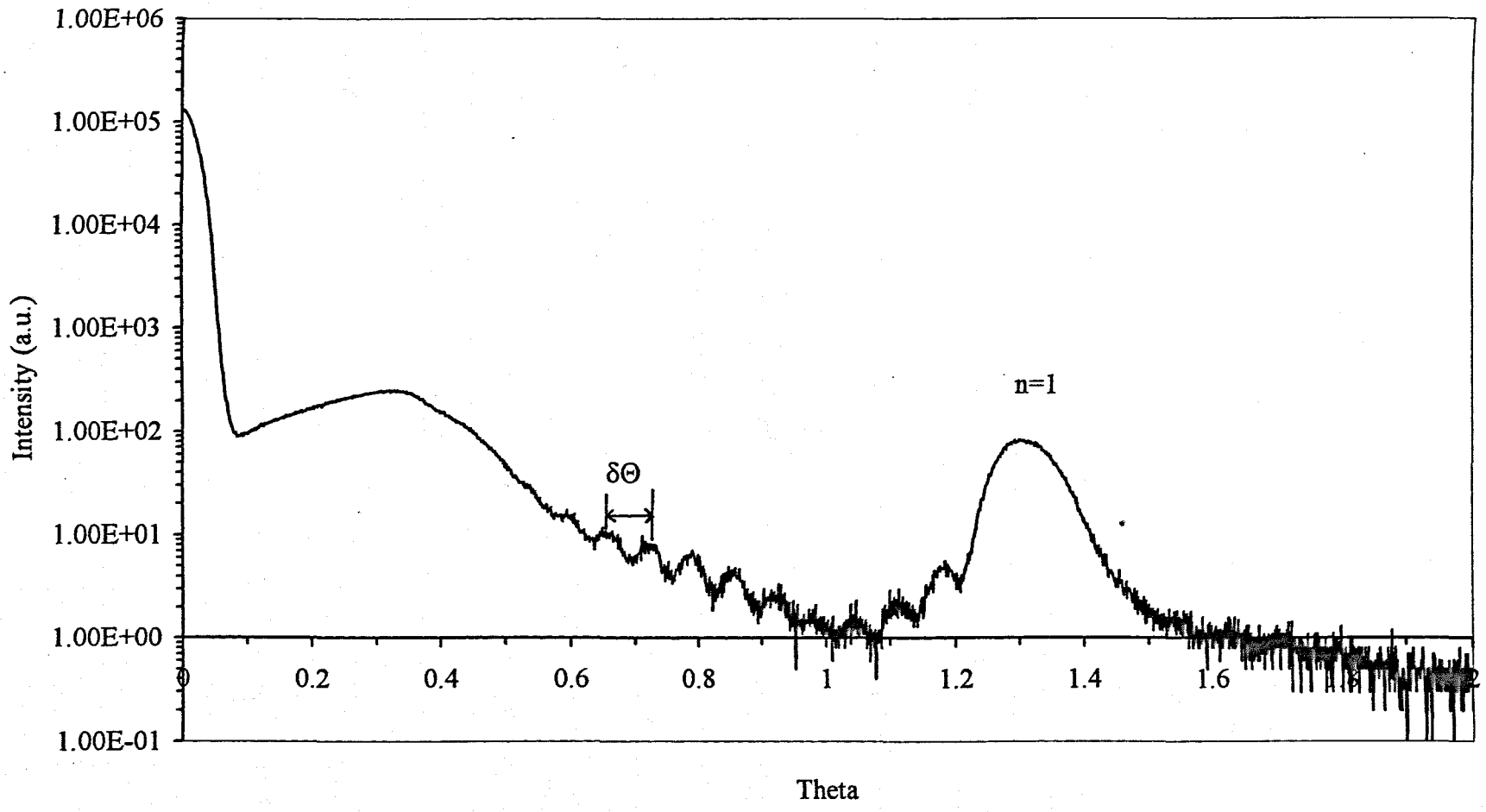

Figure 6.1 X-ray reflectivity data for sample nm25.

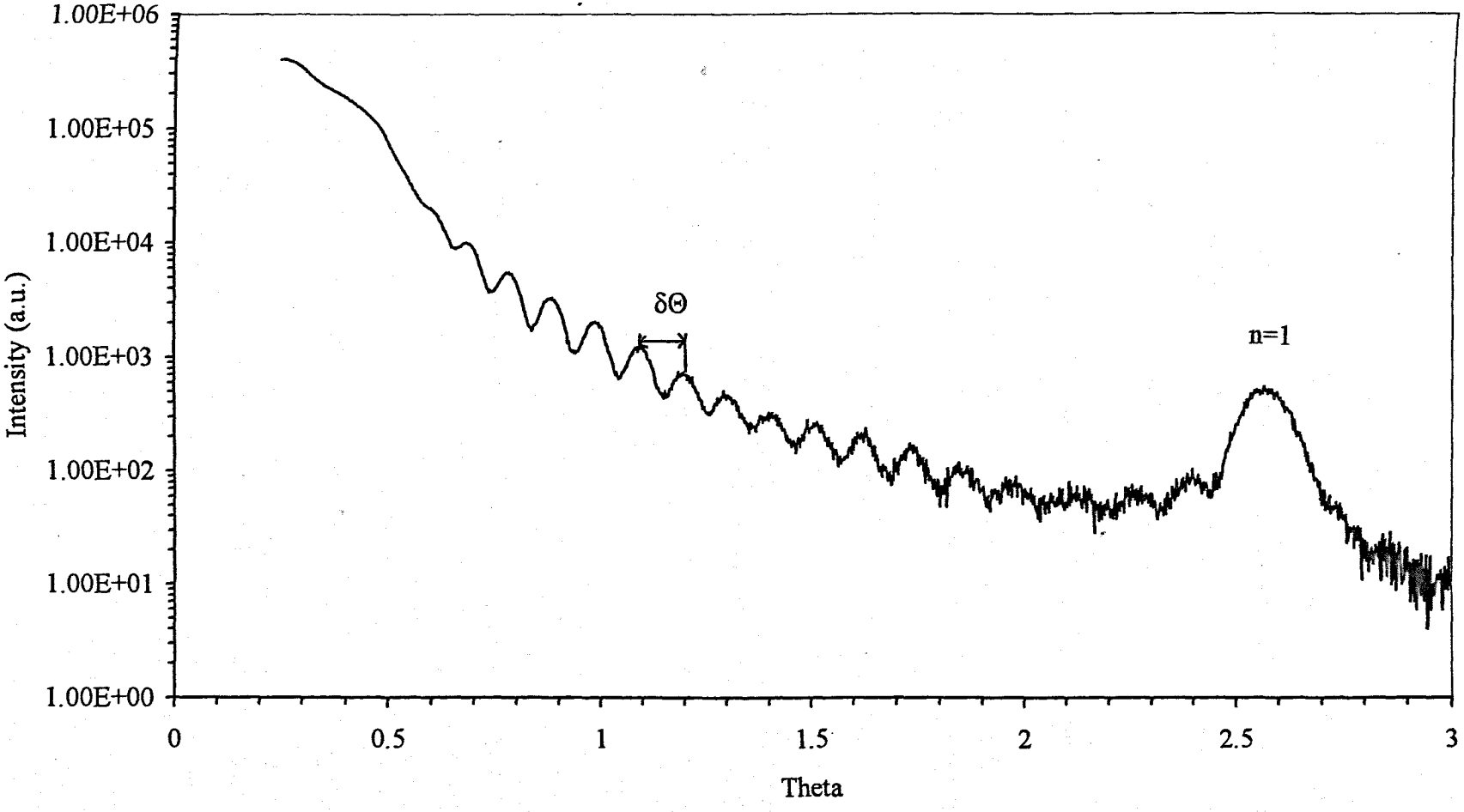

Figure 6.2 X-ray reflectivity data for sample nm23.

evident. Since the information at the beginning of the spectrum is not used for this analysis, the spectrum starts at θ=0.5°. Thus for the n=1 Bragg peak at θ=2.56±0.02° the repeat layer thickness is 1.72±0.02nm. A total sample thickness of 39±5nm was determined from the interference fringe separation of δθ=0.114°. From the determined bilayer thickness, the total thickness is estimated as 34.4nm. This value is within the errors of the total thickness of the sample determined from the interference fringe separation. We also see from Table 6.2 that a tantalum layer is deposited initially before the multilayer sample which will also account for some differences in the total thickness obtained via the two measurements.

6.3.1.2 X-ray reflectivity data for multilayers deposited by the PLAD system at the Moscow Institute of Engineering Physics

Figure 6.3 shows the x-ray reflectivity data for multilayer m6. The n=1 Bragg peak position for m6 is θ=1.45±0.03° giving a bilayer repeat distance of 3.0±0.1nm. This corresponds to the expected repeat layer thickness of 3.0nm, i.e., 1.5nm Py and 1.5nm Pt. From the separation of the interference fringes, taken as δθ=0.118°, the total layer thickness is calculated as 75±10nm. This is slightly higher than anticipated from the growth conditions and from twenty times the repeat distance determined from the Bragg peak positions, i.e., ~60nm. However the broadening decreases the precision in determining the Bragg peak position as well as indicating roughness in the sample (Kim *et al.*, 1997), thus we see that sample m6 does not have layers as well defined as sample nm25. In addition there is a 'hump' in the range θ=0.8°-1° before the n=1 Bragg peak. The shape of this feature is not reminiscent of a Bragg peak and is therefore not attributed as one. It suggests that there are other underlying features in the m6 multilayer.

6.3.1.3 X-ray reflectivity data for multilayers deposited by the PLAD system at the University of Warwick department of Physics

For sample PyPt4, figures 6.4(a) and 6.4(b), and sample PyPt2, figure 6.5, features of the x-ray data are less pronounced. This suggests that there is more roughness in these samples than the samples already presented. In figure 6.4(a) some

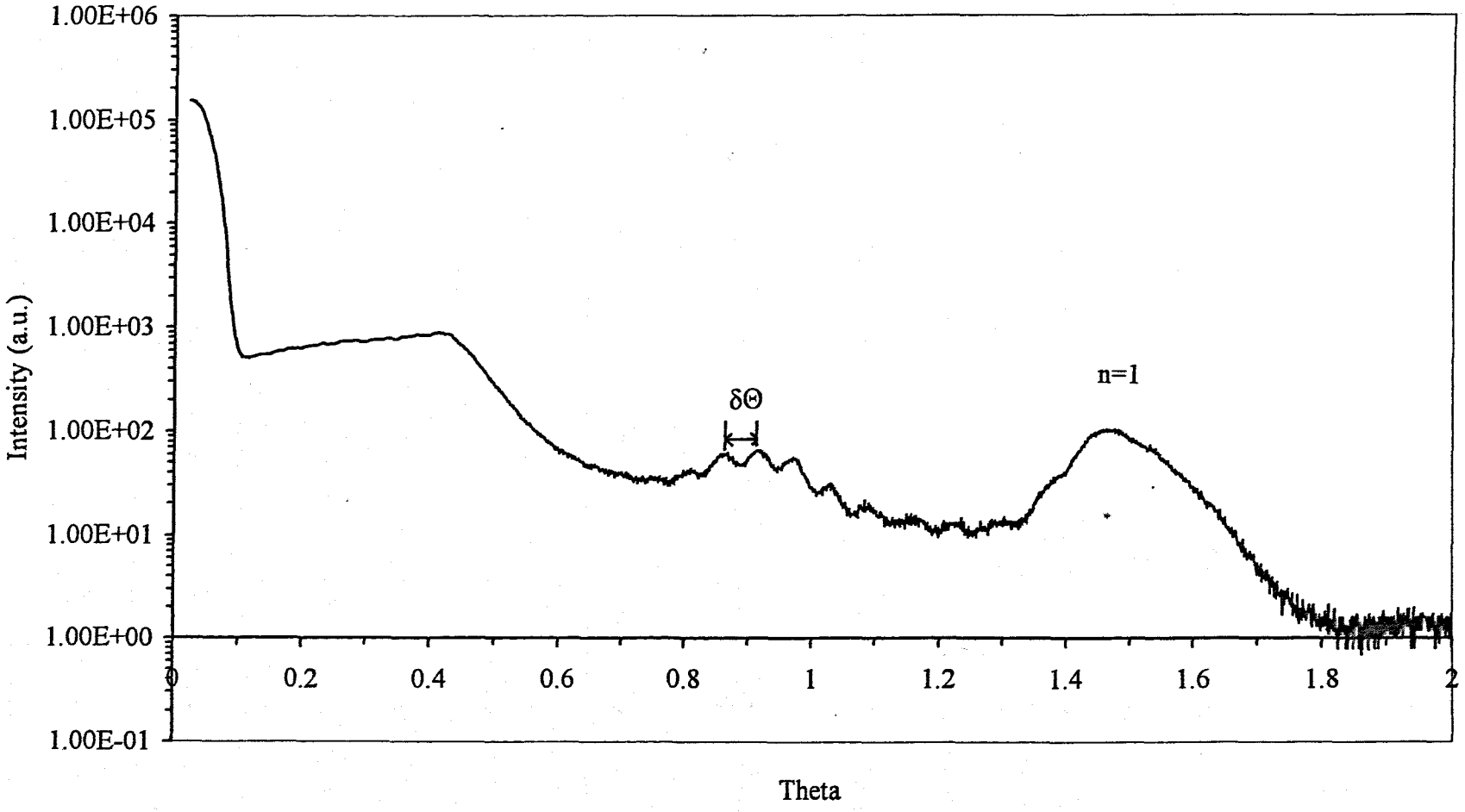

Figure 6.3 X-ray reflectivity data for sample m6.

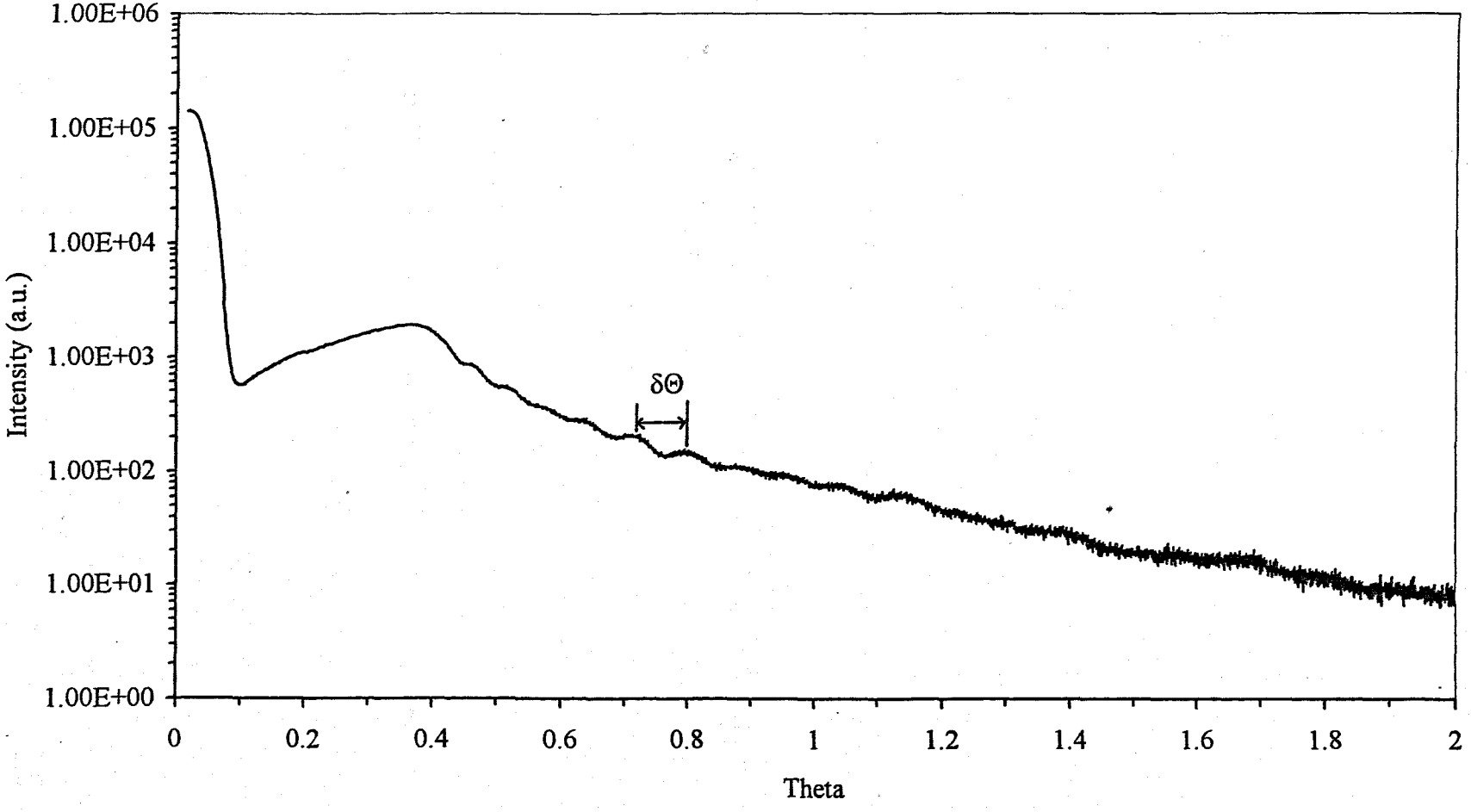

Figure 6.4(a) X-ray reflectivity data for sample PyPt4.

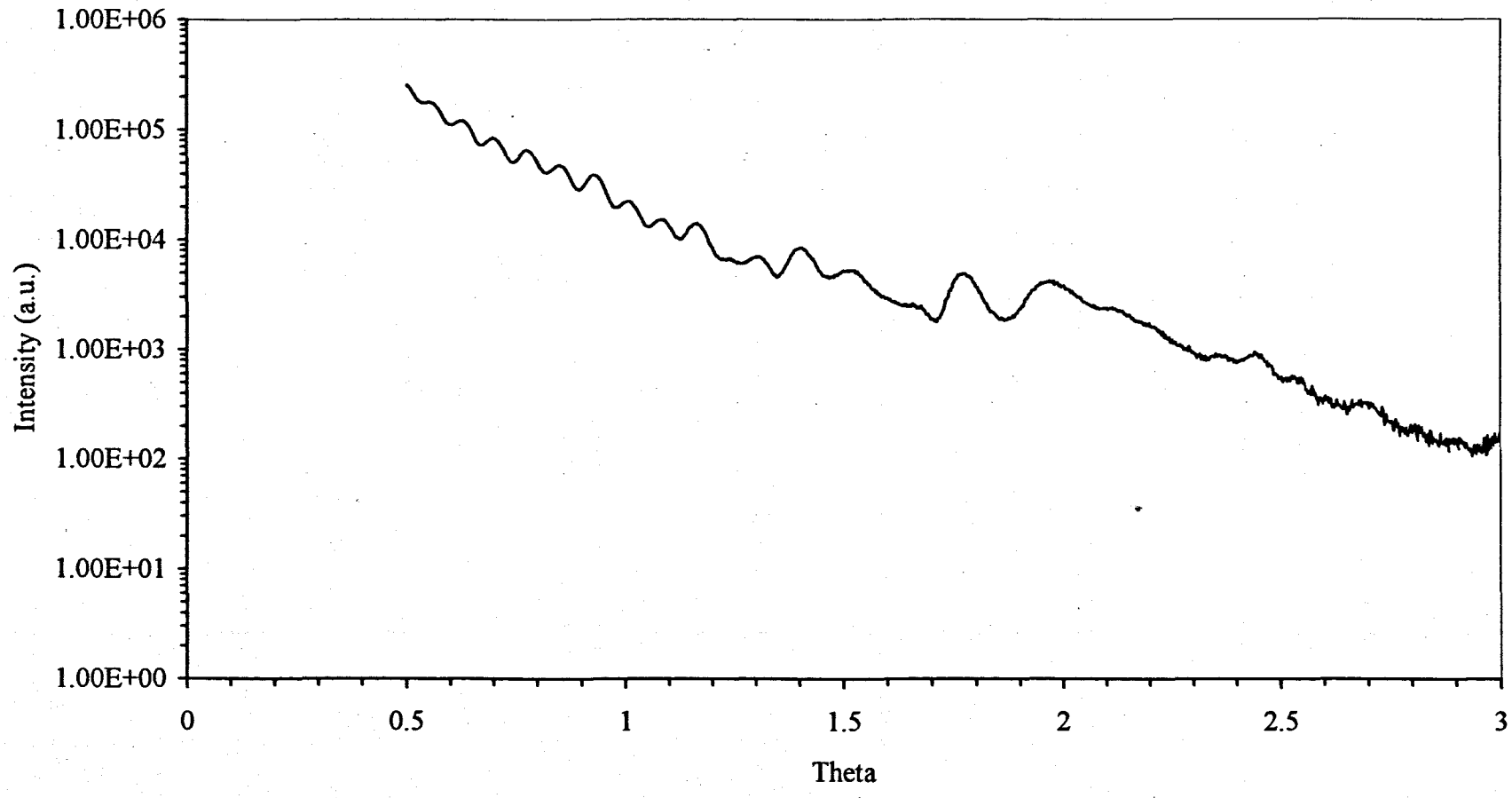

Figure 6.4(b) X-ray reflectivity data for sample PyPt4.

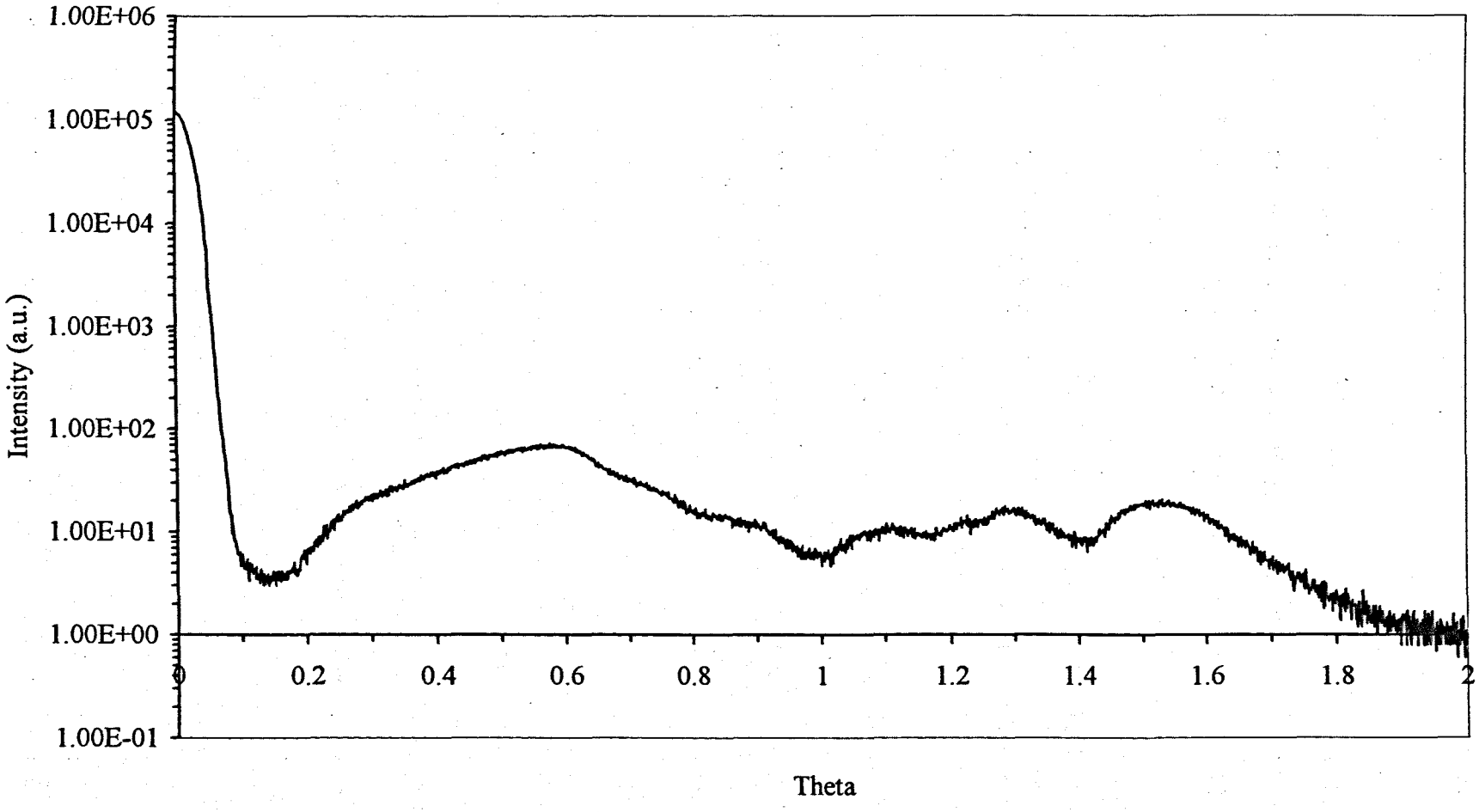

Figure 6.5 X-ray reflectivity data for sample PyPt2.

periodicity related to the sample thickness is present although the intensities of these features is severely reduced compared to the data discussed in preceding sections. No Bragg peak is present in the spectrum. This is somewhat unexpected since the growth conditions show that the periodicity is expected to be ~3.5nm, i.e., 3.0nm Py, 0.5nm Pt. For a bilayer thickness of 3.5nm a Bragg peak is expected at θ=1.26° which is not evident in figure 6.4(a). From this bilayer thickness we would expect a total sample thickness of ~73.5nm, however the total sample thickness from the interference fringes is ~55nm. This suggests that the deposition conditions for PyPt4 were not maintained and that the bilayer thickness is in fact less than 3.5nm and is closer to 2.7nm. From the TEM results in section 6.3.2 the total thickness could be a little as 50±10nm. From this the repeat layer thickness could be a low as 2.5±0.5nm. This would give an expected Bragg peak position of 1.8±0.5°. In figure 6.4 (b) reflectivity measurements were extended beyond θ=2° however a Bragg peak was still not evident. It appears that the lack of uniformity of the layering was sufficient to obscure the presence of a Bragg peak, which was expected at around 1.8°.

For sample PyPt2 we see that the x-ray reflectivity data in figure 6.5 shows little indication of uniformity, i.e., there are no interference fringes visible and no obvious Bragg Peaks. The lack of uniformity interferes with the regular reflectivity characteristics seen in the previous data. With the lack of interference fringes it is impossible to determine the total layer thickness. From the TEM data presented in the next section the thickness of the sample is estimated at 82±4nm which would give interference fringes of a separation of 0.054±0.003°. These are clearly not present in the spectrum. If 1/20th of the total thickness from TEM is used, i.e., 4.1nm, a Bragg peak would be present at θ=1.08°, which is also not seen. The non-uniformity in the bilayer spacing means that a clear Bragg peak position is not seen in the data. The expected deposition structure would have given an interference fringe separation of 0.044nm and the n=1 Bragg peak at 0.98°, which are not visible in the spectrum either.

6.3.1.4 Discussion of X-ray reflectivity data

Not only can x-ray reflectivity data be used to determine multilayer dimensions it also gives an indication of the roughness and uniformity of the layers. As discussed in section 4.7, roughness of the layers and the substrate causes the intensity of the x-ray reflectivity data to fall off more rapidly with increasing angle. The fringes can become indistinguishable if the roughness is as small as 3nm (Kim *et al.*, 1997). The effects of roughness are evident in figure 6.4(a), 6.5 and to some extent in figure 6.3. In particular we see that the intensity of the interference fringes in figure 6.4(a) falls off rapidly in comparison to the data obtained for samples nm25, nm23 and m6, figures 6.2, 6.1 and 6.3 respectively.

Thus the results of the x-ray reflectivity data suggest that the smoothest layers are deposited by sputtering, since the definition of the interference fringes is clearer than for the $PLAD_{war}$ samples in particular. In addition the broadening of the Bragg peak is less than that seen in sample m6 deposited by $PLAD_{mos}$. Sample PyPt2 in particular indicates that it is difficult to obtain good control in the $PLAD_{war}$ deposition process at these layer thicknesses, i.e., ~1-2nm. This is supported by the fall off in the intensity for sample PyPt4, which indicates roughness in the multilayer.

6.3.2 TEM micrographs of multilayer samples

The TEM micrographs shown in this section support the x-ray reflectivity data in section 6.3.1. These micrographs show a series of light and dark layers. The dark layers correspond to Pt and the lighter layers to the Py, related to density, as discussed in section 4.6.2. Thicknesses of the samples are estimated from TEM images. However the scale marker was found to be 15% longer than expected at 250kX magnification which gives thicknesses smaller than expected from the micrographs. The corrected values are given in Table 6.2, along with the associated bilayer thickness.

Figures 6.6 shows sample nm25. Two areas A and B are indicated showing that uniform layers are present in the sample, as expected from the x-ray reflectivity data. Problems were experienced in ion beam thinning samples deposited on glass.

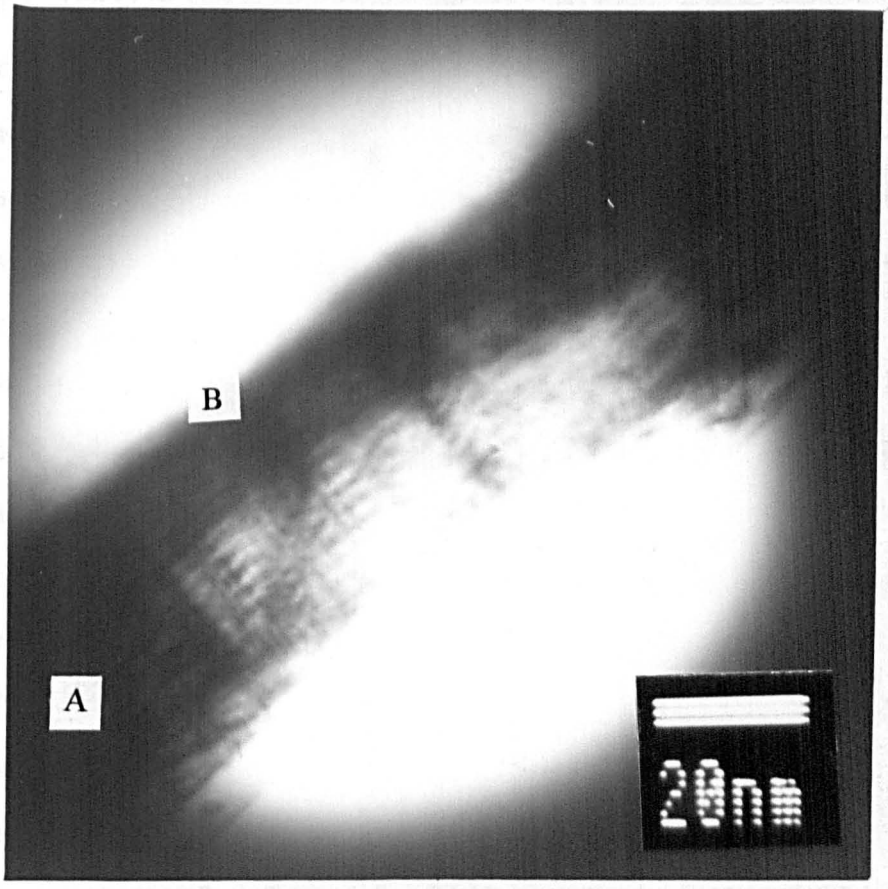

Figure 6.6 A TEM micrograph of sample nm25. Labels A and B indicate uniform areas of layering.

Graduated thin areas were difficult to achieve which meant that images were not easy to analyse by TEM. Disruption in the centre of the image is related to the thinning of the sample. The thickness shown works out to be 48±4nm, taking into account the 15% error due to the scale marker. This is less than the total thickness of 68±7nm determined from the n=1 Bragg peak. It appears that the area shown is not the total thickness of the multilayer and therefore the TEM value is less than anticipated. The difficulties with thinning samples deposited on glass meant that micrographs of sample nm23 were not obtained.

Figure 6.7 also shows the uniform layer structure of sample m6, which is indicated by the x-ray reflectivity data in figure 6.3. The sample thickness from the micrograph is determined as 63±4nm. The value obtained from the x-ray reflectivity data is 75±10nm. Therefore at the extremes of the error ranges these values are consistent.

The reflectivity data of samples PyPt4 and PyPt2, in figures 6.4(a), 6.4 (b) and 6.5 show less uniformity in their layering than samples nm25, nm23 and m6. This is confirmed in the TEM micrographs where the darker layers are of different thicknesses. For example in figure 6.8, a TEM micrograph of sample PyPt4, the lack of uniformity is particularly evident near the surface of the sample, where the layers are not clearly defined.

For sample PyPt4 the TEM micrograph and x-ray data correspond well giving a total film thickness in the region of 55-59nm. From this the bilayer thickness is estimated as 2.7nm. However the x-ray reflectivity data does not show the corresponding Bragg peak at θ=1.64°. Neither is there a Bragg peak at 1.26° corresponding to the bilayer thickness of 3.5nm given in Table 6.1. Therefore it is concluded that roughness in the sample over the area of the x-ray beam and the non-uniformity of the bilayer thicknesses are sufficient to obscure periodicity and mask the n=1 Bragg peak.

In figure 6.9(b) we see in the enlarged area that non-uniformity in the layering is visible. From the reflectivity data we might expect that the layering would appear

Figure 6.7 A TEM micrograph of sample m6 showing uniform layering.

Figure 6.8 A TEM micrograph of sample PyPt4. The non-uniformity of the layers is evident at the film surface.

(a)

(b)

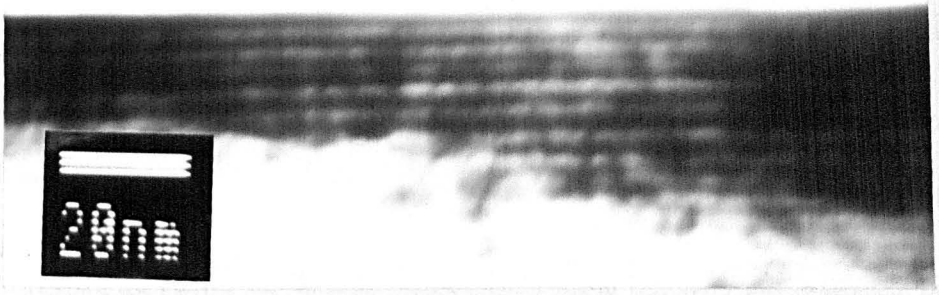

Figure 6.9 (a) A TEM micrograph of sample PyPt2. (b) An enlarged area clearly showing non-uniformity in the layers.

more distorted, however the sensitivity of the x-ray reflectivity may show details that are not clearly evident on the micrographs. One must remember that only small portions of the sample, approximately $5\times10^{-9}mm^2$, are analysed in TEM in comparison to the beam size in x-ray reflectivity of the order $10mm^2$. The x-ray reflectivity data from PyPt2 and PyPt4 suggest that roughness is present in the samples. To see roughness of the order of less than a nanometer requires magnifications close to the resolution of the microscope. Therefore it is difficult to ascertain details of the layer interfaces directly. In addition, ion beaming of the sample whilst thinning can lead to a mottled effect that may be mistaken as roughness in the TEM micrographs.

6.3.3 Surface characteristics of multilayer sample

Figures 6.10 and 6.11 show that droplets are present on the surfaces of samples m6 and PyPt4. Fewer droplets are present on m6 than PyPt4. SEM micrographs of sputtered multilayer samples show no droplet like features. The surface appears relatively smooth. This implies that some of the roughness evident in the x-ray reflectivity data for samples deposited using $PLAD_{war}$ and $PLAD_{mos}$ arise from droplets, with the most roughness being found in sample PyPt4 with the largest droplets, and less roughness arising in sample m6 which generally has smaller droplets.

The presence of droplets is detrimental for multilayer devices. With droplets being of the order of microns they are large enough to protrude through a number of layers, thus distorting the conduction through the magnetic and non-magnetic layering which gives rise to the GMR effect.

6.4 Magnetoresistance Measurements of Py/Pt Multilayers

In section 4.8 of the experimental procedures we see that to measure magnetoresistance (MR) the sample undergoes a cycle whereby the magnetic field is swept to a maximum value and back to zero and then again to maximum field where the cycle starts. This implies that virgin curves for these samples are not obtained. The maximum applied magnetic field is 0.88kA/m, which is equivalent to $\mu_0H=1.1T$.

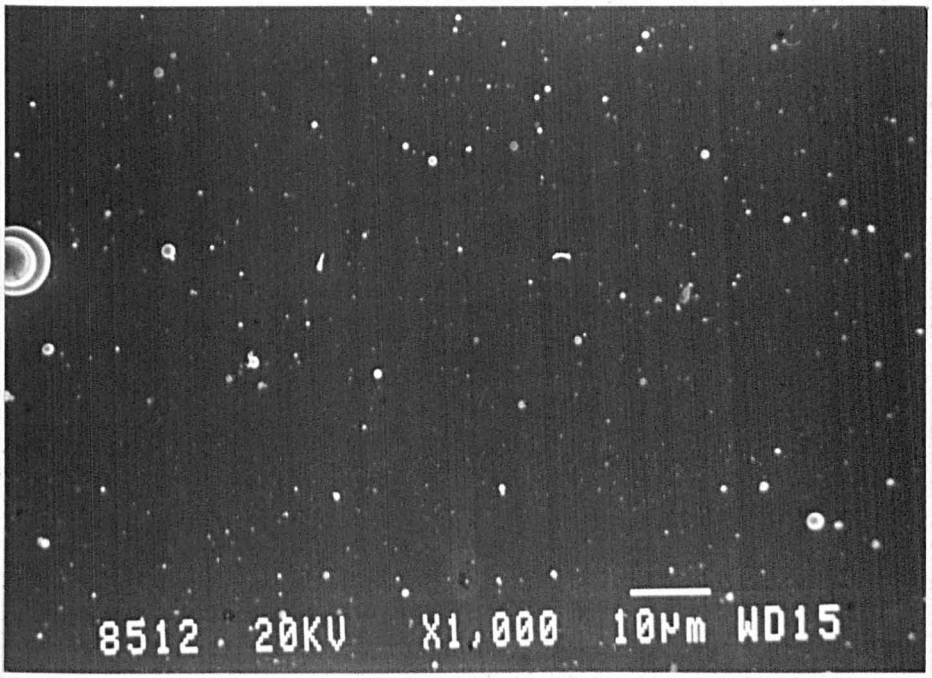

Figure 6.10 A SEM micrograph showing droplets on sample m6.

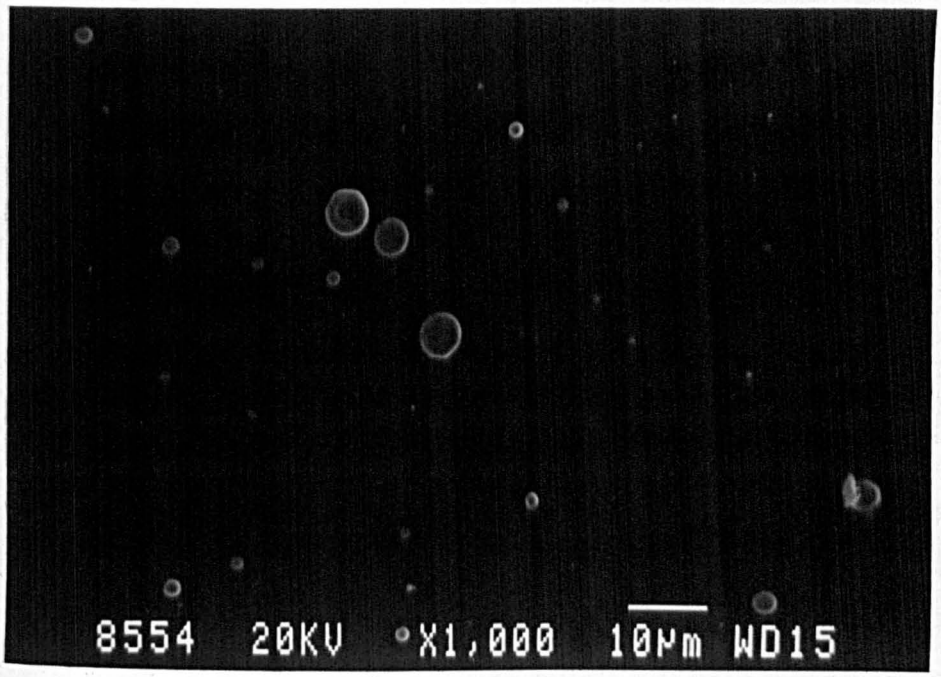

Figure 6.11 A SEM micrograph showing droplets on sample PyPt4.

The saturation of Py occurs at 1.08T (Landolt Bornstein, 1986). Thus the resistance at saturation is used to calculate the MR ratios.

For all the data there is some drift in the start and end point of the cycle. The drift amounts to 0.05% on the MR figure and is seen in both directions. This amounts to a change in the resistance of 0.005Ω in a film of 10Ω. This change is equivalent to a change in temperature of the sample of the order of 0.1°C, where the temperature coefficient of resistance is $6\times10^{-3}\Omega/K$ for Ni (Ohanian, 1994). Over the 10 minute period required to collect data the multilayer temperature might be heated by the 2mA current in the sample. However this source would only explain a drift upwards in the resistance. Changes in room temperature of several degrees, and hence in the sample by a fraction of this, could explain a drift downward in the data. In either direction the drift does not exceed 0.05% which is not sufficient to obscure or invalidate the results of the MR data.

The magnetoresistance measurements of the samples outlined in section 6.4 are shown in figures 6.12, 6.13, 6.16, 6.17 and 6.18. They are given as a percentage of the MR ratio from equation 3.1, which is the usual representation of this type of data.

6.4.1 MR of films deposited by RF sputtering

The magnetoresistance of samples nm25 and nm23[1] deposited by RF sputtering are shown in figures 6.12 and 6.13. The figures show the current parallel and orthogonal to the applied magnetic field, respectively. For sample nm25 we see that as the magnetic field increases the resistance of the sample decreases, except at very low applied magnetic field. The magnitude of this change in resistivity is ~0.13% irrespective of the geometry of the current and applied magnetic field. At low magnetic fields however there is a sharp variation in the resistance. The actual value of the resistance falls below the resistance of the sample at maximum field. These

---

[1]These samples were supplied by the Centre for Data Storage at the University of Coventry.

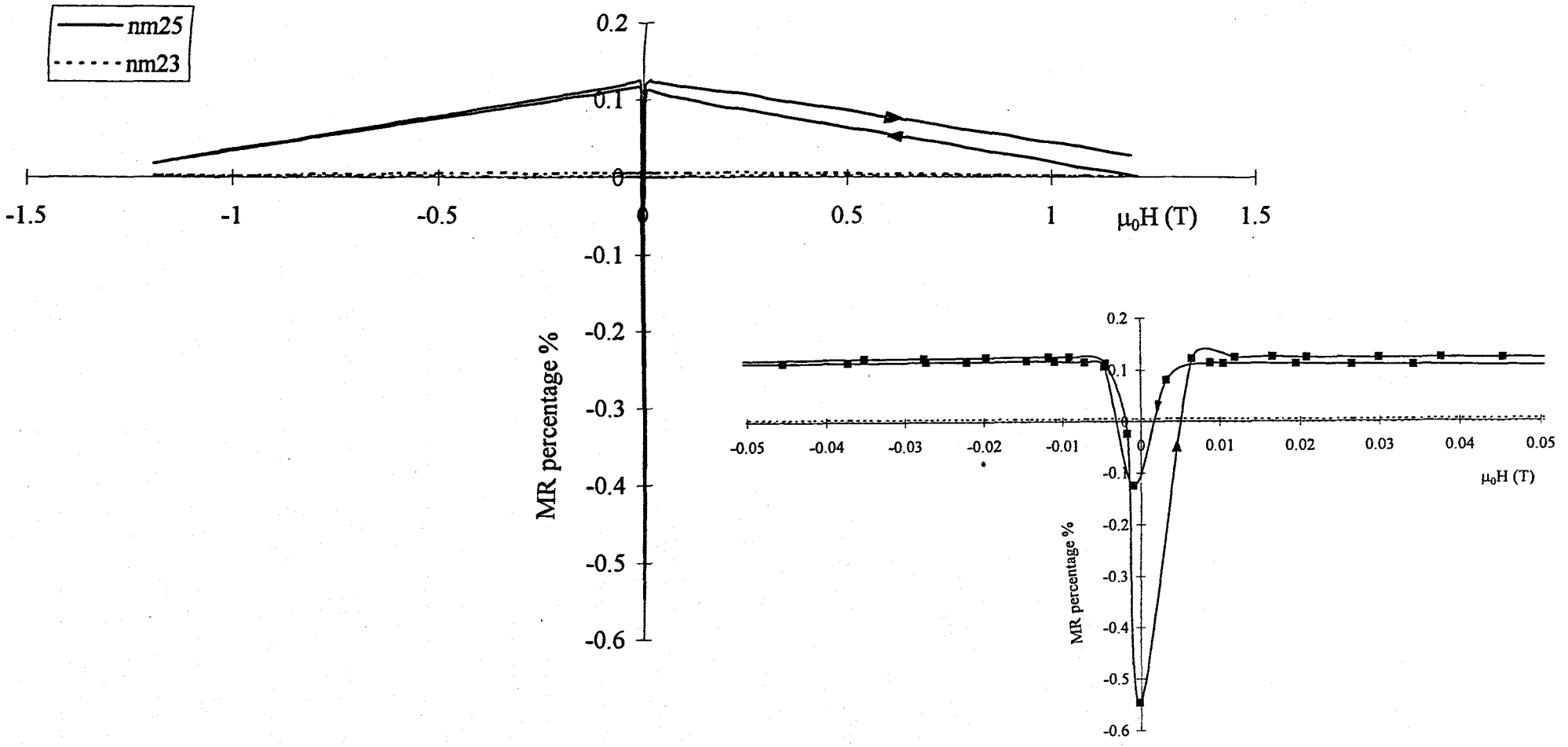

Figure 6.12 Magnetoresistance measurements of nm25 and nm23 with current parallel to field.

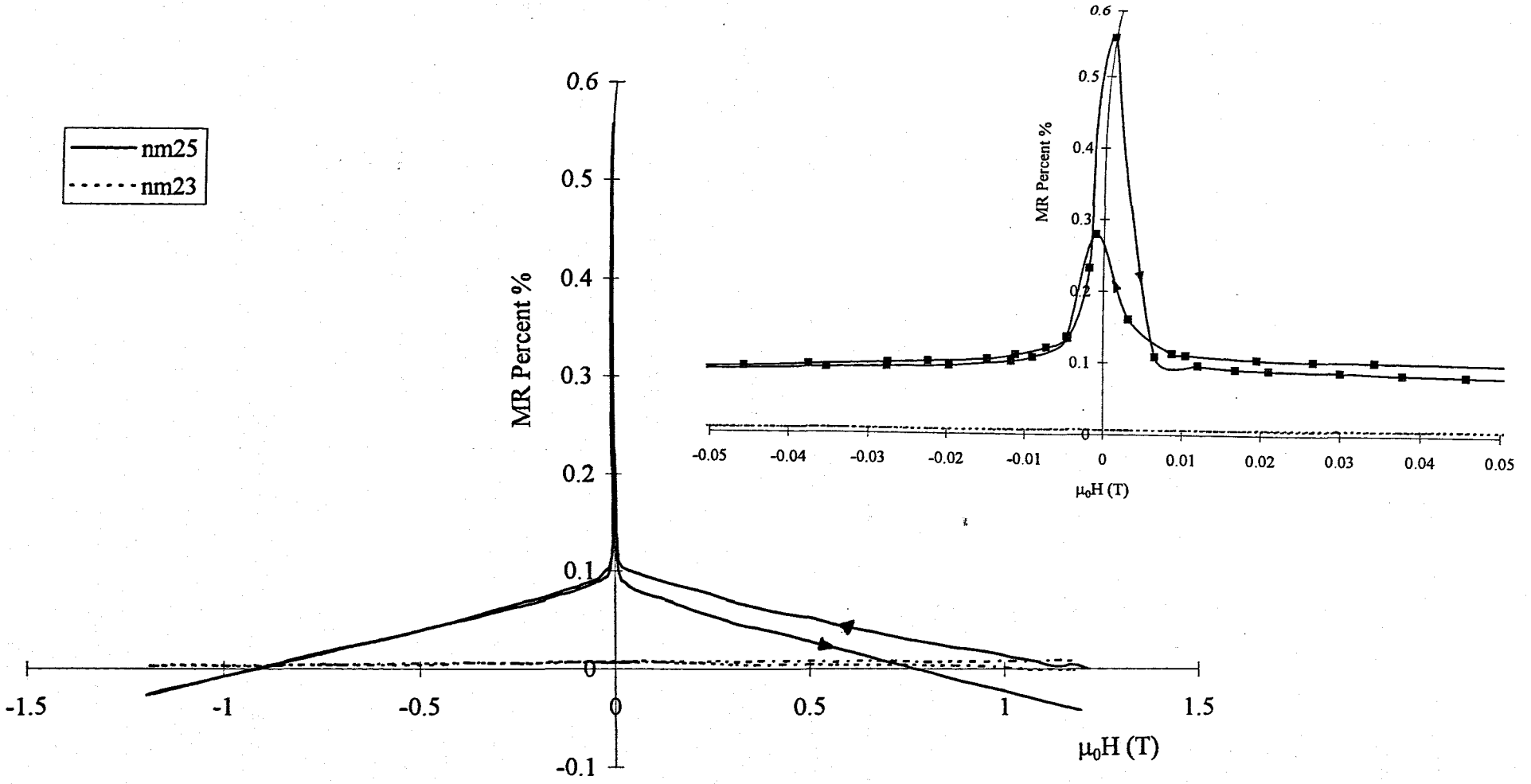

Figure 6.13 Magnetoresistance measurements for samples nm23 and nm25 with current perpendicular to magnetic field.

sharp resistance features occur in a field range of ±100Oe. This is indicative of the AMR effect as discussed by Smit (1951) who shows similar features below 50Oe. This change is ~0.5% when the current is perpendicular to the magnetic field and ~ -0.5% with the current parallel to the magnetic field. Hence the resistance of the sample at low field is dependent on the relationship of the current to applied magnetic field as for the AMR effect. Figures 6.12 and 6.13 do not strictly give the AMR percentage defined in equation 3.3, instead the individual geometries are shown separately using the MR percentage defined in equation 3.1. The AMR percentage is shown in figure 6.14. We see that the values of the AMR percentage are of the same order as the MR percentage. According to the schematic representation of the change in resistance of a ferromagnetic alloy in a magnetic field, figure 3.1, this sharp decrease in resistance is possible. It shows that at low field the resistance of the sample in the parallel geometry initially increases as the magnetic field is applied. This is then followed by a decrease in resistance at a slower rate at higher fields. This schematic representation can also account for the sharp decrease in the resistance of the sample seen in the transverse geometry. The resistances of sample nm25 in the parallel and perpendicular geometries are shown in figure 6.15 and show the same features as those discussed by Smit, figure 3.1. Thus we attribute these sharp features at low field to AMR. We also see that the variation at high field is similar in both geometries. This is expected since the change in resistance with magnetic field at high values is equal in both geometries.

One might expect the parallel measurements of MR to be slightly lower since the absolute resistance value of the sample at high field is higher than in the transverse geometry, thus the MR ratio would be smaller since the resistance at the maximum applied field is used in the calculation. This is borne out when comparing the parallel and perpendicular geometries for sample nm25, figures 6.12 and 6.13 respectively, where the MR percentage at around $\mu_0 H$=0.01T, i.e., before the sharp change in resistance, is slightly lower in the parallel geometry.

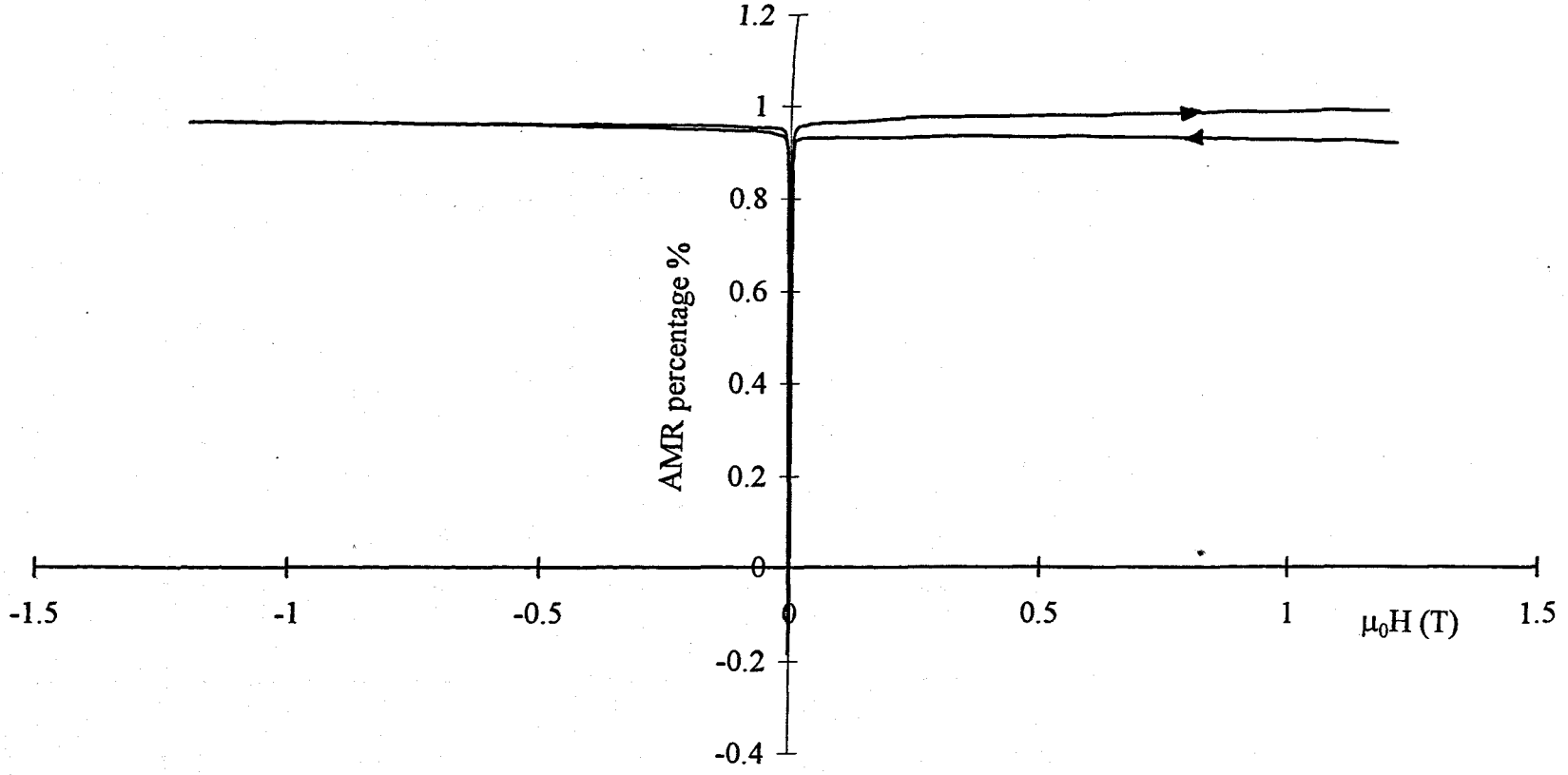

Figure 6.14 Anisotropic magnetoresistance measurements of sample nm25.

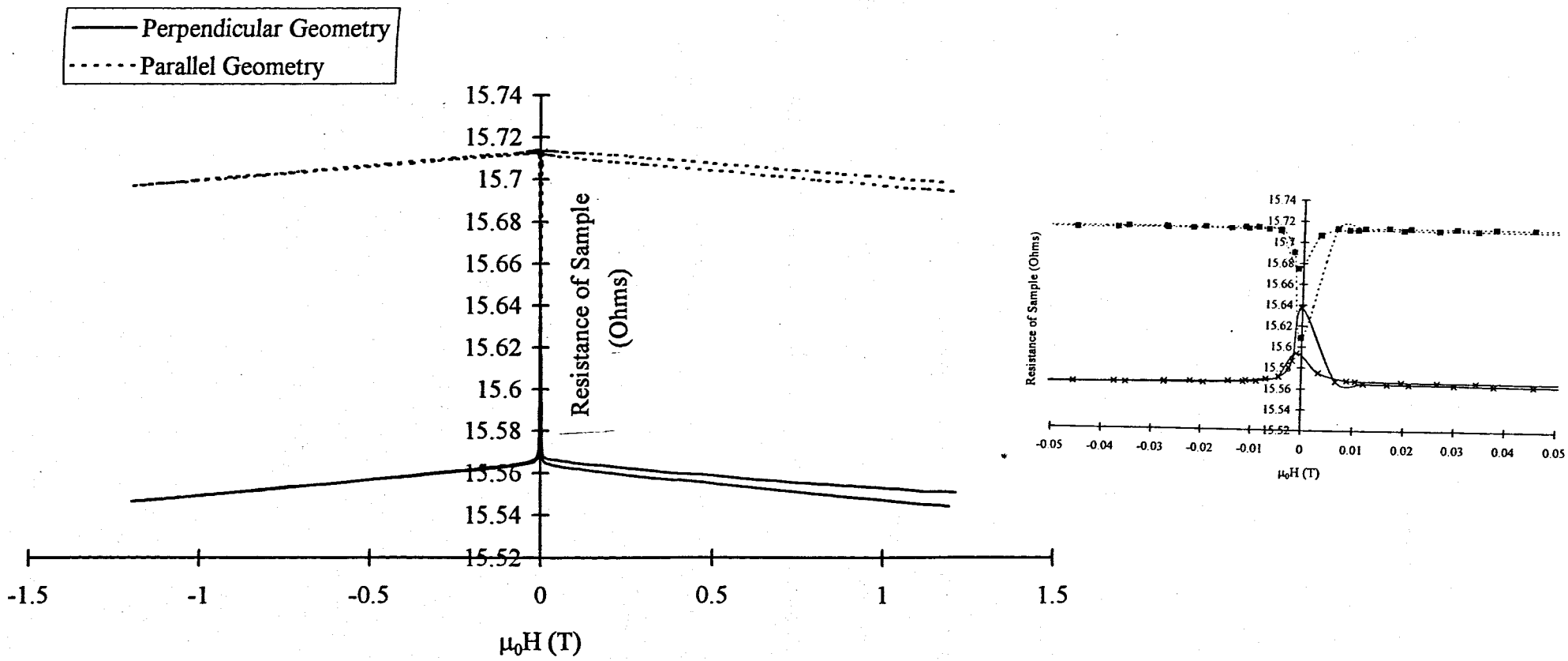

Figure 6.15 Resistance vs $\mu_0 H$ for sample nm25.

If we look on the enlarged scales for the parallel and perpendicular geometries we see that the effect at low field is more pronounced in the forward direction, i.e., with the field sweeping from maximum negative field through zero to maximum positive field than in the reverse sense, i.e., from maximum positive field to maximum negative field, for both geometries. If we look at the density of points around the zero field measurement we see that the peak is defined by the data point taken closest to zero field in both directions. Ideally a higher density of points is required to plot the behaviour around zero field more precisely. On might also expect hysteresis to be observed in the low field measurements as a result of the 'resistance' of magnetic domains to rotate by 180° once the applied magnetic field is reversed. At low fields there is some evidence that the peak changes in resistance do not coincide, however the data are not consistent. This is also due to the distribution of data points at low field which obscure the true magnetoresistance behaviour.

Sample nm23 shows no variation in resistance with applied magnetic field, thus there is no evidence of AMR or GMR. The lack of the AMR effect can be explained by the smaller amount of Py present in the sample compared to sample nm25. The sputtering conditions suggest that the ratio of Py:Pt is less for sample nm23 than sample nm25. The results from x-ray reflectivity for sample nm23, discussed in section 6.3.1.1, show that the bilayer thickness is 1.72±0.02nm. Of this measured bilayer thickness the deposition conditions suggest that the amount of Py is much less than the amount of Pt. In addition energy dispersive x-ray analysis used in scanning electron microscopy showed that Py accounted for only 20% of sample nm23. This is equivalent to 0.3nm layers of Py, hence we might expect that there is too little Py present to show a strong AMR response.

6.4.2 MR of films deposited by the PLAD system at the Moscow Institute of Engineering Physics

Some of the aspects of the MR behaviour in sample nm25 are seen in sample m6[2], figures 6.16 and 6.17. Over the entire applied magnetic field range a background change in the resistance of ~0.07% is observed in the parallel alignment and ~0.09% in the perpendicular alignment. This difference in the alignment is as expected and is observed in other samples. We see that for sample m6 in the parallel configuration, figure 6.16, that a data point was missed close to zero field in the reverse direction therefore giving the impression that the AMR effect does not occur. This again is due to the data point density around zero field.

6.4.3 MR of films deposited by the PLAD system at the University of Warwick Physics Department

For the samples deposited by PLAD using the Warwick system, a change in resistance is observed over the range of the applied magnetic field, figure 6.18. For sample PyPt4 the change is ~0.1% and for sample PyPt2 it is ~-0.02%. These samples show the effect of decreasing the Pt spacer layer thickness, thus increasing the percentage of Py in the multilayer sample. The intended ratio of Py:Pt layer thickness is 30:5 in PyPt4, 30:10 in PyPt3 and 30:15 in PyPt2. This reduction in the ratio is accompanied by a reduction in the effect of the magnetic field on the resistance of the samples. It could be considered that the OMR effect resulting from the increasing amount of Pt in the sample is working against the AMR effects from the Py. In these PLAD samples no sharp change in the resistance is observed at low field thus implying that the AMR effects are not as pronounced. Since the AMR effect is not so pronounced only the MR data in the parallel geometry is shown.

---

[2]This sample was supplied by the Moscow Engineering Physics Institute, Department of Solid State Physics.

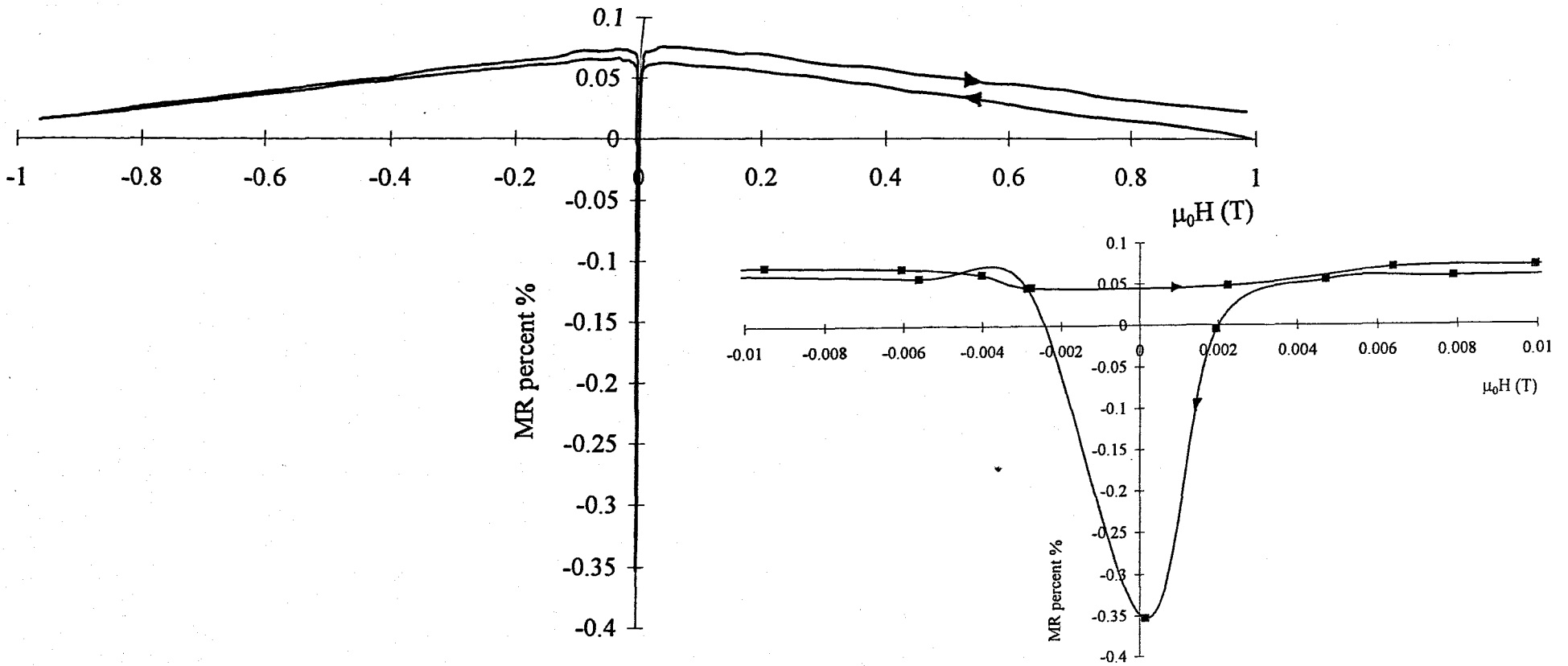

Figure 6.16 Magnetoresistance of multilayer sample m6 with current parallel to Field.

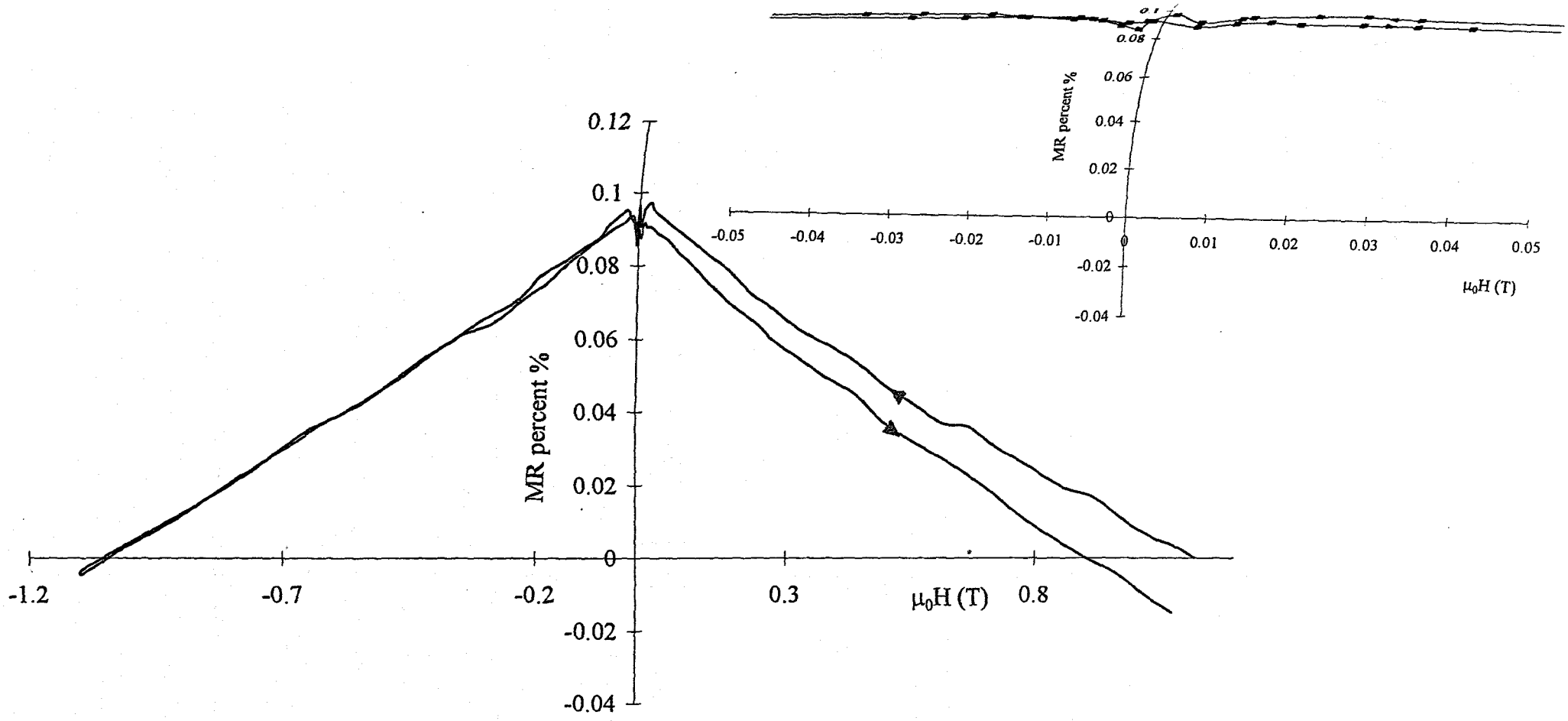

Figure 6.17 Magnetoresistance of multilayer sample m6 with current perpendicular to field.

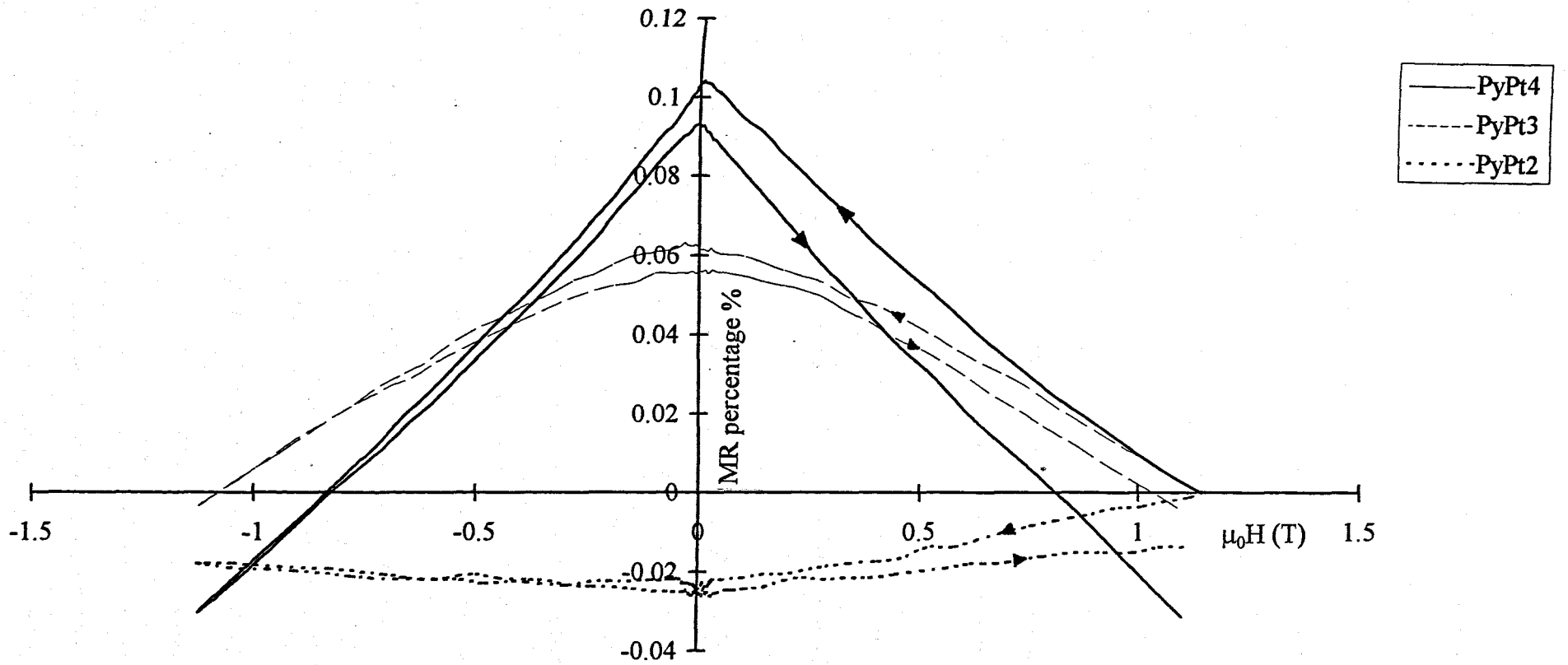

Figure 6.18 Magnetoresistance measurements of samples PyPt2, PyPt3 and PyPt4 with current parallel to field.

6.4.3.1 MR of a permalloy film

The MR of a permalloy film deposited using the Warwick system in shown in figure 6.19. We see that the change in resistivity is ~0.06%, except at low fields where the changes are ~0.02% in the parallel geometry and ~–0.01% in the perpendicular geometry. This gives actual MR values of ~0.085% and ~0.04% in the parallel and perpendicular geometries respectively. The characteristics are similar to those seen in the multilayer samples, although the changes in MR near zero field appear to be less than those measured in some of the multilayer samples. However if we note the field value at which the data point closest to zero field was taken, we can see that the true change in MR may be higher. For example, in figure 6.19 the data point closest to zero field is taken at 0.0045T with a corresponding change in MR of ~0.085%. If we compare this with the closest 'zero' points in figure 6.16 of 0.00015T, figure 6.13 of 0.0001T and figure 6.12 of -0.00015T we see that the corresponding changes in MR are greater than the values taken at slightly higher fields for the permalloy film. Thus if values slightly closer to zero field were presented for the permalloy film we would expect the MR values at zero field to be higher. Therefore we see that the distribution of the data points can account for some of the differences in the AMR effects seen throughout the multilayer samples. We can also conclude that the MR response of the multilayer samples is the same as that seen in the permalloy film and confirm that the AMR effect is the most pronounced in the MR measurements of most of the samples presented here.

6.4.4 Discussion of MR measurements

The magnetoresistance measurements of Py/Pt multilayers suggest that they are not suitable for sensitive MR device applications. We see that at high fields the resistance of the samples decreases with increasing field strength. Although this trend is seen in GMR it seems that the effects are not strong enough to favour this explanation over the AMR effects. The dependence of the resistivities on the current and applied magnetic field orientation points conclusively to AMR as the predominant effect. Thus, unlike Parker and Rabedeau (1996), GMR effects are not observed in

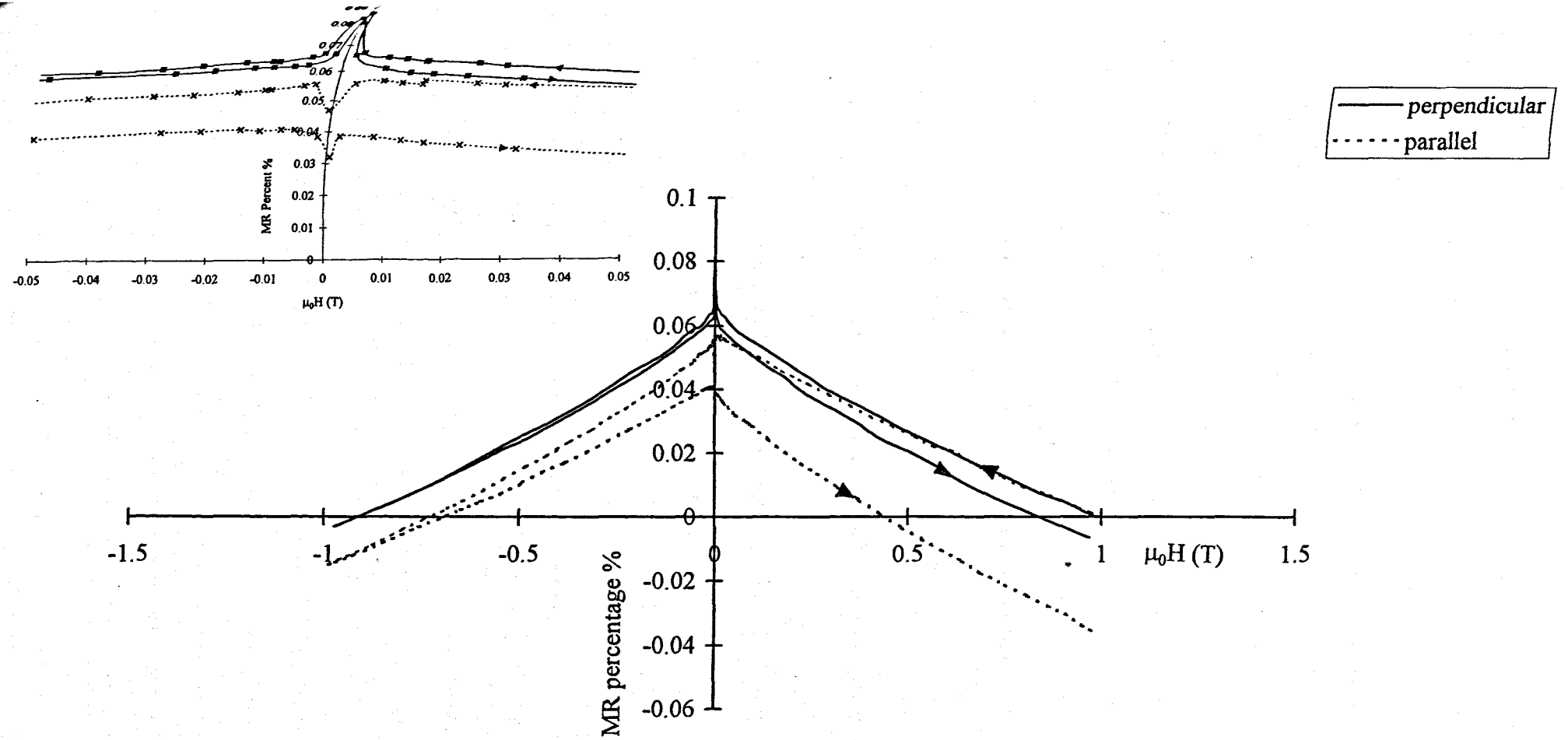

Figure 6.19 Magnetoresistance measurements of permalloy film with current perpendicular and parallel to the field.

multilayer samples of permalloy and platinum, despite the conclusions from Parkin (1991) that platinum would provide a weaker coupling between magnetic layers resulting in a more sensitive change in resistance at low fields. The change in resistance due to AMR observed in sample nm25 was of the order of 0.005%/Oe which is three orders of magnitude less than for the Pt/Au multilayers reported by Parkin and Rabedeau (1996). In addition to the samples discussed here the magnetoresistance of a wider variety of Py/Pt and Py/Au multilayers were also measured. The results were much the same as shown here with AMR effects dominating and no GMR being observed. However it was pointed out by Parker and Rabedeau (1996) that the Py/Au samples were very sensitive to deposition conditions and spacer layer thickness. Thus it is difficult to ascertain whether it is the sample structure or the difficulty in obtaining the correct deposition conditions that is the origin of the lack of GMR. The x-ray reflectivity and TEM results of the multilayer structures show that the best uniformity of layers is achieved via sputtering, followed by the $PLAD_{mos}$ technique. This suggests that where good structures were obtained the lack of GMR could be attributed to deposition conditions. In the case of the samples deposited using the $PLAD_{war}$ system significant difficulties arose in depositing uniform layers compounding the difficulties of depositing a successful GMR device.

6.5 Magnetisation Curves of Samples PyPt2, PyPt3 and PyPt4

The magnetoresistance of samples PyPt2, PyPt3 and PyPt4, in figure 6.18, does not show a marked change in value near zero field due to AMR as for the other samples. This suggests that these samples are not ferromagnetic, thus magnetisation curves were measured for these samples. The raw data, moment vs $\mu_0 H$, is shown in figure 6.20(a). Above ± 0.25T we see that there is a linear decrease in the moment. This is due to the diamagnetic response of the silicon substrate, the platinum in the multilayer sample and the rod holding the sample. However the diamagnetic response of the platinum in the sample can be ignored since the amount of platinum is negligible compared to the silicon substrate and the sample holder (see section 4.9).

Figure 6.20(a)

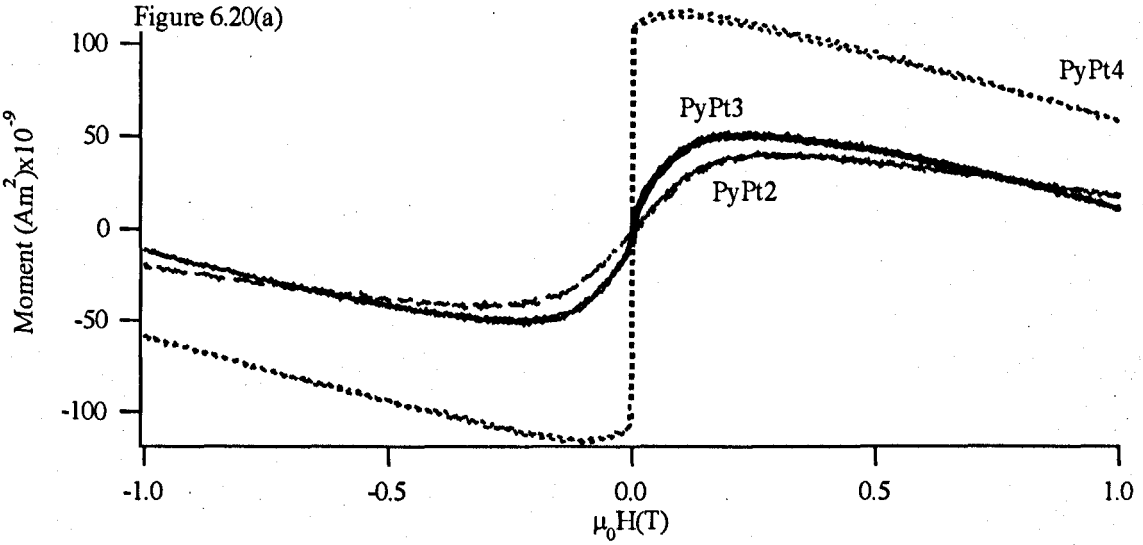

Figure 6.20(b)

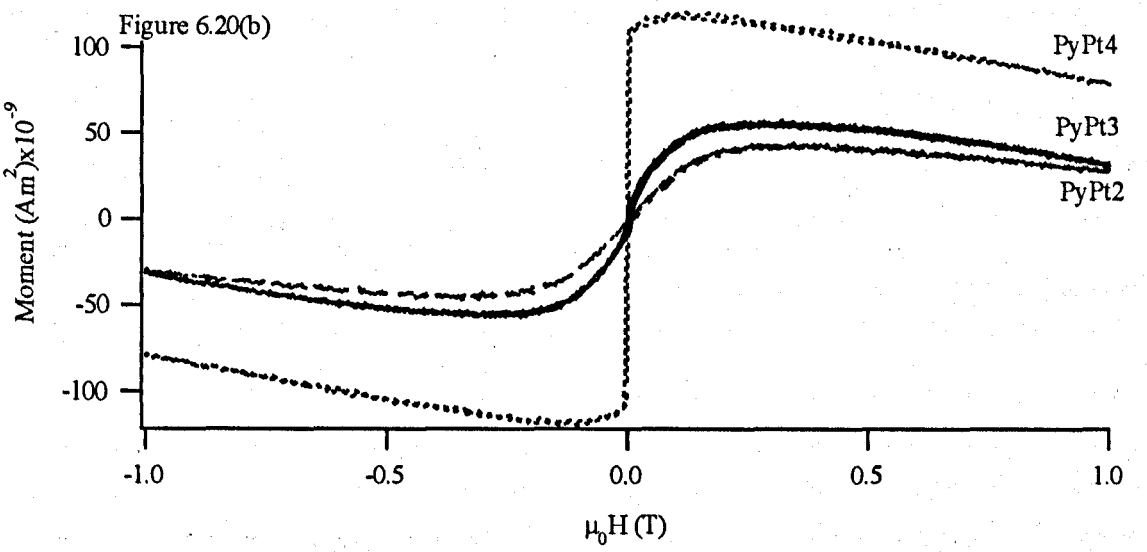

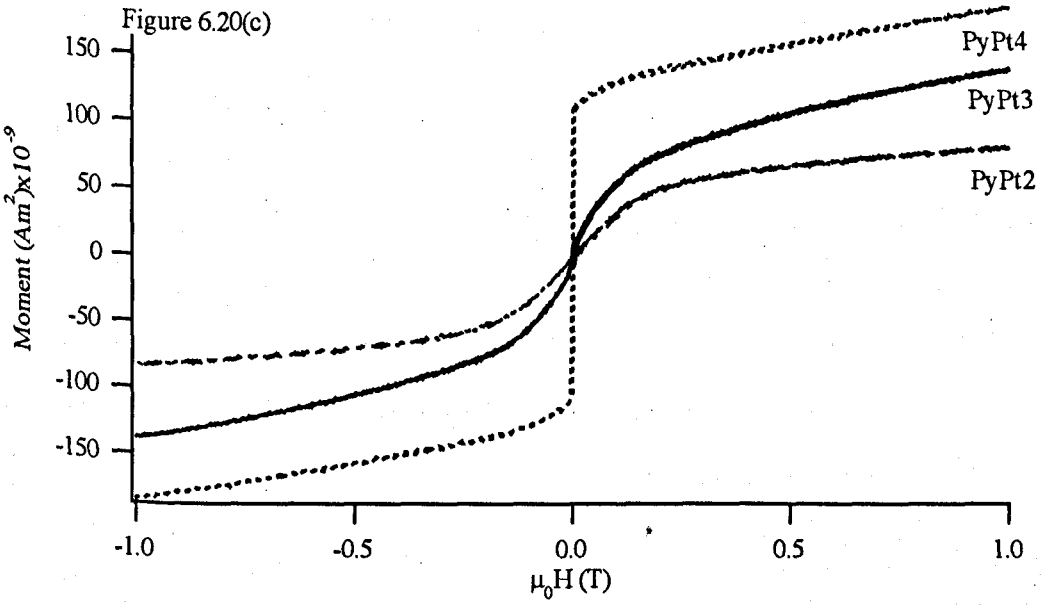

Figure 6.20 (a) shows the measured moments for samples PyPt2, PyPt3 and PyPt4. (b) shows the data corrected using the diamagnetic response measured for a piece of silicon. (c) shows the diamagnetic response calculated from equation 4.7.

Correcting for the diamagnetic response was not simple. Firstly the diamagnetic response of a piece of silicon was measured in the vsm. From the data the moment per silicon atom was determined. This value was used to remove the moment due to the silicon substrates of the samples. The results of this correction are shown in figure 6.20(b). We see that the correction was not sufficient since the moment still decreases above 0.25T. This is probably due to the response of the sample rod, which was not measured independently. Thus the moment per silicon atom determined from the vsm measurement is not correct.

Another correction was attempted by estimating the diamagnetic response of the silicon substrate using the expression in equation 4.7. The results of this correction are shown in figure 6.20(c). We see that the raw data are over corrected. The over correction is greater than the errors incurred in calculating the diamagnetic moment from the overall mass of the sample. Again this method does not take into account the diamagnetic response of the sample rod which is part of the raw data.

The difficulty in correcting these data is due to the small amount of ferromagnetic material present in the sample. In many cases the diamagnetic response of the sample rod is negligible compared to the size of the sample under investigation. In view of these difficulties the data were corrected by fitting a line above 0.25T. From this fit the slope was subtracted from the raw data. The corrected values for moment were then converted to magnetisation. These corrected results are presented in figure 6.21 which shows the volume magnetisation calculated for samples PyPt2, PyPt3 and PyPt4. The shapes of these magnetisation curves suggest that these samples are in fact ferromagnetic. There are however some discrepancies between the saturation magnetisation values seen in Figure 6.21 and reported bulk saturation magnetisation values. Crangle and Hallam (1963) show that the average moment per alloy atom of $Ni_{0.8}Fe_{0.2}$ is $1.08\mu_B$. Table 6.3 summarises the saturation magnetisation values determined from figure 6.magnetisation and the equivalent saturation magnetisation determined using the Crangle and Hallam (1963) value.

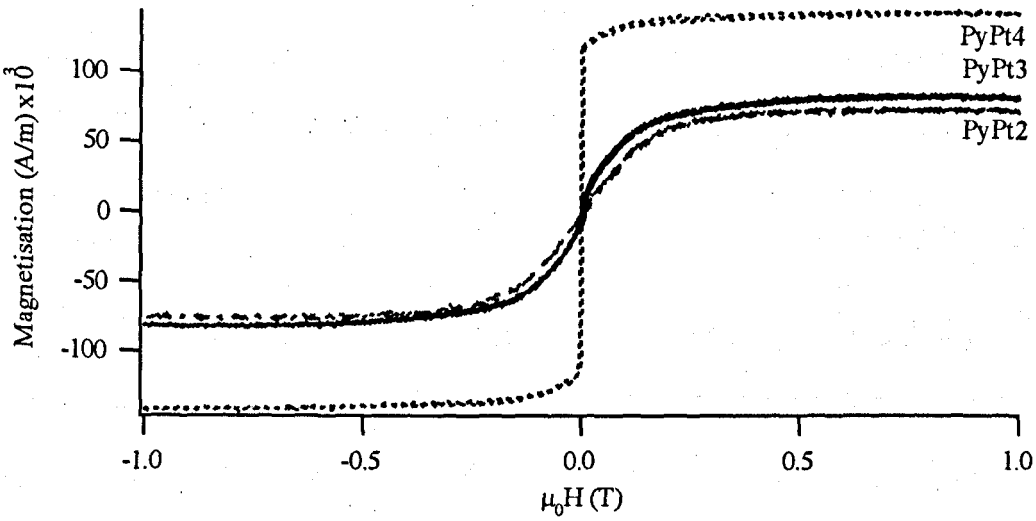

Figure 6.21 Magnetisation curves for samples PyPt2, PyPt3 and PyPt4.

	PyPt2	PyPt3	PyPt4	Reported Value (Crangle and Hallam, 1963)
Saturation Magnetisation (A/m)$\times 10^3$	74	82	144	903

Table 6.3 Shows the saturation magnetisation values for PyPt2, PyPt3 and PyPt4 determined from figure 6.21 and the value determined from the moment/atom of $Ni_{0.8}Fe_{0.2}$ given by Crangle and Hallam (1963).

There are two points to notice regarding the saturation magnetisation values. Firstly the values for PyPt2, PyPt3 and PyPt4 should all be the same. Secondly the value for the saturation magnetisation determined from Crangle and Hallam (1963) is an order of magnitude greater than the measured saturation magnetisations. Both of these points suggest that the determination of the magnetisation values from the measured moments is subject to large errors. The error arises in determining the amount of Py deposited on each multilayer sample. The volume of material was taken as the surface area of the sample multiplied by the intended thickness of the Py layers, i.e. 21×3nm. The error associated with measuring the surface area of the samples is up to 10% and does not account for the factor of 10 difference in the magnetisation values from figure 6.21 with the reported value. Thus the other source of the error must be the thickness of the Py layers in the samples.

We have already seen from the x-ray reflectivity data, section 6.3.1, and from TEM, section 6.3.2, that the actual thicknesses of layers deposited in the samples does not correspond with the intended thicknesses given in Table 6.2. Thus the reported saturation magnetisation values were used to work backwards to determine the amount of Py required to give the measured moment. This gave individual Py thicknesses of 0.25±0.2nm in samples PyPt2 and PyPt3 and 0.50±0.05nm in sample PyPt4. These values are very much smaller than the intended thicknesses for Py of 3nm. For sample PyPt2 an estimate for the bilayer thickness from the TEM

micrograph in figure 6.9(a) was 3.9nm. The expected bilayer thickness from the growth conditions was 4.5nm. This would imply that the thickness of the Py layer was less than 3nm but not as thin as suggested from the magnetisation calculation. Similarly for sample PyPt4, the estimated bilayer thickness was 2.7nm compared to the intended bilayer thickness of 3.5nm. Again this implies that the bilayer thickness is thinner than anticipated but not as thin as determined from the magnetisation calculation. The results of the x-ray reflectivity and TEM suggest that the deposition of material via the Warwick PLAD system is not well controlled. The results of the magnetisation data also suggest that the deposition of the layers is less than intended. However the difference observed in the magnetisation data is significantly less than seen from the TEM and x-ray reflectivity data.. In order to evaluate these differences further magnetisation curves of Py layers of different thicknesses would be required.

Despite some of the discrepancies arising from the magnetisation data it does show that samples PyPt2, PyPt3 and PyPt4 are ferromagnetic. The estimation of the amount of Py present in these samples from the reported saturation magnetisation is small. This suggests that the amount of Py present in the samples may not be enough to show the AMR effect in figure 6.18 and consequently the OMR effect may be significant as the amount of platinum increases from sample PyPt4 through to PyPt2. This could account for the changes in the MR results from sample PyPt4 to PyPt2.

6.6 An Evaluation of the Different Deposition Techniques

The data in this chapter suggest that the smoothest multilayers are deposited using RF sputtering. This is supported by the x-ray reflectivity data which shows interference fringes and n=1 Bragg peak suggesting smooth well defined layers. An increased amount of roughness in seen for the $PLAD_{mos}$ samples, and the most roughness is seen in the $PLAD_{war}$ samples. Thus the conclusions of this work are that there is less control for depositing thin metallic layers for multilayer systems using PLAD techniques. This conclusion is supported by the characterisation of the multilayers investigated in this chapter. For example the AMR features are most pronounced in sample nm25 which is deposited by sputtering followed by sample m6.

The structure of these samples from x-ray reflectivity suggest that they have relatively large bilayer thickness. For nm25 it appears from TEM that there is a significant amount of Py in the sample, which is estimated at 2.3nm. In the case of m6 we expect that the thickness of the Py layer is 1.5nm per layer and accounts for 50% of the layer structure. Samples PyPt2, PyPt3 and PyPt4 show very little evidence of AMR. The sharp features associated with AMR near zero field were not pronounced despite the fact that all the samples were intended to have ~3nm Py per bilayer which is more than for both m6 and nm25. Thus we might have expected a more pronounced AMR effect in all the $PLAD_{war}$ multilayers. Magnetisation curves for samples PyPt2, PyPt3 and PyPt4 suggest that the amount of Py present in the samples is significantly less than expected. This might account for the differences in the magnetoresistance results of these samples compared to the others. The magnetisation results again suggest that there is a lack of control in the deposition by PLAD which is apparent because the actual thicknesses of the multilayer samples do not correspond with the intended thicknesses. However we do see that samples PyPt2, PyPt3 and PyPt4 are ferromagnetic.

The reflectivity data further confirms the lack of control over deposition. The interference fringes arising from the total thickness of the samples are not as clearly defined as for the sputtered samples. In addition the anticipated Bragg peak for sample PyPt4 is obscured by the lack of uniformity in the sample. This illustrates that non-uniformity is a problem in the multilayers deposited by $PLAD_{war}$.

The range of interlayer thicknesses is 0.5-1.5nm for the samples discussed here. Parkin and Rabedeau (1995) show that the oscillatory nature of the GMR effect is of the order of 1nm. In which case it might be expected that GMR would be seen in these samples. Thus the lack of GMR can be mostly attributed to the difficulty in depositing the layers. We see instead a range of AMR and OMR characteristics. In the case of sputtering we see that the layer thickness and quality can be controlled more precisely. For the $PLAD_{mos}$ system there is still a fair amount of control for layer thickness, although an increased amount of roughness is present. The presence

of droplets provides one source of this roughness. Finally films deposited by $PLAD_{war}$ show a high degree of non-uniformity and roughness. The presence of droplets again contributes to the roughness. Some difficulty in maintaining deposition rates is also experienced. This shows insufficient control of metal deposition for multilayer purposes.

Chapter 7

7 Conclusions and Further Work

The literature review shows that there is still a shortage of published work quantifying the effect of PLAD parameters on droplet numbers. This is particularly true in the case of metal deposition. The literature also reveals that the inherent droplet problem prevents the widespread use of PLAD for the production of metallic multilayer samples. Thus this thesis addresses the droplet problem and assesses the suitability of using PLAD for the deposition of novel Py/Pt multilayer structures by comparing samples prepared by two different PLAD techniques and RF sputtering.

7.1 Conclusions to Chapter 5

Chapter 5 investigated the effects of laser wavelength and the temporal profile of the laser pulse on the deposition rates of nickel and silver and the production of droplets during the deposition of films. In addition the effects of a uniform beam profile and a continuously spooled tape target on droplet numbers were also reported.

Firstly the deposition rates of nickel and silver were investigated. The results showed that the deposition rates of silver tended to saturate at wavelengths of 193, 248 and 351nm. Sputtering of the depositing films by incoming energetic species in the plasma was proposed as the origin of the saturation phenomenon. In addition to this it appeared that the deposition rate also depended on the film that had previously been deposited onto the quartz crystal monitor. By looking in detail at the deposition measurements performed it was concluded that self sputtering was the likely cause of the deposition rate characteristics observed with silver. The sputtering yield also accounted for the deposition rate showing a dependence on the thickness of material previously deposited onto the crystal quartz monitor, as shown by figure 5.5.

In contrast to silver the deposition rates of nickel did not show the saturation phenomenon so convincingly. In figure 2.2 we saw that the sputtering yield for nickel was less than that of silver and thus we might have expected this to be the case. In

order to investigate the effects of sputtering on nickel deposition, fluences above the maximum fluence available of $20J/cm^2$ would be required.

The threshold fluences measured for nickel and silver decreased with decreasing laser wavelength, in accordance with equation 2.6, which shows wavelength dependence. However the values calculated using this equation were high in comparison to the measured values. Other models which take into account absorption of the laser pulse, are able to predict threshold fluences closer to those measured in this thesis and elsewhere, see for example Lunney and Jordan (1998). This shows that only a simple ablation model was presented here.

The saturation of the deposition rates of silver occurred at lower fluences for shorter wavelengths. In addition the deposition rates at shorter wavelengths were initially higher. We saw, from figure 5.8, that the average energy of the ions in the plasma was less at shorter wavelengths. Lower energy ions result in less sputtering and therefore deposition rates were initially higher at shorter wavelengths. As the fluence was increased we expected that the average ion energy increased, thus leading to the saturation of the deposition rates.

The results of this work suggest that the phenomenon of self sputtering was a viable explanation for the deposition rate characteristics observed. Deposition rate measurements showed some dependence upon the thickness and type of material previously deposited and upon the energy of incoming ions. Further work could be performed to substantiate the sputtering theory more fully. For example, the deposition rate curves for both nickel and silver could be repeated to provide more data points. In both cases deposition rate measurements should be made onto the same thickness of material each time. For example, 100nm of silver should be present initially on the quartz crystal monitor to minimise the effect that previously deposited material could have upon the deposition rates measured. In addition higher fluences are required to investigate the deposition characteristics of nickel. Another set of deposition rates on to a range of films of different thicknesses, for example 25nm, 50nm, 75nm and 100nm of silver and of nickel, would also add data to figures 5.5 and

5.6. Further measurements might include measuring ion energies in the plasma and correlating these energies with deposition rates to obtain a quantitative evaluation of sputtering at the substrate.

Ablation rates for nickel and silver were compared with values calculated using equation 2.12. The values measured from the targets were higher than determined from equation 2.12. From this it was concluded that the model does not extend well to higher temperatures and pressures. The values from the model were calculated using boiling point temperatures and 1 atmosphere of pressure. These values are lower than the actual surface temperatures and pressures that occur during ablation and thus we expect the calculated values to be lower than the measured values. An attempt was made to use higher temperatures and pressures in the model however the values obtained for the ablation rates were not sensible. Other models such as Phipps *et al.* (1988) and Boardman *et al.* (1996) are found to give ablation rates closer to measured values. These models take into account processes for material removal other than just evaporation.

The effect of laser wavelength on the number of droplets produced during the deposition of nickel and silver was also investigated. The results showed that there might be some dependence of droplet number on laser wavelength although any dependence was nowhere near as marked as seen in oxides. This was because for metals the thermal diffusion length, defined in equation 2.1, is larger than the optical absorption, defined in equation 2.2. In addition to the effect of wavelength on droplet numbers the effect of the number of pulses was also investigated. The results did not give a convincing correlation between the number of pulses used to deposit a film and the number of droplets seen on that film. Thus further work would be required to ascertain whether pulse number has any effect on droplet numbers and also to decide whether this effect is stronger than that of laser wavelength. In order to do this some additional aspects of droplet production need to be clarified first. For example, the effect that polished targets and damaged targets have on the production of droplets needs to be investigated. It has been shown (van de Riet *et al.*, 1993b) that damaged

targets tend to produce more droplets. If this were the case then we would expect the average number of droplets to increase for longer depositions. To ascertain whether or not this occurs, films deposited using the same number of pulses from polished and damaged targets need to be compared. One would hope to show that the use of the lens wobbler would minimise damage to the target and thus there would be no significant change in the number of droplets per pulse at high pulse numbers. In addition the effect that increasing laser fluence has on droplet numbers needs to be established. Some authors have found that droplet numbers increase with laser fluence (Weaver, 1998; Blank *et al.*, 1992) and others have found that they decrease with increasing laser fluence (van de Riet *et al.*, 1993b; Guilfoyle *et al.*, 1997). In general the latter appears to be true for the films deposited in this thesis. Once these trends have been established films deposited with different pulse numbers can be investigated along with more films deposited using different laser wavelengths. To improve upon the results presented in this thesis it would be desirable to increase the counting statistics by depositing more films for comparison. Also, in order to make comparisons more valid similar spot sizes should be used on the targets to avoid differences in the plasma expansion and where possible films of similar thickness should be compared.

When looking at the features on the nickel and silver targets there appeared to be more melting on the silver target than on the nickel target. The melt depths of the nickel and silver targets subject to 200 pulses were estimated using equation 5.3. The calculated values were 5μm and 19μm respectively. This confirmed that for the same fluence more melting occurred on the silver target which corresponded with more droplets being present on silver films than on nickel films. We also saw that droplet sizes given in Table 2.2 corresponded well with both the droplet sizes seen on the deposited films and the size of the asperities formed on the silver target.

Difficulties with achieving isolated picosecond pulses were experienced in the section relating to the effects of the laser pulse profile on deposition rates and droplet production. The calculation in section 5.7.1 showed that the energy associated with

the picosecond part of the pulse profiles was less than 0.1% of the nanosecond background of the pulse profile. Thus the results did not truly investigate the effects of isolated picosecond pulses as intended. This point was borne in mind when interpreting the corresponding data.

For the deposition rates measured using the single ps pulse profile we saw that the ns background appeared to have most effect on the values obtained. For example, the magnitude of the deposition rates was of the same order as observed for the ns pulses in the previous sections. A wide spread in the silver deposition rates was also observed and it was likely that this was due to sputtering at the substrate, although further measurements of silver deposition rates would be required to confirm this. We also saw that for the nanosecond fluence of $10J/cm^2$ the silver deposition rate started to saturate. This compared with the nanosecond data and was also attributed to sputtering. For the nickel deposition rates, again the presence of saturation was not conclusive.

For the ps pulse train profile we saw that the deposition rates were again dominated by the ns background. However, the deposition rate data did not show any sign of saturation.

The deposition rates for both the single ps pulse profile and the ps pulse train profile illustrated the difficulties experienced in deconvolving the ps and ns parts of the profiles to assess the results properly. The evidence suggested that the ns background was dominant in the ablation process. However all of the deposition rate data would benefit from further experimentation to identify conclusively the deposition rate characteristics of both nickel and silver using these two pulse profiles. In order to investigate individual ps pulses a laser system that does not have a ns background associated with the pulse profile would be required. Again particular care concerning the amount of material previously deposited onto the quartz crystal monitor would also be required.

The dominance of the ns background was also apparent for the threshold fluences measured for nickel and silver. The values of threshold fluence were similar

to those observed for the ns pulse profiles. This again confirmed that the fluences associated with the ps pulses were less than the values associated with the ns background. It was shown in table 5.7 that the heating of the target by the ps part of the pulse profile was negligible compared to the ns background. Thus one would expect that the ablation characteristics would be similar to that of the ns ablation characteristics. As for the ns ablation the values for threshold fluence predicted by equation 2.12 were higher than the measured values.

Ablation rates using the ps pulse train profile were determined from the target and were found to be higher than the calculated values. Again the model predicting ablation rates was limited to temperatures and pressures much lower than those actually experienced by the target during ablation. We also saw that the ablation rate calculated for an isolated ps pulse was negligible compared to that of the ns pulse. This was due to the fact that at shorter pulse lengths the assumption that heat transfer to the target occurs instantaneously is no longer valid.

A comparison of films deposited using either the single ps pulse profile or the ps pulse train profile with films deposited using ns pulses revealed that more droplets were present on films deposited using the former profiles. This suggested that melting still occurred when using the ps pulse profiles. This was confirmed by equation 5.3, which showed that the melting was due to the ns background. It was then proposed that an increase in pressure was exerted on the molten surface by the superimposed ps pulses. This increase in pressure exerted by the ps pulses was supported by the Phipps *et al.* (1988) model which showed that the ablation pressure for ps pulses was greater than for ns pulses. Although the conditions pushed the model to the limit, this did give a qualitative explanation for the origin of the increase in droplet numbers using the ps pulse profiles.

The models used to predict the droplet sizes were unsuccessful at shorter pulse lengths, since the ps pulses did not contribute significantly to the heating of the target. For example, the lack of heating due to the ps pulses meant that the thermal expansion of asperities in the Kelly and Rothenberg model (1985a) was also

insignificant. In addition the time scale for thermal expansion is far greater than the 5ps pulse length. Similarly the contribution of the ps pulses to the acceleration of the melt as used by the Bennett *et al.* (1985) model, was also insignificant. Thus the extension of these models to shorter pulse lengths was unsuccessful. Difficulties also arose in deconvoluting the ns and ps contributions of the pulse, which further complicated the calculation of the droplet sizes. The Brailovsky *et al.* (1995) model may be more satisfactory since it looks at the effects of the plasma on the molten surface and there is some indication from the Phipps *et al.* (1988) model that the effects of the plasma are important for describing ablation.

The results presented here show that further work is necessary to ascertain the effects of using individual ps pulses on the production of droplets. If ps pulses were used to deposit films, instantaneous heat transfer would no longer be valid and therefore one might expect the mechanism for droplet formation via the hydrodynamic model, discussed in this thesis, to change. Thus an investigation into the characteristics of particulates and the features on the targets would be required to elucidate some of these changes that might occur in the ablation process at shorter pulse lengths.

Further investigations into the effects of a uniform energy beam profile and the use of a continuously spooled tape target on the production of droplets were performed. For the uniform beam profile droplets were still present on the films deposited. However more films would be required in order to make a statistically valid statement about a correlation of droplet numbers and uniform energy profiles.

In the case of the tape target it was found that many droplets were still present on the deposited films. This implied that the expulsion of material from the tape occurred before a hole was punched through it and that melting still occurred at the target. It was shown by Bostanjoglo *et al.* (1994) that the ejection of molten material occurs within 5ns which is fast when compared with the 25ns pulse envelope. Thus the presence of droplets was not surprising. Further work photographing material removed from the tape target at different times could confirm this process.

In conclusion we saw that sputtering of the depositing film was a problem for PLAD. We also saw that the elimination of droplets was not simple. The kinetic model, which described the removal of material from the target, covered temperatures and pressures well below values that occur during ablation. Other models that take into account absorption of the laser beam by the plasma and the effect of the developing plasma on the target surface give a more successful description of ablation.

Improvements to the results presented here could be made. Firstly for the deposition rate data, more data points are required to confirm the reproducibility of the results already obtained. Secondly for the counting of droplet numbers more films are required to improve the counting statistics and to provide more films for comparison.

7.2 Conclusions to Chapter 6

In chapter 6 the comparison of Py/Pt multilayers deposited using three different deposition systems were described. These were two PLAD systems and RF sputtering. The suitability of these techniques for depositing multilayers was assessed in terms of the uniformity achieved in the samples and the magnetoresistance results.

The uniformity of the layers was assessed using x-ray reflectivity and cross sectional TEM. Starting with the sputtered samples nm23 and nm25, the x-ray reflectivity suggested well-defined samples. The interference fringes related to the thickness of the sample were clearly visible and the intensity did not fall off compared to the other samples, thus indicating smooth layers. The n=1 Bragg peak was present in the data for both of the samples and was used to determine the bilayer thickness. The TEM image of sample nm25 confirmed the uniformity suggested by the x-ray reflectivity data.

Sample m6 was deposited using the Moscow PLAD system. The x-ray reflectivity showed the interference fringes clearly and the n=1 Bragg peak was also present. However the interference fringes were not as well defined as for the sputtered samples and the Bragg peak was slightly broader. In addition a 'hump' was

observed in the data which was not attributed as a Bragg peak. All of these variations in the features indicated that there was a slight decrease is uniformity present in this sample. From the TEM micrographs the layers appeared uniform in thickness thus the non-uniformity in the samples could have been due to roughness between the layers and the presence of droplets. The resolution of the TEM prevented the roughness between layers from being investigated more fully.

Samples PyPt2, PyPt3 and PyPt4 were deposited using the Warwick PLAD system. Samples PyPt2 and PyPt4 were investigated by x-ray reflectivity and TEM. The x-ray reflectivity data for PyPt4 did show some interference fringes although the intensity of these fringes was reduced significantly at higher angles. This suggested that the roughness of this sample was more than for the other samples already discussed. Furthermore the uniformity of the layers was not sufficient to give a Bragg peak. This was confirmed by the TEM micrographs of sample PyPt4 which showed that the layering was not uniform. In sample PyPt2 the x-ray reflectivity curves did not even show interference fringes, thus making any determination of the sample dimensions impossible. Again the TEM micrographs confirmed that the layers were not uniform.

SEM micrographs of the surfaces of the samples revealed that droplets were present on the samples deposited using both the Moscow and Warwick PLAD systems, whilst the RF sputtered samples were relatively smooth. The presence of droplets was a likely contribution to the decrease in uniformity observed in sample m6 deposited using the Moscow PLAD system compared to the sputtered samples nm23 and nm25.

From the structural analysis of these multilayer samples it was shown that the samples produced using RF sputtering had the most uniform layers. We saw that for the Warwick PLAD system problems occurred in successfully depositing uniform multilayers. Even samples deposited at lower fluences using the Moscow PLAD system did not match the uniformity of the samples deposited by RF sputtering.

The work of Parkin (1991) suggested that Pt would give weaker coupling between magnetic layers resulting in a more sensitive giant magnetoresistance effect of multilayer samples at low magnetic fields. However this was not established. Only the anisotropic magnetoresistance effect was measured in the samples, no giant magnetoresistance was observed.

The magnetoresistance data of the sputtered films showed the characteristic features of AMR as seen in figure 3.1. The largest change in resistance occurred near zero field and was dependent upon the orientation of the field and the current. The largest change of 0.5% in the perpendicular geometry and –0.5% in the parallel geometry was seen in sample nm25. For the data presented, however, the true characteristics around zero field were not shown. The results showed that the AMR behaviour could have been precisely determined if a higher density of data points were taken around zero field. This problem of the density of data points might also have obscured hysteresis of the sample that might be expected but not observed. In contrast to sample nm25, sample nm23 showed no characteristic AMR behaviour. From the x-ray reflectivity measurements it was suggested that the thickness of Py in sample nm23 was less than 0.3nm. This might have been insufficient to give a larger effect than the ordinary magnetoresistance due to the Pt present in the sample.

The magnetoresistance data for sample m6 were much the same as for sample nm25. Again the true values of the MR percentage close to zero field were obscured by the insufficient number of data points.

Samples PyPt2, PyPt3 and PyPt4 showed a range of behaviour. Samples PyPt3 and PyPt4 showed a decrease in resistance with increasing field however they did not show the characteristic AMR behaviour as observed in samples m6 and nm25. Sample PyPt2 showed MR data characteristic of the ordinary magnetoresistance effect. Sample PyPt2 was intended to have the highest amount of Pt compared to Py in it and thus it might be expected that the OMR effect from the Pt was larger than the AMR effect from the Py. However further measurements of multilayers with different thicknesses of Pt and Py would be required to confirm this.

The MR results for a Py film deposited using the Warwick PLAD system confirmed the AMR characteristics observed in samples nm25 and m6. Once again the magnitude of the MR% was obscured by the lack of data points around zero field.

Magnetisation loops were measured for samples PyPt2, PyPt3 and PyPt4 to establish whether they were ferromagnetic or not. The results showed that the films were ferromagnetic and further calculations showed that the amount of Py present in the samples was much less than anticipated. This could account for the lack of AMR behaviour in these samples. The magnetisation data provided useful information regarding the thickness of Py in samples PyPt2, PyPt3 and PyPt4. Further measurements of this sort could be used to establish whether a relationship exists between the magnetoresistance characteristics and the thickness of Py and Pt present in the multilayer samples.

The results showed only AMR and OMR behaviour in the Py/Pt multilayer samples. This highlighted the difficulties involved in achieving the correct structure and deposition conditions necessary to make multilayers that show the GMR effect. However the suggestion by Parkin (1991) that this system might give sensitive GMR characteristics make it worthwhile pursuing this multilayer structure.

The differences in uniformity between the samples deposited using sputtering and PLAD might be due to the energy of the species in the deposition plasma. As discussed in chapter 4, self sputtering is a problem for PLAD where the average kinetic energy of the depositing species is higher than for sputtering. This may also have implications for the definition of boundaries between layers in the multilayer samples. The results of chapter 6 suggest that least uniformity was achieved using the Warwick PLAD system. This system was likely to produce higher average kinetic energy deposition species than the Moscow PLAD system because higher fluences were used during deposition. In order to test this out, the energy of the species for each of the systems used would need to be measured and this could be correlated with sample uniformity measured using x-ray reflectivity. This might then provide evidence for the suggested difference between the multilayer samples.

7.3 Final Comments

From the work presented in this thesis it is concluded that if PLAD is to become a competitive alternative to deposition by sputtering further work would be required to increase the control and reproducibility of metal deposition. As highlighted in this thesis the reduction in droplet numbers and increase in the uniformity of the deposition process are two aspects that need to be improved upon. In my opinion the best way to do this would be to improve the beam delivery system so that the laser spot is reproducible on the target. In addition fluctuations in the laser pulse energy should be minimised. This would involve using an excimer laser capable of delivering a pulse energy of at least 500mJ/pulse. With a higher pulse energy the beam could be imaged onto the target, rather than focused, and still maintain a high enough fluence for ablation. The laser would be operated at it's maximum energy and the fluence would be adjusted by attenuating the laser beam. By operating the laser in it's optimum conditions this would ensure that the fluctuations between pulses were minimised. Attenuating the laser beam would enable the spot to be kept the same at all times, thus reducing the effects that changing spot dimensions might have upon the plasma expansion and thus the film deposition. This would minimise the variables in film deposition and increase the chances of producing films that could be sensibly compared.

The laser parameters must be chosen to optimise the deposition of films. The fluence at the target must be chosen to avoid the problem of sputtering at the substrate by energetic species in the plume. This might then minimise roughness developing in multilayer samples and thus improve the uniformity of layered samples. A compromise between high fluences, which give higher deposition rates and possibly more droplet, and lower fluences, which give lower deposition rates and possibly fewer droplets, needs to be established. The use of a higher power laser would enable larger spot dimensions to be used to counteract the problem of lower deposition rates at lower fluences. A system to filter droplets might also be used without compromising deposition rates. Contamination problems must also be addressed. To

prevent contamination of metallic layers deposited by PLAD vacuum conditions must at least match those of sputtering, i.e., 1×10^{-7}mbar. A vacuum loading system should also be considered to prevent contamination.

Although some of the issues raised in this section were not addressed directly in this thesis they have come about as a result of the experience and problems encountered in using a PLAD system and provide useful comments for future systems being set up. From the problems that have been highlighted in this thesis it is clear that further work is required if PLAD is to compete successfully with sputtering for the deposition of metallic films.

Appendix A

Order	Fluence (J/cm^2)	Deposition rates ($nm/pulse/cm^2$)	Thickness Deposited (nm)	Accumulated Thickness On Quartz Monitor (nm)
Series 193nm				New Crystal
1	5.5	0.11	5.8	5.8 (Ni)
2	18	0.16	9.0	9.0 (Ag)
3	18	0.39	22	22 (Ni)
4	12	0.20	11	33 (Ni)
5	12	0.13	7.3	7.3 (Ag)
6	3.6	0.085	4.5	11.7 (Ag)
7	3.6	0.032	1.8	1.8 (Ni)
8	1.3	0.021	5.6	5.6 (Ag)
9	1.3	0.021	5.4	11.0 (Ag)
10	1.3	0.021	5.2	16.2 (Ag)
11	3.8	0.11	4.7	20.9 (Ag)
12	8.1	0.11	12	32.9 (Ag)
13	3.8	0.11	12	44.9 (Ag)

Table A.1 The nickel and silver deposition measurements at λ=193nm shown in figures 5.1 and 5.4.

Order	Fluence (J/cm^2)	Deposition rates ($nm/pulse/cm^2$)	Thickness Deposited (nm)	Accumulated Thickness On Quartz Monitor (nm)
Series Ni 248				New Crystal
1	2.1	0.0002	0.1	0.1 (Ni)
2	3.3	0.0083	1.9	2.0 (Ni)
3	2.4	0.0016	0.6	2.6 (Ni)
4	9.2	0.56	125	127.6 (Ni)
5	8.6	0.47	105	232.6 (Ni)
6	8.4	0.11	24	256.6 (Ni)
7	11	0.22	50	306.6 (Ni)

Table A.2 The nickel deposition measurements at λ=248nm shown in figure 5.4.

Order	Fluence (J/cm^2)	Deposition rates ($nm/pulse/cm^2$)	Thickness Deposited (nm)	Accumulated Thickness On Quartz Monitor (nm)
Series 351nm				New Crystal
1	16	0.46	42	42 (Ni)
2	3.3	0.02	2.0	2.0 (Ag)
3	3.5	0.01	1.8	1.8 (Ni)
4	18	0.33	30	30 (Ag)
5	16	0.30	27	57 (Ag)
6	16	0.27	24	24 (Ni)
7	9.7	0.04	3.6	27.6 (Ni)
8	9.7	0.15	13	13 (Ag)

Table A.3 The nickel and silver deposition measurements at λ=351nm shown in figure 5.1 and 5.4.

Order	Fluence (J/cm^2)	Deposition rates ($nm/pulse/cm^2$)	Thickness Deposited (nm)	Accumulated Thickness On Quartz Monitor (nm)
Series 1				New crystal
1	2.0	0.093	4.9	4.9 (Ni)
2	2.0	0.093	9.2	14.1 (Ni)
3	6.2	0.36	36	50.1 (Ni)
4	3.1	0.17	17	67.1 (Ni)
5	4.7	0.26	26	93.1 (Ni)
6	11	0.47	47	140.1 (Ni)
7	5.3	0.28	28	167.7 (Ni)
Series 2				168.1 (Ni)
1	12	0.47	47	215.1 (Ni)
2	14	0.47	47	262.1 (Ni)
3	14	0.47	47	309.1 (Ni)
4	5.0	0.13	12	321.1 (Ni)
5	7.8	0.28	28	349.1 (Ni)
6	11	0.36	36	385.1 (Ni)
7	16	0.40	40	425.1 (Ni)
8	2.7	0.029	2.9	428 (Ni)

Continued...

Series 3				103 (Ag)
1	15	0.31	31	31 (Ni)
2	15	0.32	32	63 (Ni)
3	9.7	0.26	26	89 (Ni)
4	4.9	0.17	16	105(Ni)
5	6.8	0.20	17	122(Ni)
6	1.5	0.005	0.5	122.5 (Ni)
7	2.3	0.041	4.3	126.8 (Ni)
8	15	0.31	31	157.8 (Ni)

Table A.4 The nickel deposition measurements of *series 1, 2, and 3* shown in figure 5.3. λ=248nm.

Order	Fluence (ps/ns pulses) (J/cm^2)		Deposition rates ($nm/pulse/cm^2$)	Thickness Deposited (nm)	Accumulated Thickness On Quartz Monitor (nm)
Nickel ps train	ps	ns			New Crystal
1	0.006	6.0	0.045	56	56 (Ni)
2	0.004	3.7	0.023	28	84 (Ni)
3	0.002	2.1	0.015	19	103 (Ni)
4	0.004	3.7	0.030	37	140 (Ni)
5	0.001	1.1	0.003	4.4	144.4 (Ni)
Silver ps train					144.4 (Ni)
1	0.003	2.7	0.044	54	54 (Ag)
2	0.002	1.6	0.032	40	94 (Ag)
3	0.001	1.1	0.015	19	113 (Ag)
4	5e-4	0.53	0.001	1.8	114.8 (Ag)

Table A.5 The nickel and silver deposition measurements shown in figure 5.18. λ=248nm.

Bibliography

Akhsakhalyan, A.D., S.V Gaponov, S.A Gusev, V.I. Luchin, Yu. Ya. Platonov and N.N. Salashchenko (1984), *Sov. Phys. Tech. Phys.* **29**, 446.

Antoni, F., E. Fogarassy, C. Fuchs, B. Prevot and J.P. Stoquert (1995), *Appl. Surf. Sci.* **86**, 175.

Askar'yan, G.A., A.M. Pokhorov, G.F. Chantutiya,and G.P. Shipulo (1963), *Sov. Phys. JETP* **17**, 6.

Bainich, M.N., J.M. Broto, A. Fert, F. Nguyen Van Dau, F. Petroff, P. Eitenne, G. Creuzet, A. Friederich and J. Chazelas (1988), *Phys. Rev. Lett.* **61**, 2472.

Bennett, T.D., C.P. Grigoropoulos and D.J. Krajnovich (1995), *J. Appl. Phys.* **77**, 849.

Binasch, G., P. Grunberg, F. Saurenbach and W. Zinn (1989), *Phys. Rev.* **B39**, 4829.

Blank, D.H.A., R.P.J. IJsselsteijn, P.G. Out, H.J.H. Kuiper, J. Flokstra and H. Rogalla (1992), *Materials Science and Engineering* **B13**, 67.

Boardman, A.D., B. Cresswell and J. Anderson (1996), *Appl. Surf. Sci.* **96-98**, 55.

Bostanjoglo, O., R. Niedrig and B. Wedel (1994), *J. Appl. Phys.* **76**, 3045.

Boyakovet, V.M., V.M. Epikhin, B.A. Kalin, M.K. Makhatov, I.N. Nikolaev and G.N. Shishkin (1978), *Sov. J. Quantum Electronics* **8**, 902.

Brailovsky, A.B., S.V. Gaponov and V.I. Luchin (1995), *Appl. Phys.* **A61**, 81.

Callegaro, L., E. Puppin and A. Sattamino (1994), *Meas. Sci. Technol.* **5**, 1013.

Chan, C.L. and J. Mazumder (1987), *J. Appl. Phys.* **62**, 4579.

Chen, L.-C. (1994), in *Pulsed Laser Deposition of Thin Films* (D.B. Chrisey and G.K. Hubler, eds.), Wiley, New York, p.167.

Cherief, N., D. Givord, A. Lienard, K. Mackay, O.F.I.C. McGarth, J.P. Rebouillat, F. Robaut and Y. Souche (1993), *J. Magn. Magn. Mater.* **121**, 94.

Cheung, J.T. (1994), in *Pulsed Laser Deposition of Thin Films* (D.B. Chrisey and G.K. Hubler, eds.), Wiley, New York, p.1.

Cheung, J.T., and H. Sankur (1988), *CRC Crit. Rev. Solid State Mater. Sci.* **15**, 63.

Chichkov, B.N., C. Momma, S. Nolte, F. von Alvensleben and A. Tunnermann (1996) *Appl. Phys.* **A63**, 109.

Chuang, M.-C., and A.C. Tam (1989), *J. Appl. Phys.* **65**, 2591.

Corkum, P., F. Brunel, N. Sherman and T. Srinivasan-Rao (1990), *Phys. Rev. Lett.* **64**, 1847. Also see (1988), *Phys. Rev. Lett.* **61**, 2886.

Crangle, J., and G.C. Hallam (1963), *Proc. R. So. London* **A 272**, 119.

CRC Handbook of Chemistry and Physics 73rd edition (1992), (D.R. Lide, ed.), CRC Press Inc.

Dijkkamp, D., T. Venkatesan, X.D. Wu, S.A. Shaheen, N. Jisrawi, Y.H. Min-Lee, W.L. McLean and M. Croft (1987), *Appl. Phys. Lett.* **51**, 619.

Dreyfus, R.W. (1991), *J. Appl. Phys.* **69**, 3.

Dreyfus, R.W., C. Phipps and A. Vertes (1994), *Laser Ablation: Mechanisms and Applications II, 2nd International Conference,* American Institute of Physics Conf. Proc. **228**, p285.

Du, D., X. Liu, G. Korn, J. Squier and G. Mourou (1994), *Appl. Phys. Lett.* **64**, 3071.

Dupas, C., P. Beauvillain, C. Chappert, J.R. Renard, F. Trigui, P. Velu and D. Renard (1990), *J. Appl. Phys.* **67**, 5680.

Dupendant, H., J.P. Gavigan, D. Givord, A. Lienard, J.P. Rebouillat and Y. Souche (1989), *Appl. Surf. Sci.* **43**, 369.

Dyer, P.E., R.D. Greenough, A. Issa and P.H. Key (1989), *Appl. Surf. Sci.* **43**, 387.

Enrech, M., J.G. Lunney, R. Skomski and J.M. Coey (1994), *Mater. Sci. Eng.* **B23**, 25.

Fabbro, R., E. Fabre, F. Amiranoff, C. Garban-Labaune, J. Virmont, M. Weinfeld and C.E. Max (1982), *Phys. Rev.* **A26**, 2289.

Fahler, S. and H.-U. Krebs (1996), *Appl. Surf. Sci.* **96-98**, 61.

Gapanov, S.V., B.M. Luskin and N.N. Salashchenko (1979), *Sov. Tech. Phys. Lett.* **5**, 210.

Gaponov, S.V., A.A. Gudkov, A.A. Fraerman (1982), *Sov. Phys. Tech. Phys.* **27**, 1130.

Gaponov, S.V., S.A Gusev, Yu. Ya. Platonov, N.N. Salashchenko and E.S Gluskin. (1983), *Sov. Tech. Phys. Lett.* **9**, 91.

Gavigan, J.P., (1990), *Proceedings of NATO ASI on the Science and Technology of Nanostructured Magnetic Materials,* Aghia Pelaphria, Crete, Greece.

Geilman, T., J. Chevallier, M. Fanciulli, G. Weyer, V. Nevolin and A. Zenkevitch (1997), *Appl. Surf. Sci.* **109/110**, 570.

Gorbunov, A.A., W. Pompe, A. Sewing, S.V. Gapanov, A.D. Akhsakhalyan, I.G. Zabrodin, I.A. Kas'kov, E.B. E.B. Klyenkov, A.P. Morozov, N.N. Salachenko, R. Dietsch, H.Mai and S. Vollmar (1996), *Appl. Surf. Sci.* **96-98**, 649.

Green, S.M., A. Pique, K.S. Harshavardhan and J.S. Berstein (1996), in *Pulsed Laser Deposition of Thin Films* (D.B. Chrisey and G.K. Hubler, eds.), Wiley, New York, p.23.

Grolier, V., D. Renard, B. Bartenlian, P. Beauvillain, C. Chappert, C. Dupas, J. Ferre, M. Galtier, E. Klob, M. Molly, J.P. Renard and P. Veillet (1993), *Phys. Rev. Lett.* **71**, 3023.

Groneveld, R.H.M., R. Sprik and A. Ladendijk (1995), *Phys. Rev.* **B51**, 11433.

Guilfoyle, S.J., M. Perry and D. Bernard (1997), poster presentation at the PLAD Workshop (1997), Department of Physic, Queen's University Belfast.

Hermann, J., C. Boulmer-Leborgne and D. Hong (1998), *J. Appl. Phys.* **83(2)**, 691.

Hill, E.W., *Private communication* The Manchester School of Engineers, The University of Manchester, Oxford, Road M139PL.

Horwitz,, J.S., and J.A. Sprague (1994), in *Pulsed Laser Deposition of Thin Films* (D.B. Chrisey and G.K. Hubler, eds.), Wiley, New York, p.229.

Huai, Y., M. Chaker, H. Pepin, S. Boily, X. Bian and R.W. Cochrane (1994), *J. Magn. Magn. Mater.* **136**, 204.

Hubler, G.K. (1994), in *Pulsed Laser Deposition of Thin Films* (D.B. Chrisey and G.K. Hubler, eds.), Wiley, New York, p.327.

Hylton, T.L., K.R. Coffey, M.A. Parker and J.K. Howard (1993), *Science* **261**, 1021.

Jackson, T.J. and S.B. Palmer (1994), *J. Phys. D: Appl. Phys.* **27**, 1581.

Jackson, T.J., N.J. Appleyard, M.J. Cooper, D.H. Richards and S.B. Palmer (1995), *Meas. Sci. Technol.* **6**, 128.

Jackson, T.J., S.B. Palmer, H.J. Blythe and A.S. Halim (1996) *J. Magn. Magn. Mater.* **159**, 269.

Jandeleit, J., G. Urdasch, H.D. Hoffmann, H.-G. Treusch and E.W. Kreutz (1996), *Appl. Phys.* **A63**, 117.

Jiles, D. (1998) *Introduction to Magnetism and Magnetic Materials 2nd ed.* Chapman and Hall.

Jordan, R., D. Cole, J.G. Lunney, K. Mackay and D. Givord (1995), *Appl. Surf. Sci.* **86**, 24.

Jordan, R., D. Cole and J.G. Lunney (1997), *Appl. Surf. Sci.* **109/110**, 403.

Kautek, W., B. Roas and L. Schultz (1990), *Thin Solid Films* **191**, 317.

Kaye, G.W.C. and T.H. Laby (1986), *Table of Physical and Chemical Constants*, Longman Scientific and Technical.

Kelly, R., and A. Miotello (1994), *Laser Deposition of Thin Films*, (Chrisey, D.B. and G.K. Hubler, eds.), Wiley, New York, p55.

Kelly, R., and J.E. Rothenberg (1985a), *Nucl. Instrum. Meth.* **B7/8**, 755.

Kelly, R., J.J. Cuomo, P.A. Leary, J.E. Rothenberg, B.E. Braren and C.F. Aliotta (1985b), *Nucl. Instrum. Meth.* **B7/8**, 187.

Kim, D.-E., S.-M. Lee, I.-J. Jeon and M. Yanagihara (1998), *Appl. Surf. Sci.* **127-129**, 531.

Kim, D.-E., D.-H. Cha, S.-W. Lee (1997), *J. Vac. Sci. Technol.* **A15**, 2291.

Kononenko, T.V., S.V. Garnov, S.M. Klimentov, V.I. Konov, E.N. Loubruin, F. Dausinger, A. Raiber and C. Taut (1997), *Appl. Surf. Sci.* **109/110**, 48.

Kashchiev, D. (1977), *J. Cryst. Growth* **40**, 29.

Koo, T.Y., S.H. Park, K.-B. Lee and Y.H.Jeong (1997), *Appl. Phys. Lett.* **71**, 977.

Kools, J.C.S. (1992), *J. Vac. Sci. Tech.* **A10**, 1809.

Kools, J.C.S., R. Coehoorn, F.J.G. Hakkens and R.H.J. Fastenau (1993), *J. Magn. Magn. Mater.* **121**, 83.

Kools, J.C.S. (1994), in *Pulsed Laser Deposition of Thin Films* (D.B. Chrisey and G.K. Hubler, eds.), Wiley, New York, p.455.

Koren, A., A. Gupta, R.J. Baseman, M.I. Lutwyche and R.B. Laibowitz (1989), *Appl. Phys. Lett.* **55**, 2450.

Krebs, H.-U., S. Fahler and O. Bremert (1995a), *Appl. Surf. Sci.* **86**, 86.

Krebs, H.-U., O. Bremert, M. Stormer and Y. Luo (1995b), *Appl. Surf. Sci.* **86**, 90.

Krebs, H.-U., M. Stormer, S. Fahler, O. Bremert, M. Hamp, A. Pundt, H Teichler, W. Blum and T.H. Metzger (1997), *Appl. Surf. Sci.* **109/110**, 563.

Landolt-Bornstein (1986), **III/19a** Springer Verlag.

Laser Deposition of Thin Films (1994), (Chrisey, D.B. and G.K. Hubler, eds.), Wiley, New York.

Levoska, J., and S. Leppavuori (1995), *Appl. Surf. Sci.* **86**, 180.

Li, Q. (1994), in *Pulsed Laser Deposition of Thin Films* (D.B. Chrisey and G.K. Hubler, eds.), Wiley, New York, p.535.

Luft, A., U. Franz, A. Emsermann A. and J. Kasper (1996), *Appl. Phys.* **A63**, 93.

Lunney, J.G. (1995), *Appl. Surf. Sci.* **86**, 79.

Lunney, J.G., and R. Jordan (1998), *Appl. Surf. Sci.* **127-129**, 941.

Macquart, P., F. Bridou and B. Pardo (1991), *Thin Solid Films* **203**, 77.

Mai, H., and W. Pompe (1992), *Appl. Surf. Sci.* **54**, 215.

Martin, J.A., L. Vazques, P. Bernard, F. Comin, and S. Ferrer (1990), *Appl. Phys. Lett.* **57**, 1742.

Martynyuk, M.M. (1983), *Russian J. Phys. Chem.* **57**, 494.

Mathon, J., (1991), *Contemp. Phys.* **32,** 143.

Matthias, E., M. Reichling, J. Seigel, O.W. Kading, S. Petzoldt, H. Skurk, P. Bizenberger and E. Neske (1994), *Appl. Phys.* **A58**,129.

McGuire, T.R., and R.I. Potter (1975), *IEEE Trans. Mag.* **MAG-11**, 1081.

Meaden, G.T., (1966), *Electrical Resistance of Metals*, Heywood Books, UK.

Metev, S. (1986), *Laser Processing and Diagnostics (II)*, (D. Bauerle, K.L. Kompa and L. Laude, eds.), Euro. Mat. Res. Soc. Symp. Proc., 143.

Metev, S. (1994), in *Pulsed Laser Deposition of Thin Films* (D.B. Chrisey and G.K. Hubler, eds.), Wiley, New York, p.255.

Metev, S., and K. Meteva (1989), *Appl. Surf. Sci.* **43**, 402.

Misra, D.S., and S.B. Palmer (1991), *Physica C*, **176**, 43.

Momma, C., S. Nolte, B.N. Chichkov, F. von Alvensleben and A Tunnermann (1997), *Appl. Surf. Sci.* **109/110**, 15.

Muenchausen, R.E., and X.D. Wu (1994), in *Pulsed Laser Deposition of Thin Films* (D.B. Chrisey and G.K. Hubler, eds.), Wiley, New York, p.357.

Muller, F., K. Mann, P. Simon, J.S. Bernstein and G.J. Zaal (1993), *SPIE* **1848**, 464.

Ohanian, C.H., (1994), *Principles of Physic*, Norton and Co., 542.

Parkin, S.S.P., N. More and K.P Roche (1990), *Phys. Rev. Lett.* **64**, 2304.

Parkin, S.S.P., (1991), *Phys. Rev. Lett.* **67**, 3598.

Parkin, S.S.P., T.A. Rabedeau, R.F.C. Farrow and R. Marks (1994), *J. Appl. Phys.* **76**, 6617.

Parkin, S.S.P. (1995), *Annu. Rev, Mater. Sci.* **25**, 357.

Parkin, S.S.P., and T.A. Rabedeau (1996), *Appl. Phys. Lett.* **68**, 1162.

Phipps, C.R., and R.W. Dreyfus (1993), in *Laser Ionization Mass Analysis*. Chemical Analysis Series **vol 124** (A. Vertes, R. Gijbels and F. Adams eds.), Wiley and Sons, Inc., 369.

Phipps, Jr., C.R., T.P. Turner, R.F. Harrison, G.W. York, W.Z. Osborne, G.K. Anderson, X.F. Corlis, L.C. Haynes, H.S. Steele, K.C. Spicochi and T.R. King (1988), *J. Appl. Phys.* **64**, 1083.

PLAD Workshop (1997), Department of Physic, Queen's University Belfast.

Preuss, S., E. Matthias and M. Stuke (1994), *Appl. Phys.* **A59**, 79.

Preuss, S., A. Demchuk and M. Stuke (1995), *Appl. Phys.* **A61**, 33.

Ready, J.F. (1963), *Appl., Phys. Lett.* **3**, 11.

Rodmacq, B., B. George, M. Vaezzadeh, M. Gerl and Ph. Mangin (1992), *J. Phys. Condensed Matter* **4**, 4527.

Rodmacq, B., G. Palumbo, P. Gerard (1993), *J. Magn. Magn. Mater.* **118**, L11.

Rosenfeld, A., and E.E.B. Campbell (1996), *Appl. Surf. Sci.* **96-98**, 430.

Rothman, J., D. Givord and C. Meyer (1997), *J. Magn. Magn. Mater.* **165**, 202.

Saenger, K.L. (1993), *Processing Adv. Mater.* **3**, 63.

Sandy Lee, I.-Y., W.A. Tolbert, D.D. Dlott, M.M. Doxtader, D.M. Foley, D.R. Arnold and E.W. Ellis (1992), *J. Imaging Sci. and Technology* **36**, 188.

Sato, T., S. Furuno, S. Iguchi and M. Hanabusa (1987), *Jpn. J. Appl. Phys.* **26(II)**, L1487.

Scheibe, H.-J., A.A. Gorbunov, G.K. Baranova, N.V. Klassen, V.I. Konov, M.P. Kulakov, W. Pompe, A.M. Prokhorov and H.-J. Weiss (1990), *Thin Solid Films* **189**, 283.

Shintaku, K., N. Hosoito and T. Shinjo (1993), *J. Magn. Magn. Mater.*

Singh, S.K., S.B. Palmer, D. McK Paul, M.R. Lees (1996), *J. Phys. D, Appl. Phys.* **26**, 2522.

Smit, J. (1951), *Physica* **XVI (6)**, 612.

Smith., H.M. and A.F, Turner (1965), *Appl. Opt.* **4**, 147.

Stauter, C., J. Fontaine and Th. Engel (1996), *Appl. Surf. Sci.* **96-98**, 522.

Stone, L.A., H.V. Snelling and A.G. Jenner (1997), *Appl. Surf. Sci*, **109/110**, 389.

Stuart, B.C., M.D. Feit, A.M. Rubenchik, B.W. Shore and M.D. Perry (1995), *Phys. Rev. Lett.* **74**, 2248.

Svendsen, W., O. Ellegaard and J. Schou (1996), *Appl. Phys* **A 63,** 247

Tabor, D. (1979), *Gases, Liquids and Solids* 2nd ed., Cambridge University Press.

Thomas, D.W., C. Foulkes-Williams, P.T. Rumsby and M.C. Gower (1992), *Laser Ablation of Electronic Materials. Basic Mechanisms and Applications*, North Holland, p221.

Turcu, I.C.E., M.C. Gower, C.J. Reason, P. Huntington, M. Schulz, A.G. Michette, F. Bijkerk, E. Louis, G.J. Tallents, Y. Al-Hadithi, and D. Batani (1991), *Excimer Lasers and Applications III SPIE* **1503**, 381.

Turcu, I.C.E., I.N. Ross, P. Trenda, C.W. Wharton, R.A. Meldrum, H. Daido, M.S. Schulz, P. Fluck, A.G. Michette, A.P. Juna, J.R. Maldonado, H. Shields, G.J. Tallents, L. Dwived, J. Krishnan, D.L. Stevens, T.J. Jenner, D. Batani and H. Goodson (1994), *Applications in Laser Plasma Radiation* **2015**, 243.

Turcu, I.C.E., *Private communication*, Central Laser Facillity, Rutherford Appleton Laboratory, Chilton, Didcot, Oxon, OX11 0QX.

van de Reit, E., J.C.S. Kools and J. Dieleman (1993a), *J. Appl. Phys.* **73**, 8295.

van de Reit, E., C.J.C.M. Nillesen, J. Dieleman (1993b), *J. Appl. Phys.* **74**, 2008.

von Allmen and Blatter, M., and A. Blatter (1995), *Laser-Beam Interactions with Materials* 2nd ed., Springer-Verlag.

Weaver, I., and C.L.S. Lewis (1996), *Appl. Surf. Sci* **96-98**, 663.

Weaver, I. (1998), PhD Thesis, The Queen's University, Belfast.

White, R.M. (1963), *J. Appl. Phys.* **34**, 3559.

Yang, Q., S.-F. Lee, P. Holody, R. Loloee, P.A. Schroeder, W.P. Pratt Jr. and J. Bass (1994) *Physica B* **194-196**, 327.

Zalm, P.C. (1984), *J. Vac. Sci. Technol.* **B2**, 151.

Zhang, W., I.W. Boyd, N.S. Cohen, Q.T. Bui and Q.A. Pankhaurst (1997), *Appl. Surf. Sci.* **110**, 350.